

2 R&D, Prototypes, Test Results

Introduction

In the late eighties, the interest for solar-blind single-photon detectors was revived by independent works studying the possibility of using CsI-based wire chambers of large area. High quantum efficiency (QE) values were reported in Refs. [1, 2] for CsI- and TMAE-coated films in CH_4 and stable operation of CsI-based gaseous photomultipliers under high gain was achieved. The growing availability of sophisticated integrated electronics opened the possibility of instrumenting wire chambers with large areas of pad-segmented cathodes using sensitive and low-noise front-end amplifiers of convenient volume, and at an affordable cost.

During the same time, the HEP community started to propose new experimental facilities dedicated to the future colliders SLAC, RHIC, and the LHC. The development of CsI RICH detectors designed to achieve particle identification in various momentum ranges was therefore undertaken by many research teams and included a common feature, the possibility to operate in high-density particle environments.

This situation led to the launching in 1992 of a CERN R&D project, RD-26 [3], aimed at studying the ‘Development of a large-area advanced fast RICH detector for particle identification at the Large Hadron Collider operated with Heavy Ions’. Several groups joined RD-26, proposing CsI RICH detectors to be integrated into the following large experiments: HADES at GSI Darmstadt, Babar at SLAC, HERA-B in Hamburg, ALICE at LHC. In addition, basic research work on CsI thin films was undertaken, in the collaboration, by specialized laboratories such as the Weizmann Institute, Ecole Polytechnique Palaiseau and EPF Lausanne [4].

A wide variety of research work has been performed in these laboratories both on matters of common interest such as CsI layer processing, chamber optimization, front-end electronics etc. and on more specific topics such as radiator systems, pattern recognition, etc. A part of the information can be found in the RD-26 Status Reports issued every year [5] as well as in review papers [6] and proceedings of workshops dedicated to RICH detectors and photodetection [7].

After four years of developments in RD-26, three large experiments have adopted the use of CsI RICH detectors as part of their apparatus: HADES [8], ALICE [9] and COMPASS/NA58 [10]. A detector of about half a square metre of CsI photocathode has been built and successfully operated in the NA44 experiment [11]. In the next section, we shall report on the studies related to ALICE detectors. Different options were adopted for other detector systems like HADES [8].

2.1 Basic CsI RICH components

The design of a CsI-RICH detector is based on the following requirements:

- i) produce a CsI thin film of large area deposited on the cathode of a MWPC providing a high QE in the wavelength range below 210 nm (photoelectric threshold);
- ii) ensure that an efficient detection of single electrons is obtained under stable operation of the MWPC having CsI-covered cathode and open geometry;
- iii) make a detector system, with radiator and gaseous media highly transparent to UV light, allowing the generation and propagation of Cherenkov photons with wavelength below the 210 nm threshold.

We shall first discuss these basic features in general terms of their physical properties as well as their implications on the design of a RICH detector.

2.1.1 The CsI thin film

Combined with vacuum or gaseous electron multipliers, CsI photocathodes provide an efficient mean for UV photon imaging over a considerable spectral range [12]. It is limited in the short wavelengths by optical window or gas absorption and reaches a cut-off at a wavelength around 210 nm ($E_g \sim 6$ eV). Of all alkali halides, CsI has the largest quantum efficiency. This is due to its low electron affinity ($E_a = 0.1 \div 0.2$ eV) and to its exceptionally large electron escape length, which is 16 nm for 1 eV electrons [13]. Indeed, the QE of CsI surpasses that of all known solid UV photocathodes. It is comparable to that of TMAE (tetrakis (dimethylamine) ethylene) vapours in the short wavelengths but is smaller by about a factor of two above 190 nm. Compared to gas photoconversion, affecting the time response, occupancy and localization properties of the photodetector, CsI-based devices have the advantage of surface conversion and emission. The latter is of prime importance for operation at very high photon flux and for the ultimate localization and timing under oblique photon incidence.

CsI films are simple to prepare and are rather stable when exposed to ambient air. A low sensitivity to exposure at oxygen is indeed expected for material having $E_g + E_a > 6$ eV [14]. This specific property is the key feature for the processing of large areas of CsI thin films. It will be reported in the next sections that such a processing implies a series of manipulations and transfers from the evaporation station to the photodetector that would be impossible in the high vacuum conditions imperatively needed in the processing of bi-alkali halide photocathodes operating in the visible range.

Finally, the relatively low volume resistivity of CsI thin film (< 500 nm thickness), of the order of $10^{10} - 10^{11} \Omega \text{ cm}$ [15], makes possible their stable operation at high radiation fluxes under high gaseous multiplication conditions.

2.1.1.1 Preparation of the CsI film

The CsI films are usually prepared by resistive vacuum deposition, the substrates being kept either at room temperature or heated, as will be discussed later. In the processing of CsI layers, some physical features of this compound have to be taken into account:

- melting and boiling temperatures at 621 and 1280 °C, respectively;
- insulator compound with poor thermal conductance;
- high vapour pressure at melting point (0.1 mbar at 621 °C).

According to Maier-Komor [16], these features favour a dissociation of the CsI molecules during thermal evaporation when too high a temperature is reached at local points as supported by the observation of a non-stoichiometric composition of CsI thin films [17]. This suggests to use the electron gun evaporation with a cooled crucible and well-controlled surface evaporation. However, a large proportion of the users adopted the easier thermal evaporation. To palliate the above effects, the evaporation boat is prepared by pre-melting the CsI powder or small crystal pieces under vacuum, ensuring a good thermal contact between the boat and the load for future use. To eliminate the presumably contaminated superficial layer of the pre-molten CsI load, the deposition under vacuum is started by a short release on a rotatable shutter and only then pursued on to the substrate.

It was found that the physical form and purity of the raw CsI material might play some role in the photoemission properties of the photocathode, probably due to the concentration of impurities. Anderson et al. [18] reported on significantly superior QE values, starting from large CsI crystals. We have not observed such an enhancement and have subsequently employed, as most of the users, CsI powder of different purities.

CsI is also known as a hygroscopic compound: exposed to moist air, its surface becomes whitish. Many compounds are formed from chemical and photo-reaction of water vapour with the CsI surface, such as cesium hydroxide (CsOH), oxide (Cs₂O), iodate (CsIO₃) and hydrogen iodide multihydrate (HI · (nH₂)). All of them will degrade the CsI QE by poisoning the surface and the CsI bulk after diffusion. In the case of free cesium, fast oxidation is observed. Therefore, it is advisable to perform the deposition

of CsI film in the best possible vacuum. In addition, it is essential to get the substrate surface free of moisture, requiring a heavy outgassing, preferably at the highest temperature tolerated by the substrate under vacuum.

In practice, as reported by different groups, the pressure during the evaporation may range between 1.0×10^{-4} and 5.0×10^{-7} Torr without any clear indication of great influence on the photocathode performance. However, since the QE evaluation of a fresh photocathode is usually carried out a short time period after its production, it is likely that all the early contaminations influence the ageing properties of the film, affecting the rate of chemical reactions in the longer term.

No visible influence on the photocathode performance has been seen by varying the evaporation rate between 1 and 50 nm/s in the 1.0×10^{-5} to 5.0×10^{-7} Torr vacuum range.

2.1.1.2 Evaluation of the CsI film

The two major parameters of a CsI film, relevant to its application as RICH photocathode, are the QE as a function of the wavelength of the incident photon and the long-term stability versus external agents (chemical contamination, radiation, etc.). It is expected that the optimization of these two variables will depend on a variety of physical and technical parameters such as evaporation procedures, substrate composition, microstructures, etc.

The QE measurements of CsI films can be carried out in vacuum and in gas media. The studies are usually made in three different modes:

- a) measuring a DC photocurrent in vacuum or gas under relatively low electrical fields;
- b) counting pulses in CsI-based wire chambers, under gas multiplication at moderate-to-high fields;
- c) counting particle-induced photoelectrons in a CsI-based UV detector using Cherenkov emission.

QE measurements under vacuum

The results presented in this section are obtained using method a), studying small-area CsI samples with a monochromatic UV beam in a laboratory vacuum vessel. The QE differential curves will serve as a reference for comparison with results obtained with large photodetectors operated under gas with single Cherenkov photon counting, method c).

Among the numerous studies performed on the subject (see references quoted in Refs. [4, 6, 7]), we shall refer only to the ones performed at the Weizmann Institute by Malamud et al., [19]. A versatile apparatus was built in that institute, schematically shown in Fig. 2.1, where the following operations can be performed in sequence:

- resistive CsI film deposition under high vacuum and controlled by quartz balance;
- in situ exposure to a monochromatic collimated beam using a D₂ Hamamatsu DC-lamp and measurement of the induced photocurrent using a Keithley picoammeter;
- adjustable substrate temperature for film conditioning;
- measurement of the incident photon flux by deviating the UV beam by means of a rotatable mirror on a calibrated photomultiplier (Hamamatsu R1460).

Two reasons made that instrument the most appropriate for our purposes:

- a) the full sequence of operations and measurements is achieved in the same vacuum vessel, the CsI films are studied under optimal condition of cleanliness warranting excellent reproducibility;
- b) the problem of measuring the absolute photon flux in the 150 ÷ 210 nm range was mastered by calibrating commercial phototubes against a NIST reference (see Breskin in Ref. [4]).

All of our optimization studies on substrates and post treatment were done in close collaboration with the Weizmann group.

Figure 2.2 shows the differential CsI QE curve obtained in vacuum by averaging a large number of measurements. The error is evaluated to $\pm 5\%$. The CsI films, 500 nm thick, were deposited on a polished stainless-steel substrate, held at 50°C and submitted to the post treatment described below. That curve will be taken as a reference curve and referred to as ‘QE-RD-26’. On the same figure is shown the best result obtained by Seguinot et al. [2] with a significantly higher QE value. It was not possible to reproduce such a good result in our set-up.

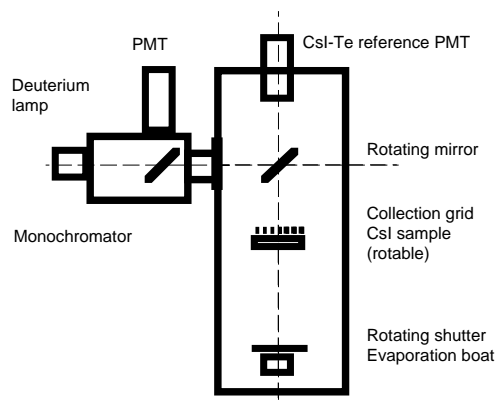


Figure 2.1: Scheme of the set-up used to measure the QE of CsI evaporated on small samples. After coating, the sample is rotated by 180° , under vacuum, to be illuminated from the top by the UV collimated beam.

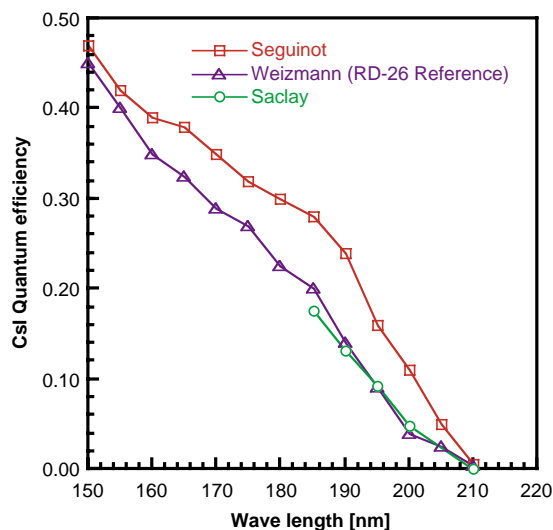


Figure 2.2: Measurements of the CsI QE as a function of wave length: a) Seguinot et al., best result from Ref. [2]; b) Weizmann, average curve [19]; c) Besson et al. [4]. Measurements a) and b) were made under vacuum.

Influence of the polarization and of the angle of incidence

The measurements described were performed using unpolarized UV beams at normal incidence while Cherenkov photons to be counted in a RICH detector are emitted in a p-polarized state and are expected to impinge on the CsI surface at large angle, 60–70 degrees. As shown in Fig. 2.3 the polarization state does not affect the reflection coefficient at normal incidence but does so significantly in the 60–80 degree range according to the polarization state. Hence, the QE measured by both methods — lamp or Cherenkov emission — has to be first corrected for that effect before comparison. In addition, the Fresnel relations used to calculate the reflection coefficients are applicable to a specular surface. If the roughness of the physical CsI surface is such that its normal at the impinging point is no longer in the polarization plane of the incident photon, the polarization vector is then decomposed into p- and s-components, meaning a more important probability of reflection than the pure p-component. Therefore, the surface roughness of the CsI films was investigated (see Section 2.1.1.5) to check the validity of the specular assumption.

A direct measurement of the CsI QE versus the incident angle by Mine et al., shown in Fig. 2.4 [20], indicates a decrease of the QE as a function of the incident angle which becomes more pronounced at larger wavelength. A test set-up, to pursue studies of small CsI samples, will be completed at CERN in autumn 1998. It is described in Section 2.1.1.6.

QE measurements under gaseous media

The use of a solid photocathode in a MWPC imposes the evaluation of its quantum response under gas which is generally smaller than the QE measured under vacuum. Indeed, the collection efficiency of photoelectrons emitted into gas depends on the gas composition and pressure (p) [21], and can be considerably reduced by elastic backscattering from gas molecules. Also the electric field in the photocathode vicinity

plays an important role: at high field values the backscattering effect is almost totally suppressed [22]. The effect can be explained by the difference between inelastic and elastic collisions with gas molecules: in the first case the photoelectron trajectory is only slightly perturbed, while in the latter it is completely randomized, resulting in the backscattering towards the photocathode owing to the large mass difference between an electron and a gas molecule. This effect puts constraints on the detector operating conditions since the usually low reduced electric field E/p at the photocathode imposes a limited choice of gases. With the chamber geometry and operating voltage in use, the E/p value is 4 V/cm Torr^{-1} at the surface of the photocathode.

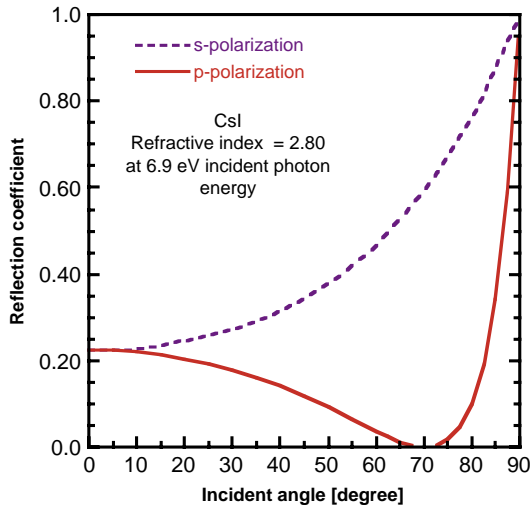


Figure 2.3: Reflection coefficient of a CsI layer as a function of the incident angle for s- and p-polarized light beam. Calculated from Fresnel relations for a specular surface.

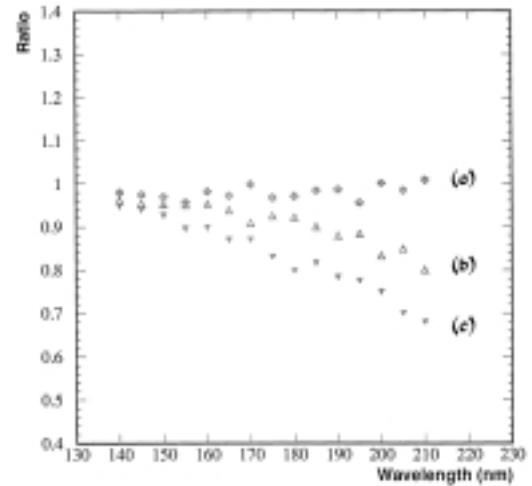


Figure 2.4: Ratio of the CsI QE measured under vacuum at an incident angle to that measured at normal incidence as a function of wavelength. The angles are: curve a) = 15° , b) = 45° , c) = 55° [20].

This effect has been extensively studied in the framework of the RD-26 project and all details about experimental set-up, measurement procedures, and results can be found in Ref. [23]. The CsI photoemission into gaseous media has been investigated, both, in laboratory using a UV source and in beam test, with a RICH detector using He-, Ar- and CH_4 -based mixtures [24].

In the UV tests both the single pulse counting and the DC current recording techniques were used. The single pulse counting technique allows the field to be varied at the vicinity of the CsI surface while maintaining the pulse detection efficiency. Thus we can compare the photoelectron collection efficiency measured at low electric fields, under ‘charge collection mode’, to the one observed in high electric fields, under ‘charge multiplication mode’ (relative QE measurement). Using the DC current recording, an absolute evaluation of the photoelectron collection efficiency is obtained by the ratio of the photocurrents measured in gas to that measured in vacuum, where the backscattering effect is absent.

The photoemission measured in He/ CH_4 (95/5) mixture by pulse counting on the charge collection plateau is about 60% less than on the charge multiplication plateau [25]. The photocurrent measured in DC mode, in the same gas mixtures, below the multiplication threshold, is reduced by the same factor with respect to vacuum (Fig. 2.5). Therefore, we deduce that at high electric fields, above a gas amplification of 100, the same photoelectron yield as in vacuum is obtained.

In CH_4 , the photoelectron collection efficiency in the charge collection mode, derived from the pulse counting, is about 90% of the value in the multiplication mode [25]. Also, in this gas, the gas-to-vacuum photocurrent ratio (~ 0.9 below multiplication, Fig. 2.6) is almost equal to the reduction factor estimated with the single-pulse counting technique. These experimental findings support the assumption that gas effects on the photoelectron collection efficiency are suppressed under charge multiplication.

Ar-based mixtures were studied only with the DC current recording technique. Pure Ar shows the same behaviour as He-based mixtures while in Ar/CH_4 (50/50) the photoelectron collection efficiency approaches that of pure CH_4 .

A Monte Carlo program simulating the photoelectron transport process from the photocathode to the anode has been implemented to reproduce and interpret the laboratory measurements [25]. The results are shown in Figs. 2.5, 2.6, 2.7 together with the respective measured gas-to-vacuum photocurrent ratios. The photoelectron collection efficiency is determined primarily by the ratio of elastic and inelastic collision frequencies: the larger the rate of inelastic collisions the lower the backscattering probability.

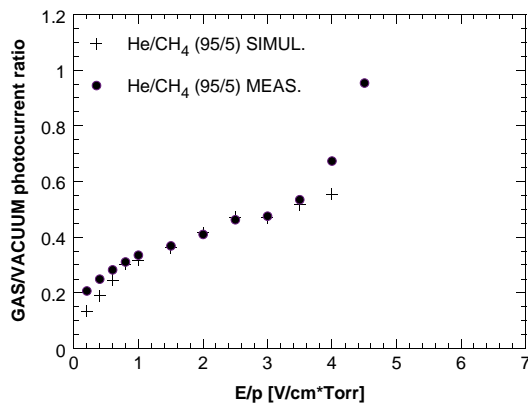


Figure 2.5: The ratio of the photocurrent from CsI, at 185 nm, in He/CH_4 (95/5) at 800 Torr, to that in vacuum (measured at the same absolute electric field) and the simulation results as a function of E/p at the photocathode surface.

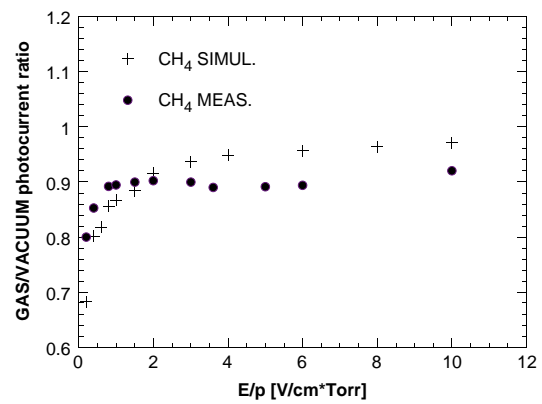


Figure 2.6: The ratio of the photocurrent from CsI, at 185 nm, in CH_4 at 800 Torr, to that in vacuum (measured at the same absolute electric field) and the simulation results as a function of E/p at the photocathode surface.

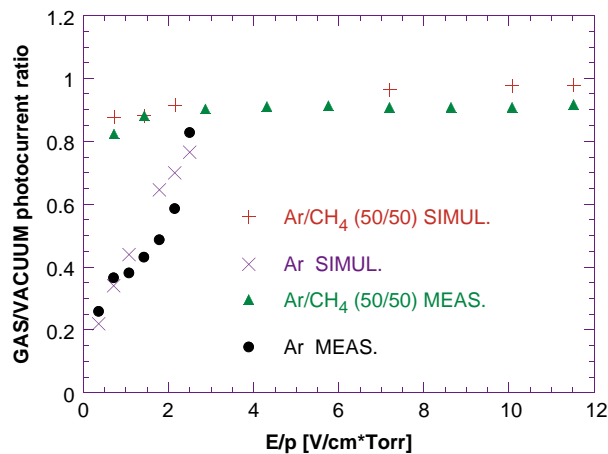


Figure 2.7: The ratio of the photocurrent from CsI, at 185 nm, in pure Ar and Ar/CH_4 (50/50) at 800 Torr, to that in vacuum (measured at the same absolute electric field) and the simulation results as a function of E/p at the photocathode surface.

Therefore the backscattering effect is particularly evident with noble gases where the lack of rotational and vibrational excitation levels makes the elastic channel the only one available at photoelectron energies below gas ionization thresholds. When the electric field at the photocathode surface reaches values high enough to start avalanche multiplication or there are polyatomic (hydrocarbon) gases, several inelastic channels become available, resulting in a suppression of the backscattering.

This study allowed us to verify the optimization of the MWPC operating conditions from the point of view of the Cherenkov photon total detection efficiency, confirming CH_4 as the best gas, since the electric field requirements for maximal photoelectron collection match well the high-voltage ranges providing a stable operation of the chamber.

2.1.1.3 Post treatment

So far, all teams involved in the processing of CsI films have followed the above evaporation procedures, considered necessary in order to produce photocathodes stable in time, but not expected to drastically change the QE performance. More controversial are the influence of the substrate and the conditioning. The conditioning, initially described by Anderson [26], consists in heating the photocathode, kept under vacuum after the evaporation to $50 - 60^\circ\text{C}$ for 4–6 hours. In addition, different configurations were tested such as flushing the vessel with CH_4 or C_2H_6 during the heating, varying the substrate temperature or the duration of the process. In Fig. 2.8, the enhancement of the QE with time is illustrated by a measurement made in the Weizmann set-up using a PCB substrate. A drastic increase in the QE was observed, mainly in the long wavelength range ($> 190\text{ nm}$), after heating the film to 60°C for 5 hours compared with measurements taken just after the evaporation. In addition, the films appear to have a better stability following exposure to air after conditioning. Such an effect was systematically reproduced by Breskin on a large number of different substrates, PCB included [27].

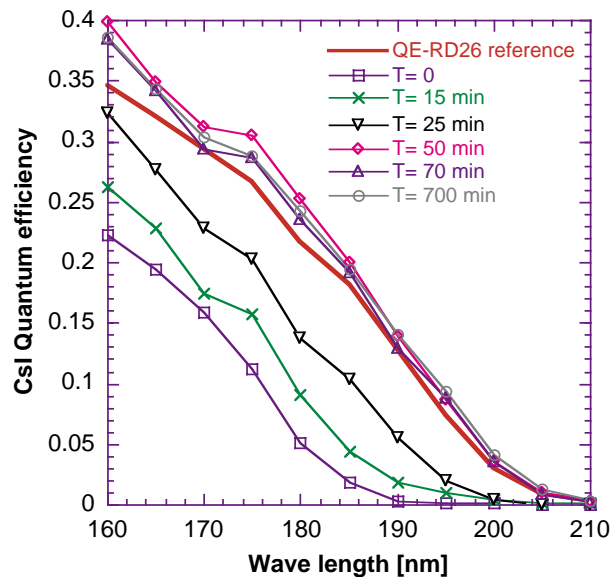


Figure 2.8: Effect of the heating of the CsI sample after evaporation at 60°C under vacuum. From $T = 0$ (the end of evaporation), an enhancement of the QE with time is observed. Measurements made at the Weizmann Institute using a CERN PCB substrate.

Following these tests on small samples in vacuum, a post treatment was systematically applied in the production of the large PCB photocathodes aimed at equipping the RICH detector. The post treatment consisted in evaporating on the pad cathode held at 50°C and in keeping under vacuum the fresh film at the same temperature for 6 to 12 hours. The positive influence of that treatment is illustrated later in Section 2.3.2.3 showing a substantial increase of the QE in our production of large photocathodes.

It should be mentioned that the positive influence of the post treatment was not observed by some authors [28]. A tentative explanation could be found in the fact that different substrates were used, such as aluminium, known for their peculiar surface structure usually porous and oxidized. Although several large photocathodes of high quality were later produced with a good yield, it is felt that deeper understanding of the processing should be still acquired in order to ensure a better control in the production of the 48 photocathodes needed in the HMPID system. For that purpose, an extension of the HMPID evaporation vessel has been built, described in Section 3.1.5, allowing for the evaluation of the photocathode immediately after its processing.

2.1.1.4 Exposure to air and ageing of small samples

After having reached the nominal QE value by applying the post treatment, J. Almeida et al. [29] exposed the sample to air and measured the variation of the QE with time. In Fig. 2.9, it is seen that a short exposure to air, less than 30 minutes, does not affect the QE.

Two processes are known to damage a CsI film: the exposure to a direct photon flux and the impact of ions when used in a MWPC. We shall not discuss the first case since it necessitates photon density of $10^{11} \text{ mm}^{-2} \text{ s}^{-1}$, far from our Cherenkov application, but we shall report on some investigations performed on the second one by Breskin et al. [7] and Krizan et al. [30].

Ageing studies of CsI photocathodes were done in a MWPC detector, having an anode plane made of $20 \mu\text{m}$ wires, with 2 mm spacing, placed 2 mm away from the cathodes and filled with pure methane. The chamber was illuminated with an Hg(Ar) lamp through air (dominant wavelength 185 nm) and the photocurrent was collected from both cathodes.

The photocathode ageing under a gas gain of 10^5 , was measured by monitoring the decay of the photocurrent. The illuminated area was 100 mm^2 and the total current density was limited to 0.05 nA/mm^2 , in order to avoid local space charge problems. The decay induced by photons only, measured at gain equal to 1, is of the order 20% after accumulated charge of 25 mC/mm^2 . As shown in Fig. 2.10, no visible drop of QE was observed by R. Chechik et al. (private communication) up to a 2.2 mC/cm^2 accumulated charge during a UV irradiation done at a chamber gain of 10^5 in CH_4 using an aluminized stainless steel substrate.

A summary of the status of CsI ageing studies can be found in [7] (Uppsala p. 116–136). Krizan et al. [31], observed some drop of QE obtained with CsI deposited on different substrates (Sn).

As reported in Section 2.3.2.7, the rate integrated over one month of Pb operation is expected to amount at 0.15 mC/cm^2 .

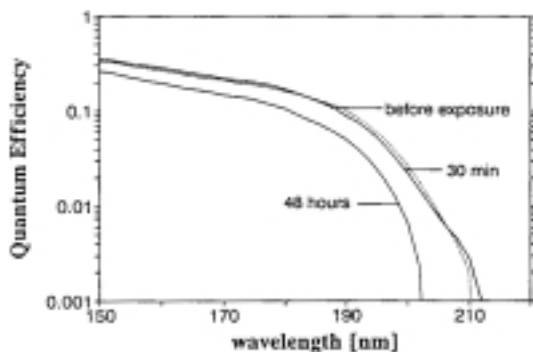


Figure 2.9: The decay of the QE of CsI layers evaporated on Ni/Au coated PCB under exposure to air at a relative humidity of 35% [29].

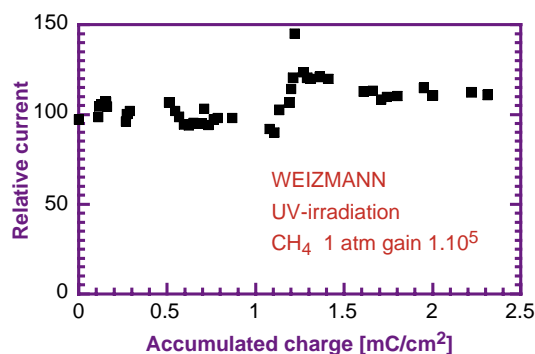


Figure 2.10: Ageing test under ion charge impact (R. Chechik et al., private communication).

2.1.1.5 Substrate and microstructural studies

Microstructural studies were undertaken in the RD-26 collaboration in an attempt to characterize CsI films by the observation of specific features using different physical probes. The aim was to correlate such features to a QE evaluation of the film and to serve as a quality control procedure. In addition, these studies are necessary in order to understand the underlying physicochemical ageing process. We shall report here only most important results. Some of these studies are still in progress thanks to a new instrument described in Section 2.1.1.6.

X-ray diffraction pattern (XRD)

The XRD probe has shown the effect of the copper substrate promoting the dissociation of the CsI [32]. In Fig. 2.11, a XRD pattern of CsI film deposited on Cu/Au is compared to the one obtained with a film deposited on a Ni/Au substrate. CsI lines are only observed on Ni/Au and are absent on Cu/Au where only some Cs lines are visible. It was also observed that the CsI film has a preferential crystallographic orientation along the $\langle 200 \rangle$ line.

CsI films were also observed under EDX and Auger probes in order to search for superficial contaminants. Carbon is found in variable thickness but essentially originating from the passage to air of the film before the measurement.

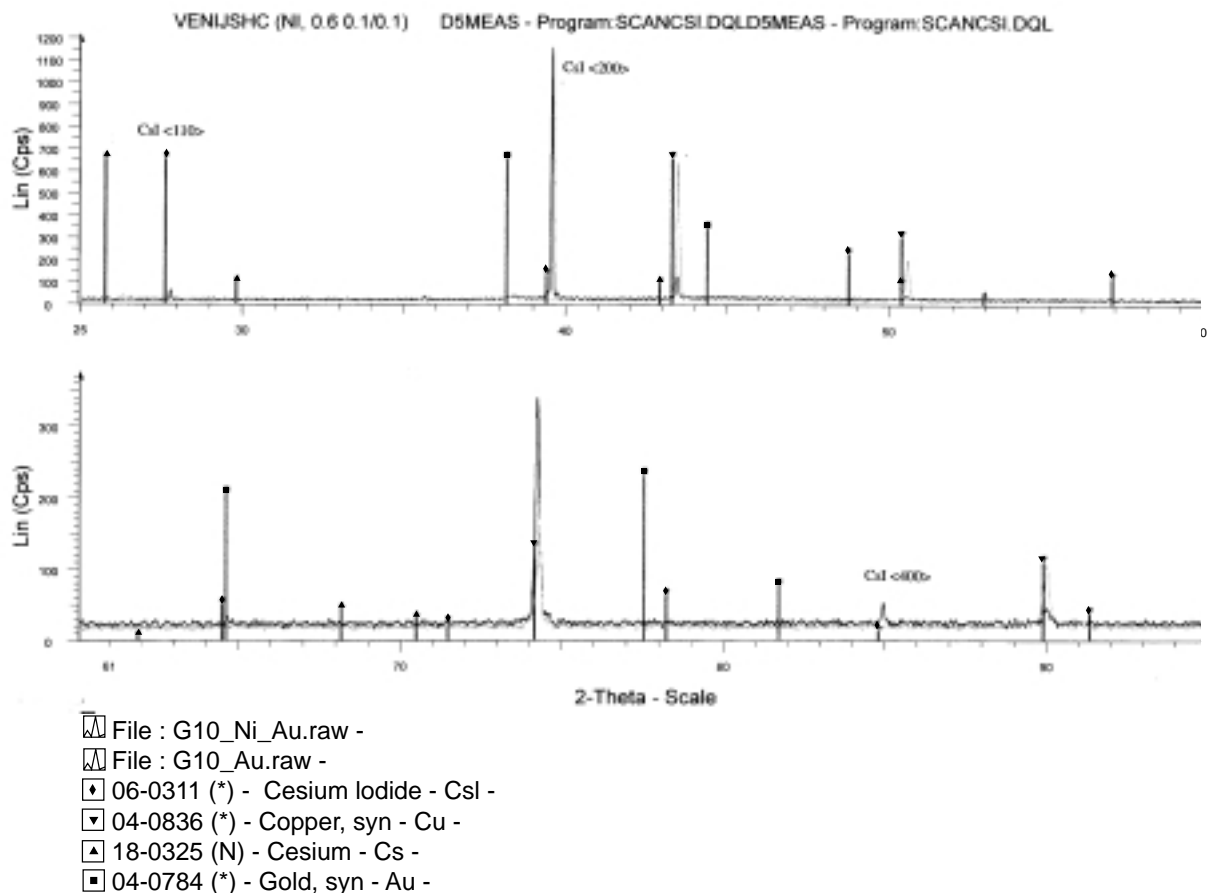


Figure 2.11: X-ray diffraction pattern of CsI coating (thickness 500 nm) on G10/Cu/Ni/Au and G10/Cu/Au substrates. The CsI peaks are visible only on the first substrate. Pronounced Cu peaks are visible on G10/Cu/Au.

Photoemission spectromicroscopy (PEEM)

These studies were performed by C. Coluzza and his team from the EPF Lausanne [17, 29, 33, 34]. They provide an image with a high lateral resolution of the primary and secondary electron emission of an area of $80 \times 80 \mu\text{m}^2$ of the sample using different excitation sources. The ESCA-300 instrument is using a source of AlK_{α} X-ray photons (1486.7 eV) for the excitation of Cs3d and I3d core level. Secondary electrons of very low kinetic energies (< 10 eV) were obtained by using a VUV deuterium lamp and some measurements were performed at the ELETTRA Sincrotrone in Trieste. These studies have demonstrated that inhomogeneities are found in the Cs to I stoichiometry up to the highest lateral resolution obtained with the scanning tunnelling microscope (100 nm range). A correlation has been found between the region enriched in I and a stronger secondary emission. The CsI dissociation due to copper-based substrate was also demonstrated.

Surface morphology

Surface morphologies were extensively studied using the Scanning Electron (SEM) and the Atomic Force (AFM) Microscopes. The textures of the films were analysed after varying substrate, evaporation procedure and other parameters. The growth of the film on the substrate starts from well-separated nucleation spots to reach a homogeneous coverage when the film thickness is larger than 100 nm. The process is described as a columnar growth [35] and the film surface appears as composed of grains more or less faceted. Extreme cases with macroscopic fractures and bad adhesion are observed on films evaporated on Cu substrates (Fig. 2.12a). Finding the parameters responsible for the size of the grains is a puzzling question. Is it a substrate- or an evaporation-related effect? In Fig. 2.13 one can see surface morphologies for different film thicknesses, showing the effect of the nucleation on the film coverage. CsI layers become continuous from a thickness larger than 100 nm. Only recently we have made SEM observations keeping the CsI film fully protected against air exposure from the evaporation vessel to the SEM vacuum chamber.

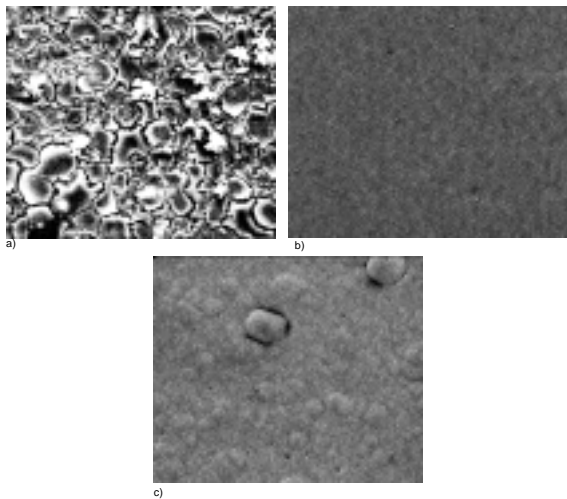


Figure 2.12: SEM images: $\times 2500$. CsI layers, 500 nm thick, deposited on various substrates: a) G10/Cu/Au, b) glass/Ni/Au, c) G10/Cu/Ni/Au.

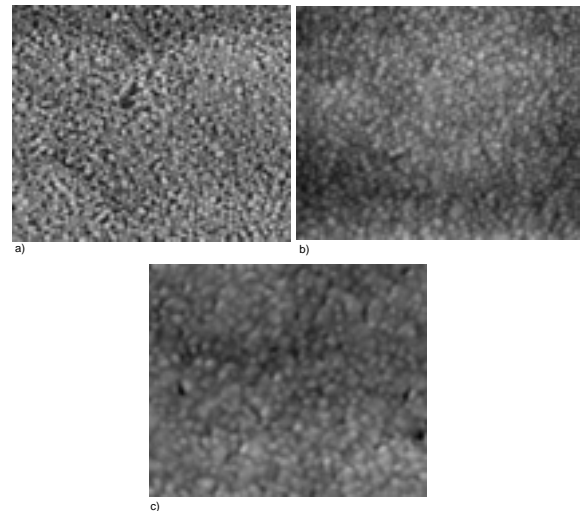


Figure 2.13: SEM images: $\times 25\ 000$. CsI layers deposited on G10/Cu/Ni/Au substrate at different thickness. a) 20 nm, b) 90 nm, c) 400 nm.

In Fig. 2.14, the texture of the non-exposed film is compared to the one observed after controlled exposures to a moist inert gas in the SEM chamber. Initially, the size of the grain is small, of the order of several hundred nanometers and increases significantly after a short exposure to moisture. The grains are also more faceted. After a longer exposure, the film becomes discontinuous and is composed of very large isolated grains.

That sequence is also shown on a thinner film, initially discontinuous, in Fig. 2.14d,e. These studies will be pursued using the experimental set-up ASSET, described in the next section, where the QE of the samples will also be measured.

In Fig. 2.15 we show a photo taken with the AFM at the Weizmann Institute. The surface profile and the lateral grain size obtained with this instrument allow the quantification of the specularity of the CsI surface and the derivation of the optical model needed to describe the reflective properties of the film (see Section 2.4). The surface roughness is found to be of the order of ± 20 nm and the lateral grain size to be 200–400 nm.

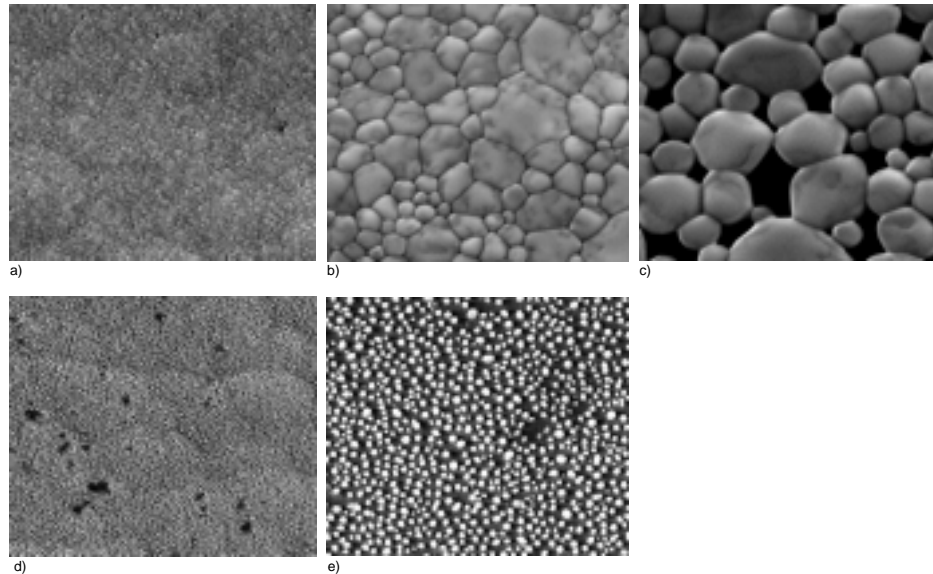


Figure 2.14: SEM images: $\times 10\,000$. Influence on the morphology of a CsI film of an exposure to argon at a relative humidity of 80% during a time T . Substrate: G10/Cu/Ni/Au. Series a, b, c: thickness 400 nm. a) $T = 0$, b) $T = 3$ min., c) $T = 5$ min. Series d, e: thickness 20 nm. d) $T = 0$, e) $T = 1$ min.

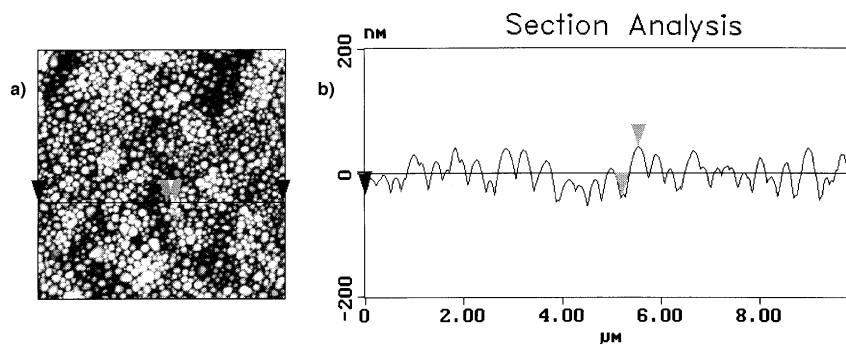


Figure 2.15: a) Atomic Force Microscope image of a CsI layer, 500 nm thick, deposited on a G10/Cu/Ni/Au substrate and b) roughness profile.

2.1.1.6 ASSET: A Small Sample Evaporation and Test facility

ASSET is a laboratory set-up to characterize small samples of CsI film ($1\text{--}10\text{ cm}^2$) by performing in the absence of exposure to air the sequence of operations and tests, i.e. evaporation, conditioning, QE evaluation, and storage in a container allowing clean transfer to any external measuring device, SEM, X-ray, etc. We shall be able to improve our present QE performance and possibly reach the higher values al-

ready demonstrated by several authors as best results. (See in Fig. 2.2, Seguinot et al. and also Krizan et al., Anderson et al. in Ref. [4]).

As seen in Fig. 2.16, the set-up is composed of two vessels, one used for film processing, the other for QE evaluation. They are separated by a vacuum valve to isolate one vessel from the other. An arm makes a linear transfer of the sample from one vessel to another and can also be rotated to vary the orientation of the substrate with respect to normal incidence. The angular effect on the growth of the CsI film and on the QE measured for inclined photons can thus be studied.

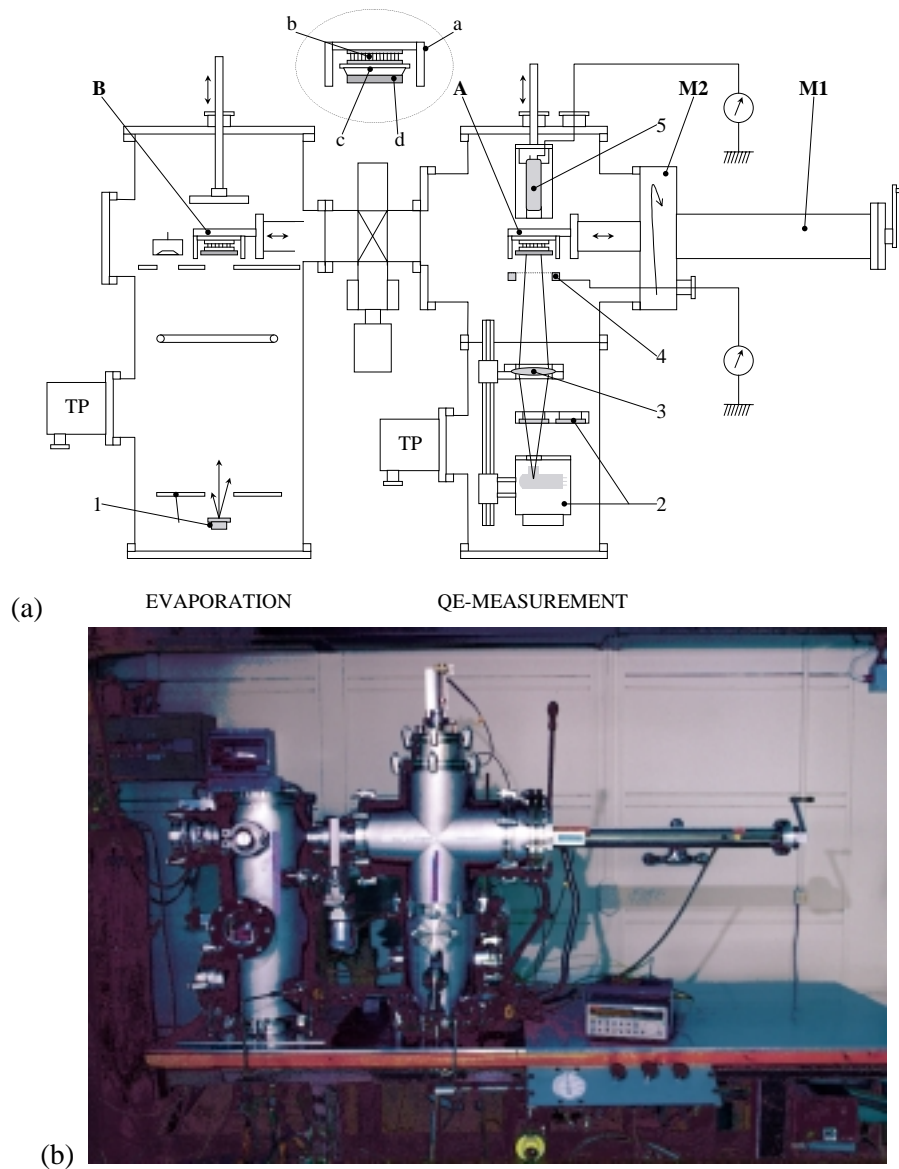


Figure 2.16: (a) Schematic of the ASSET system. The sample holder can be shifted from position B (evaporation vessel) to position A for QE measurement. M1 performs the linear transfer and M2 the sample orientation. Sample holder (seen in the expansion): a) protective box for transportation, b) Peltier elements for thermal cycle, c) insulation, d) substrate. In the evaporation vessel: 1) boat and shutter. In the QE measurement vessel: 2) UV lamp housing and interferential filter wheel; 3) CaF_2 lens; 4) photocurrent collection grid; 5) PM for photon flux calibration. (b) View of the ASSET system. The sample is coated with CsI in the evaporation vessel on the left side. Then, after operating the linear transfer arm seen on the right side, the sample is shifted from the evaporation vessel to the QE measurement vessel on the right side. The UV source is located inside and at the bottom of that vessel. One sees on the top the housing of the photomultiplier used for photon flux calibration.

Evaporation chamber

Three sources are available, supplied by independent high-current power units (12 V, 200 A, Sorensen model DCR 10-170B) to perform sequentially the evaporations of a clean substrate (Al, Au, etc.), a CsI film, and a protective coating (alkali halides). Each source has a manual shutter. A quartz crystal balance (Inficon model XTM/2) assures the monitoring of the thickness and rate of deposition of the films. The evaporation chamber is also equipped with a high-voltage glow discharge unit, to provide careful cleaning of the surfaces before evaporation by ion etching.

The linear transfer arm allows a 180° rotation, so that CsI can be evaporated on a tilted sample.

Test chamber

The QE of the CsI sample is obtained by measuring the photocurrent emitted by exposure to a monochromatic UV beam. The source is placed in the vacuum vessel. It is a deuterium lamp (Oriel model 63163) enclosed in a water-cooled aluminium box holding a wheel with four interference filters at 170, 180, 190 and 200 nm of ± 10 nm band width. After retracting the sample from the beam axis, the UV photon flux is evaluated by using a calibrated photomultiplier (Hamamatsu, R 1460) shifted along the beam axis and brought to the same location as the sample. The box is clamped to an optical rail that supports a diaphragm and a 50 mm CaF_2 lens providing a collimated beam of 4 mm diameter. A Rochon prism can be inserted to provide a polarized beam. The photocurrent is collected by a grid made of 15 μm diameter golden tungsten wires 1 mm spaced and held by a second rotary arm that can move the grid assembly out of the path of the arm when the sample is transferred into the evaporation chamber. A sapphire feedthrough is used to bring the photocurrent to a Keithley picoammeter.

Our programme is to repeat and improve some of the measurements described in Section 2.1.1.2: polarization and incident angle dependences; Section 2.1.1.3: post treatment; Section 2.1.1.4: ageing; Section 2.1.1.5: micro-structures in a set-up avoiding the exposure of the CsI film to air.

2.1.2 Single-electron detection using pad cathode readout in MWPC

2.1.2.1 The photodetector: choice of the geometry of the photodetector with pad CsI cathode

Given the high multiplicity expected in the HMPID photodetectors, a 2-dimensional readout is mandatory. Therefore we have considered only MWPC having a cathode readout segmented into pads. The pads will then be the only elements to be instrumented with electronics.

The photodetector has to locate as efficiently and accurately as possible single electrons emitted by the CsI film deposited on the pad cathode. In the case of single electrons, very small signals have the highest probability of being generated owing to the expected exponential pulse-height (PH) distribution, the small avalanche size, and the loss due to the anode/cathode coupling. Increasing the chamber gain to remedy this situation, has several limitations. The main one originates from the photon feedback (pf) mechanism. Depending on the chamber gas in use, the primary avalanche isotropically emits photons, which can in turn re-emit single electrons by hitting the CsI photocathode. Their number, N_{pf} , is taken to be proportional to the total avalanche charge Q_0 , that is the chamber gain G in case of a single electron, according to

$$N_{\text{pf}} = K_{\text{pf}} \cdot G . \quad (2.1)$$

Such a feedback can diverge at too high gain ($N_{\text{pf}} \approx 1$) and is also responsible for a background uncorrelated to the Cherenkov candidates.

Another limitation in gain is related to ageing since the impact on the photocathode of the ion clouds produced from each avalanche is the main source of degradation of the CsI film. Discharges, initiated by charging the CsI, could possibly occur at very high local irradiation rates even though CsI is proven to be a poor insulator.

The pad signal amplitude at a given gas gain can be increased by reducing the distance anode-to-pad in order to maximize their coupling: since, in our situation, that gap should be as small as a millimetre, or less, such a choice leads to undesirable technical problems in the feasibility and stability of large chamber area. Another way to gain in signal amplitude is to operate the FE pad electronics at the largest integrating time compatible with the expected local event rates.

We adopted the latter choice since the interaction rate expected at ALICE is maximum 100 kHz when running the experiment in proton mode and a few kHz in lead mode. It will be shown that such rates allow a long enough integration time of the FE electronics, > 700 ns, to get sufficient signal induced on the pads for efficient single-electron detection by still keeping a low anode-to-cathode coupling geometry thanks to the low detection threshold of the FE electronics in use. Hence, a 2 mm distance between anode and cathode has been adopted. In Section 3.1.1 the importance of that choice to ease the chamber construction is demonstrated. However, care should be taken not to increase the gap too much since the chamber is sensitive not only to single photoelectrons but also to particles depositing an amount of primary ionization proportional to the gap thickness.

The determination of the pad size is a compromise between the localization accuracy and the number of pad channels to be instrumented. Due to the low operation rate to be met in ALICE, the use of an analog multiplexed readout electronics is possible allowing for accurate localization by using charge centroid determination.

The smaller the pad size the more accurate centroid finding can be achieved, due to a larger fraction of clustered event patterns. However, a too small pad size would affect the detection efficiency.

The choice of a pad size of 8×8 mm² and of an anode pitch of 4 mm is indeed a compromise between the price of the electronics and the localization accuracy.

2.1.2.2 Chamber gain

In a MWPC geometry, shown in Fig. 2.17, a single electron extracted at the abscissa x of the cathode 1 (lower), generates an avalanche of charge Q_0 concentrated, in the case of low gain and no secondary photonic effect, at a point of the sense wire defined by the angle α . In the motion of Q_0 towards the cathode 1 during a time t , the charges $q_-(t)$, $q_{+1}(t)$, $q_{+2}(t)$ are induced on the sense wire, cathode 1 (lower) and 2 (upper), respectively. According to Vávra's nomenclature [36], these quantities are referred to as 'visible gain' when measured at t_{integ} , while Q_0 is the total gain reached when t_{integ} equals the total ion drift time, (> 10 msec). In order to evaluate the photon feedback yield (Eq. 2.1), Q_0 must be deduced from $q_{+1}(t)$ measured at t_{integ} .

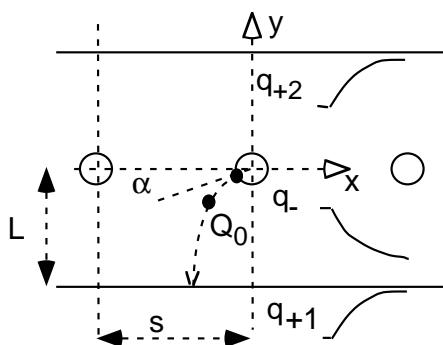


Figure 2.17: Schematics of the charges q induced by the motion of a charge Q_0 in a MWPC geometry.

For that purpose, a first correction factor for $q_-(t_{\text{integ}})$ is obtained from the equation of motion of Q_0 in the MWPC field structure, assuming a known constant ion mobility. An example of such a curve is shown in Fig. 2.18 for the case of methane, indicating an increase by a factor of approximately 2 in signal amplitude between $t_{\text{integ}} = 20$ and 600 ns for the same gap. Operating our FE electronics at $t_{\text{integ}} \approx 1$ μ s,

we have taken the value of $q_-(t_{\text{integ}})/Q_0$ equals 0.5. A second correction factor takes into account the fraction, q_{+1}/q_- of the charge induced on the pad cathode. When the gap is small, this factor depends on the angle α , that is on the location of the electron emission. Arnold et al. [37] have measured a 15% variation for a 0.67 mm gap, which is the order of magnitude of the error expected when determining Q_0 by measuring $q_{+1}(t)$ without knowing the location of emission. However, the spatial extension of Q_0 , assumed to be punctual in the calculation, should reduce the spread of $q_{+1}(t)/Q_0$.

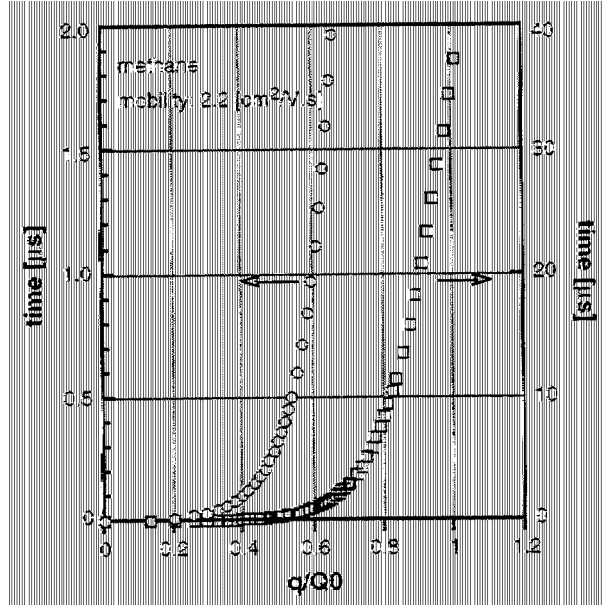


Figure 2.18: Time dependence of the ratio of the charge q induced at the anode wire to the total charge Q_0 moving towards the cathode calculated in methane in a 2 mm gap MWPC geometry. The plot on the right indicates that Q_0 is fully collected in about 40 μs ; the one on the left, that after 1 μs , 60% of the Q_0 value is induced at the anode wire.

2.1.2.3 Charge distribution on the pad cathode and avalanche position evaluation

The evaluation of the distribution of the induced charge on the cathode plane is an electrostatic problem which can be solved by considering the signal induced on the electrodes by a positive point charge as a function of spatial coordinates. For a given MWPC geometry, different models provide the parametrization of the geometrical spread of induction [38–41]. In particular, that of Gatti [38] describes the distribution of the induced charges along the anode wires taking into account the signal finite sampling related to the cathode strip segmentation, the capacitive coupling among strips, and the amplifier white noise. In that model the fraction $\Gamma(\lambda)$ of the total charge at a given normalized coordinate $\lambda = x/D$ in the sense wire direction (where D is the anode-cathode gap), is:

$$\Gamma(\lambda) = K_1 \frac{1 - \tanh^2(K_2 \lambda)}{1 + K_3 \tanh^2(K_2 \lambda)}, \quad (2.2)$$

where K_1, K_2, K_3 are parameters depending on the chamber geometry.

Mathieson et al. [42] have demonstrated that, in a chamber with symmetric gap, the charge distribution may be considered approximately symmetrical in the two directions, perpendicular and parallel to the wires, and that $\Gamma(\lambda)$ may be conveniently described in terms of K_3 only, the three parameters being related by the following relations:

$$K_2 = \frac{\pi}{2} \left(1 - \frac{1}{2} \sqrt{K_3}\right), \quad (2.3)$$

$$K_1 = \frac{K_2 \sqrt{K_3}}{4 \arctan(\sqrt{K_3})}. \quad (2.4)$$

The free parameter K_3 may vary between 0 and 1 depending on the wire diameter and on the ratio of D and the wire pitch [43]. Figure 2.19a shows the induction shape obtained with $K_3 = 0.68$, corresponding to the proto-2 geometry.

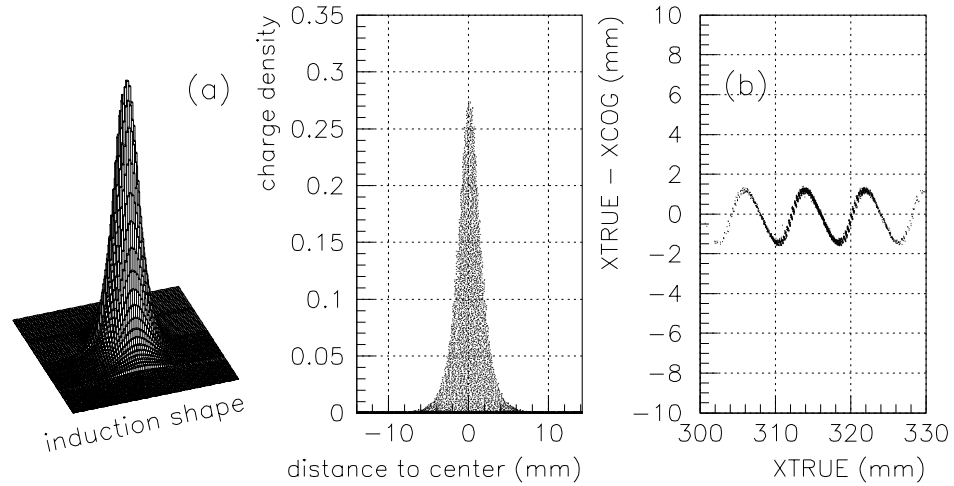


Figure 2.19: (a) Two-dimensional shape (left) and projection in one direction (right) of the charge distribution on the pad cathode. (b) Non linearity in the residuals distribution as a function of the true particle impact on 8 mm pads (the edges of the central pad are positioned at 312 and 320 mm).

Depending on the total charge developed in the avalanche (and on the pad size), in some fraction of the events the signal will be shared on more pads. In that case the average position of the avalanche, in the direction parallel to the wires, can be estimated with the centre of gravity (or *centroid*) of the charge distribution:

$$x_c = \frac{\sum_i (Q_i - B) x_i}{\sum_i (Q_i - B)} \quad (2.5)$$

for $Q_i > B$, where x_i and Q_i are, respectively, the cluster i -th pad x coordinate and measured charge; $B = b \sum_i Q_i$ is a threshold level allowing the influence of electronic noise to be reduced. The value of b has to be determined empirically so as to eliminate the contributions from small pulse-height channels, where the noise signal can be predominant, but also to avoid loss of information, if b is too high. With accurate studies, Piuz et al. [44] have pointed out that the influence of the parameter b on the evaluation of the localization accuracy has a periodic dependence on the avalanche position, with period equal to the pad width. In particular, the largest error corresponds to positions at 1/4 or 3/4 of the pad, while the maximal accuracy is obtained when the avalanche is in the middle of the pad or at the edge between two pads (Fig. 2.19b). A value of $b = 0.015$ seems to be a reasonable compromise to achieve better localization. The y_c coordinate, perpendicular to the anode wires, is discrete since it corresponds to the position of the wire on which the avalanche has developed, a position that can be deduced from the cluster shape and the induced signal distribution.

2.1.2.4 Detector response to single electron

Modelling

The shape of the pulse-height distribution obtained from Single-Electron Pulse-Height Detection (SE-PHD) is usually found to be purely exponential at low gas amplification whatever the gas mixture, obeying

the Furry distribution:

$$P(A) = \frac{1}{A_0} \cdot \exp - \left(\frac{A}{A_0} \right), \quad (2.6)$$

where A and A_0 are the current and the average pulse heights, respectively. If A_{th} is the detection threshold of the FE electronics, the single-electron detection efficiency is simply given by:

$$\epsilon_{\text{det}} = \exp - \left(\frac{A_{\text{th}}}{A_0} \right). \quad (2.7)$$

The knowledge of that distribution is essential for further simulation of the detector behaviour. The mean value of the SE-PHD has been taken as the parameter characterizing the photodetector response all along our tests. In the following, these quantities are expressed in ADC channel units, easily converted into charge unit (fC) by means of an electronics calibration.

The departure from the exponential Furry shape indicates that a fraction of the avalanches originate from more than one single electron. The mechanisms responsible are discussed in the next section. In that case, a more general pulse-height generator to fit the experimental distributions is a normalized Polya distribution [45] characterized by two parameters, A_0 and θ , according to

$$P(A) = \frac{1 + \theta}{A_0 \cdot \Gamma(1 + \theta)} \cdot \left[\frac{A}{A_0} (1 + \theta) \right]^\theta \cdot \exp - \left[\frac{A}{A_0} (1 + \theta) \right] \quad \text{with} \quad 0 < \theta < 1. \quad (2.8)$$

or

$$P(A) = \frac{(1 + \theta)^2}{A_0 \cdot \Gamma(1 + \theta)} \cdot \left[\frac{A}{A_0} (1 + \theta) \right]^\theta \cdot \exp - \left[\frac{A}{A_0} (1 + \theta) \right] \quad \text{with} \quad -1 < \theta < 0. \quad (2.9)$$

In the case of $0 < \theta < 1$, $(1 + \theta)$ is the averaged number of primary electrons per avalanche. In the case of low amplification, the Polya distribution turns to a simple exponential distribution (Furry law).

These distributions are represented in Fig 2.20.

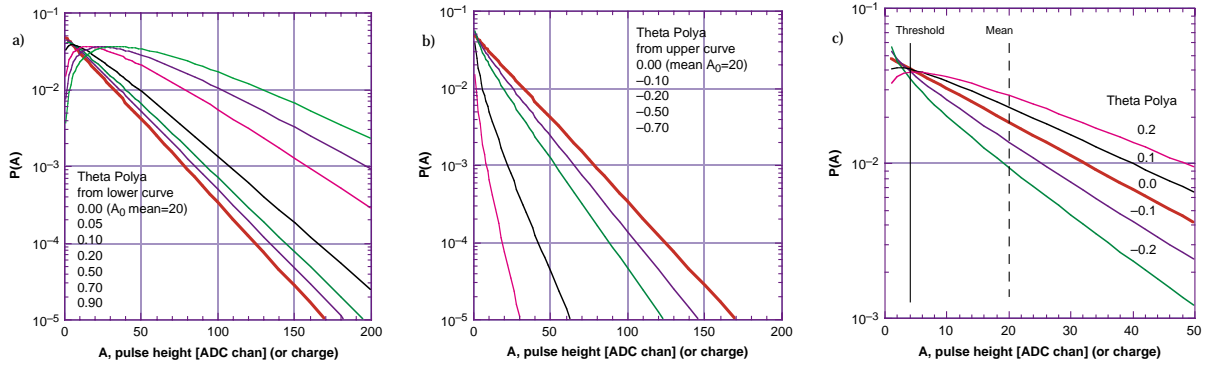


Figure 2.20: Representations of Polya distributions calculated from formulas Eqs. 2.8 and 2.9 with the mean single-electron pulse-height, $A_0 = 20$ ADC channels. In (a) and (b), positive and negative θ values are taken, respectively. (c) indicates the parts of the spectra experimentally recorded when applying a threshold cut at 4 ADC chan. At values $-0.2 \leq \theta \leq 0.2$ we observe mainly a change in the slope of the exponential.

Examples of measured SE-PHD

In standard operation of wire chambers (no CsI cathode), secondary electrons are generated from the conversion in the chamber gas of photons emitted by de-excitation processes from the primary avalanche. These secondary-emission photon mechanisms are quite complex depending on the gain and the gaseous species involved. In practice, while increasing the chamber gain, the exponential Furry distribution is modified into a Polya distribution having θ value either positive or negative.

Mixtures exclusively composed of hydrocarbon gases (CH_4 , C_2H_6 , $i\text{C}_4\text{H}_{10}$) lead to a concave shape, associated with a positive θ value. Noble gases are generally emitting energetic photons, usually absorbed by the admixture of a ‘quenching’ component, typically a hydrocarbon gas. It is observed that a convex shape characterizes poor quenching property, typical of noble-gas-based mixtures (argon, helium), associated with a negative θ value [36].

In addition to the gaseous generation from the primary avalanche in poorly-quenched mixtures, secondary electrons are also produced by feedback photons when CsI coated cathodes are used. In the case of CH_4 , photons are emitted from excited carbon atoms according to three lines at 156, 166, 193 nm in the ratio 30, 57, 13 [46]. In absence of quenching admixture, CH_4 is transparent to these photon energies leading to a photon feedback yield of $N_{\text{pf}} = 7.7 \times 10^{-6} \times G$ [47], where G is the gain of the primary avalanche (Eq. 2.1). Therefore, the Polya model cannot be applied as described above since θ is not anymore a constant but a function of the individual avalanche gain i.e. of the induced pulse height: the higher the individual amplification, the more feedback photons produced.

This is illustrated in Fig. 2.21 by SE-PHDs measured in different gas mixtures with CsI-coated cathodes. Standard Polya fits are applied to the spectra providing A_0 and θ values. The Furry curve of mean A_0 are superimposed on the measured spectra. Contrary to what is seen in Fig. 2.20, in case of negative θ , high PHs are found in excess to the Furry curve with a poorly quenched mixture. In turn, using the less transparent $i\text{C}_4\text{H}_{10}$ cuts off two of the three carbon lines (see transmission curve in Section 2.1.3) and the SE-PHD (Fig. 2.21d) has a positive θ but shows a lack of high PHs with respect to the Furry curve, illustrating its known ‘quenching’ ability.

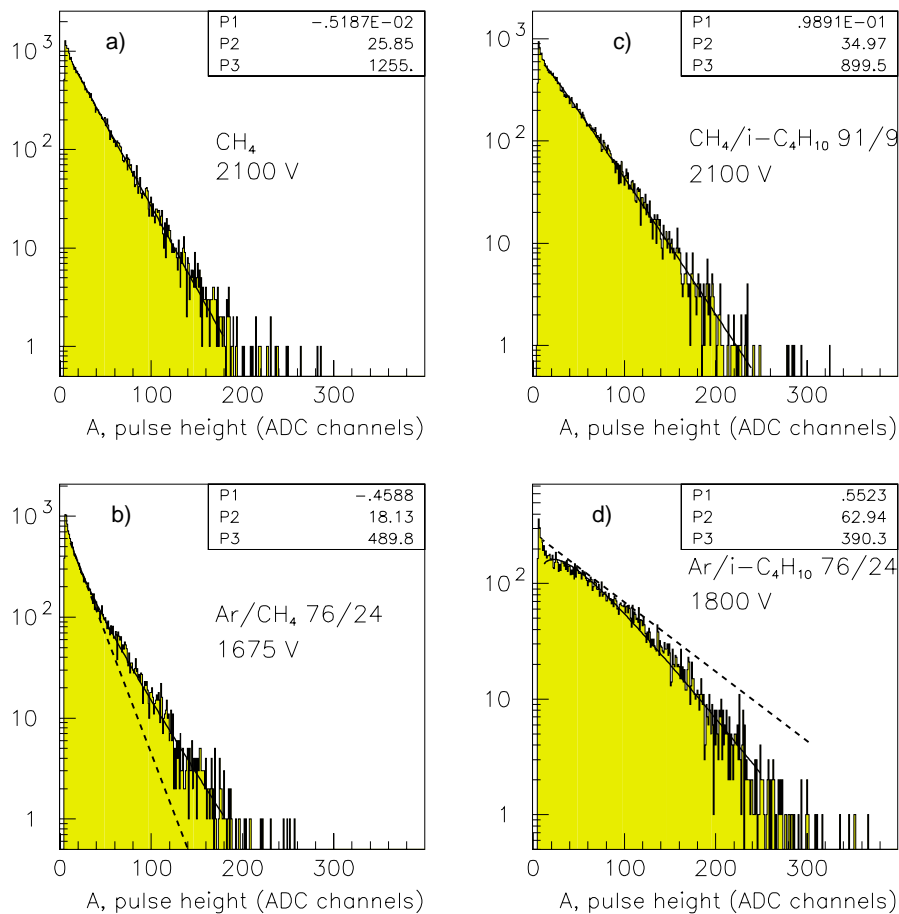


Figure 2.21: Single-electron pulse-height in different gas mixtures. A fit with the Polya distribution function is shown, with parameters P1: θ and P2: A_0 . In b) and d) hatched lines are the Furry curves with mean A_0 .

In our experimental geometry and at a maximum gain of 5×10^5 , the yield of photoelectrons in CH_4 is expected to be 0.3–0.4 per avalanche, assuming QE between 0.2 and 0.3 and a the solid angle for electron emission of about 1.5π srad.

2.1.2.5 Evaluation of the photon feedback yield

A method for evaluating the photon feedback yield in any gas mixture has been developed [48] and currently applied to check the critical parameter $K_{\text{pf}} = 7.7 \times 10^{-6}$ proposed by Arnold et al. [47] for hydrocarbon mixtures.

For this purpose, a pad cathode was half-covered with CsI and photoelectrons were extracted using a well-collimated UV source (deuterium lamp) from two spots, distant by about 10 cm, one coated with CsI and the other one not coated, in order to compare the resulting SE-PHDs. The two spots are located along the same sense wire, used as a trigger for the pad electronics in both cases. Measurements, shown in Fig. 2.22, were obtained using a MWPC with a pad size of $8 \times 8 \text{ mm}^2$, 2 mm anode to cathode distance, 4 mm anode pitch and CH_4 , $i\text{C}_4\text{H}_{10}/\text{CH}_4$, Ar/CH_4 as gas mixtures. The SE-PHDs measured at the two spots at different voltages were fitted to Polya distributions providing the θ values plotted in Fig. 2.23a. Indeed, the adjunction of CsI results in making the θ values more negative than the one obtained with bare cathodes. To simulate these measurements, by varying K_{pf} , a proportion of photon feedback photons is added to a primary SE-PHD obtained from the fit of the no-CsI SE-PHDs until the θ value measured at the CsI spot is reproduced. Figure 2.23b shows the simulated θ values obtained for different K_{pf} values. A reasonable agreement with the measurements is obtained for a K_{pf} value of 7×10^{-6} , close to the one quoted in [47].

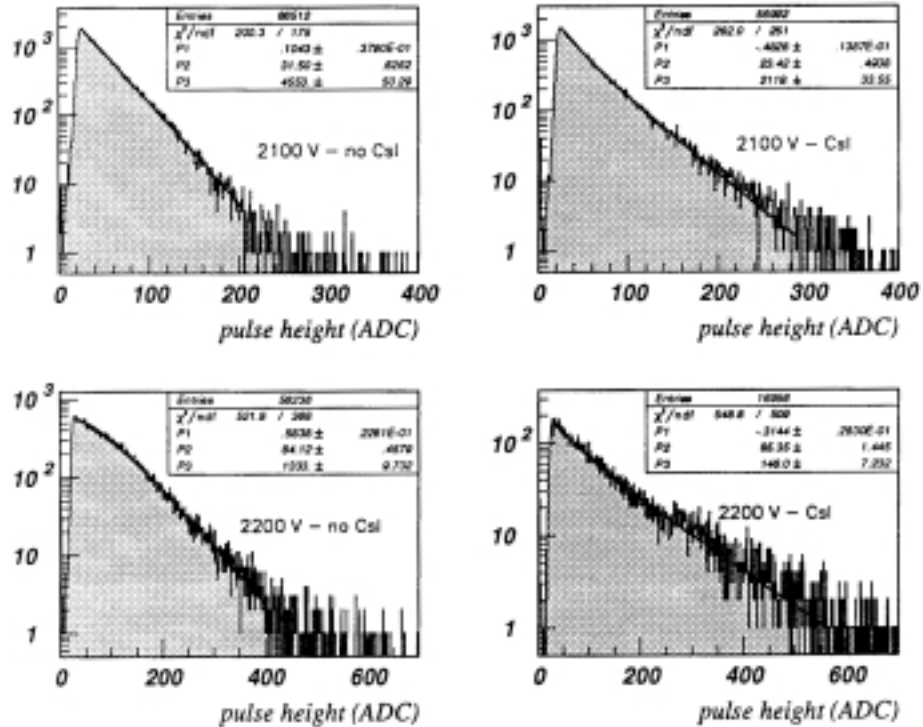


Figure 2.22: PH spectra of single electrons emitted from a cathode spot surrounded (right column) or not (left column) by a CsI coating, measured at two chamber gains in CH_4 . The constant θ and A_0 of the Polya fit are the values P1 and P2, respectively.

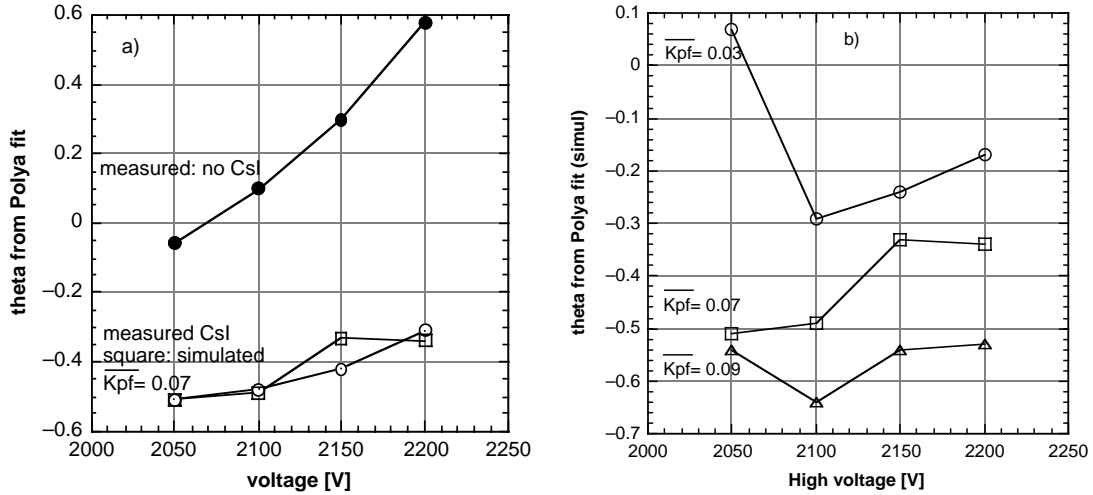


Figure 2.23: a) Having simulated SE-PHDs at different values of the feedback constant K_{pf} and made the Polya fits, the corresponding θ values are plotted as a function of the chamber gain. b) Plot of the θ values obtained from spectra measured at the two spots (CsI and no-CsI). For the presented set of CsI data the best fit is obtained with $\overline{K}_{pf} = 0.07$. In these plots, \overline{K}_{pf} is expressed in experimental charge unit (ADC channel). This value corresponds to $K_{pf} = 7 \times 10^{-6}$.

In conclusion, the Polya distributions are used as convenient analytical tools only for the purpose of fitting SE-PHDs, without attributing its usual physical meaning to the θ constant. For simulation purposes, a Monte Carlo generation is used, based on the feedback constant, $K_{pf} = 7.7 \times 10^{-6}$ and a Furry curve with mean A_0 .

However, for a pure methane, the Polya curve corresponding to small θ values, (0.1 – 0.2), still shows a quasi-exponential behaviour but of a different slope than the Furry curve, as seen in Fig. 2.20c. In addition, the tiny maximum expected at very low PH is usually masked by the applied threshold making it hardly visible in the SE-PHD.

2.1.3 Measurements of basic physical RICH parameters

Besides the CsI photodetector, the Cherenkov radiator medium is the other major element constituting the CsI RICH. Given the momentum range under study at ALICE, 1 to 5 GeV/c, only a liquid radiator could be considered. Liquid C_6F_{14} was selected for the achievable Cherenkov angular resolution, tolerable technical constraints, and affordable cost. In addition, its UV transparency threshold, at about 165 nm, presents an acceptable match to the CsI QE curve (Fig. 2.24a,d).

The main physical properties of C_6F_{14} are reported in Section 3.1.3.2. The remaining components, the chamber gas and the window containing the liquid, should have UV transparencies at least comparable to the that of the liquid C_6F_{14} . Pure CH_4 satisfies such requirement while iC_4H_{10} , if not pure enough, or contaminated by water vapour and oxygen, might reduce the transparency range (Fig. 2.24c,d). The purity control of the chamber gas aims to guarantee that the fractions of O_2 and H_2O are kept at the lowest level also in order to minimize the contamination of the CsI photocathode. High-quality primary gases are used (class 38 to 45). The impurity checks are performed with commercial instruments from Hermann-Moritz for O_2 and Shaw for H_2O . In the case of C_6F_{14} or iC_4H_{10} , the achievement of optimum transparency necessitates active filtering; in particular the options for the C_6F_{14} purification system will be described in Section 3.1.3.4.

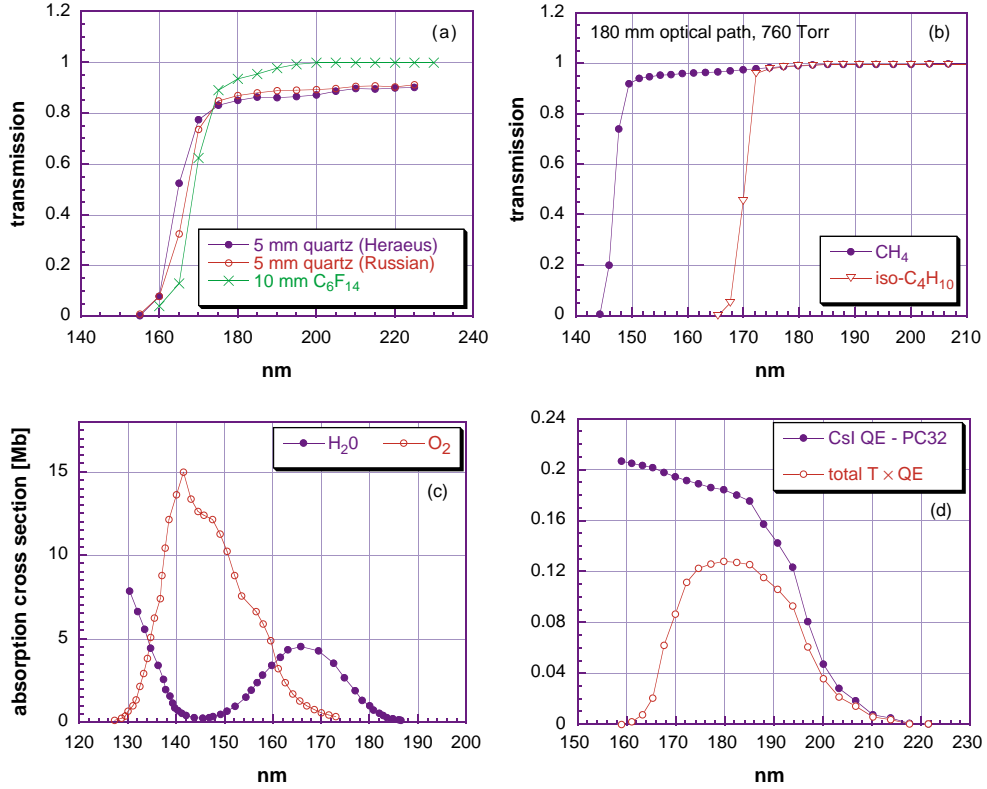


Figure 2.24: (a) Measured UV transmission of 10 mm C₆F₁₄ and 5 mm quartz plates (not corrected for reflection losses). (b) UV transmission of CH₄ and iC₄H₁₀, calculated from [49] and [50] respectively, for a photon path of 180 mm equivalent to a distance travelled in a proximity gap of 103 mm by Cherenkov photons emitted in C₆F₁₄ by $\beta = 1$ particles. (c) UV absorption cross section of oxygen [51] and water [52]. (d) PC32 QE evaluated from simulation (Section 2.4.2) and the convolution with the total media transmission.

The window of the radiator vessel containing the liquid C₆F₁₄ raises some problems since the final area of the container will be half a square metre. High-quality synthetic quartz, such as a Suprasil-Standard UV Grade from Heraeus, has an acceptable transparency, considering the C₆F₁₄ cut-off, and, in addition, it can be delivered with the necessary polishing in plates of size 45×45 cm², 5 mm thick. Figure 2.24a shows the UV transmission of quartz samples, from Heraeus and St Petersburg Optical Institute. The C₆F₁₄ and quartz transparencies were measured at CERN using a dedicated set-up put at our disposal by A. Braem, CERN.

The quartz window refractive index has been measured by the supplier Heraeus and fits with the following parametrization, which can be found also in Ref. [52]:

$$n_{\text{qz}}^2(E) - 1 = \frac{F_1}{E_1^2 - E^2} + \frac{F_2}{E_2^2 - E^2}, \quad (2.10)$$

where $E_1 = 10.666$ eV, $E_2 = 18.125$ eV, $F_1 = 46.411$ eV⁻² and $F_2 = 228.71$ eV⁻².

2.1.3.1 C₆F₁₄ refractive index

The radiator refractive index and its dispersion are basic parameters for the Cherenkov angle reconstruction and the evaluation of the achievable angular resolution. The radiator refractive index is related to its physical properties by the Lorentz–Lorenz equation [52]:

$$\frac{n^2 - 1}{n^2 + 2} = \alpha f(E); \quad (2.11)$$

$f(E)$ is the molar refractivity (in terms of the energy E) and $\alpha = 0.3738\rho/M$ where ρ is the density (in $\text{g}\cdot\text{cm}^{-3}$) and M is the molecular mass.

In the far-UV range, 150–200 nm, only a few measurements are available (Fig. 2.25) [52, 53]. The oldest measurement, from J. Seguinot and T. Ypsilantis, was limited to the range 195–250 nm; in Fig. 2.25 an extrapolation up to 160 nm is shown, according to the relation used to fit the experimental data, which has a linear behaviour with energy:

$$n(E) = a + b \cdot E, \quad (2.12)$$

with $a = 1.2177$ and $b = 0.00928 \text{ eV}^{-1}$. Such a curve does not reproduce our beam-test data: at the average wavelength of detected Cherenkov photons of 181 nm the index is 1.28127, a value corresponding to an average ring radius of 144.5 mm (for $\beta = 1$ particles and a proximity gap of 103 mm), instead of the observed 156 mm (Fig. 2.34k). The value needed to obtain the right ring radius (and to reconstruct correctly the Cherenkov angle), at the average detected wavelength, is $n = 1.2948$. The index dispersion was adjusted in order to get, in simulated events, the correct spread of the ring radius and the reconstructed Cherenkov angle distributions (Section 2.3.2.5). Indeed a and b have been estimated with a trial and error method, taking into account all the tunable parameters (namely the photon feedback and the CsI quantum efficiency); the estimated values giving the best fit to data are: $a = 1.177$ and $b = 0.0172 \text{ eV}^{-1}$. The corresponding curve is shown in Fig. 2.25, where also the recent DELPHI measurements at 27.5 °C are reported (data published by courtesy of E. Fokitis, S. Maltezos and P.G. Moyssides [53]).

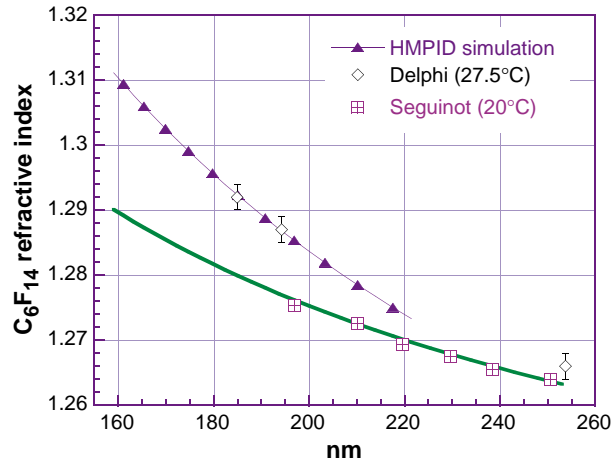


Figure 2.25: The C_6F_{14} refractive index. The Seguinot [52] and DELPHI [53] values come from measurements, while the HMPID curve has been used in a Monte Carlo simulation to reproduce RICH beam-test data. The fit to the Seguinot data with: $n = 1.2177 + 0.00928 \cdot E$ (eV) is also shown.

Even taking into account the correction for the different temperatures to which the two sets of data refer (Eq. 2.11), their agreement is still good. Indeed the experimental error quoted for the DELPHI index corresponds to an uncertainty of about 4 °C, using a coefficient $dn/dT = -5 \times 10^{-4} \text{ }^\circ\text{C}^{-1}$ given by the supplier. On the other hand the system monitoring the temperature at the experimental radiator vessel inlet and outlet has indicated a gradient of $\sim 2.5 \text{ }^\circ\text{C}$ at an ambient temperature, measured at the inlet, of 22.5 °C (the heating is very probably due to the front-end electronics dissipating about 100 Wm^{-2}).

Another factor that could play an important role is the purity of the liquid (Section 3.1.3.2).

These remarks prompted the construction of a dedicated monitoring apparatus to measure the C_6F_{14} refractive index that will be part of the ALICE C_6F_{14} circulation system. That device is under development and will be available in 1999.

2.2 Overview of the CsI-RICH prototypes and modules

The first constraint for the HMPID module layout is that its full size is reached by particles with incident angle in the range $\pm 10^\circ$, taking into account the overall tilt of the modules, as shown in Chapter 1, Fig. 1.1 on page 2. Given the distance to the vertex, a $1.33 \times 1.28 \text{ m}^2$ sensitive area fulfils that requirement.

A second constraint is given by the size of our present CsI evaporation station that allows for handling substrates of a maximum area of about $60 \times 60 \text{ cm}^2$ to minimize the investment on that device. Since no severe requirement is imposed on the detector dead zone, the whole CsI photocathode area has been partitioned into panels of size $60 \times 40 \text{ cm}^2$ as shown in Fig. 2.26.

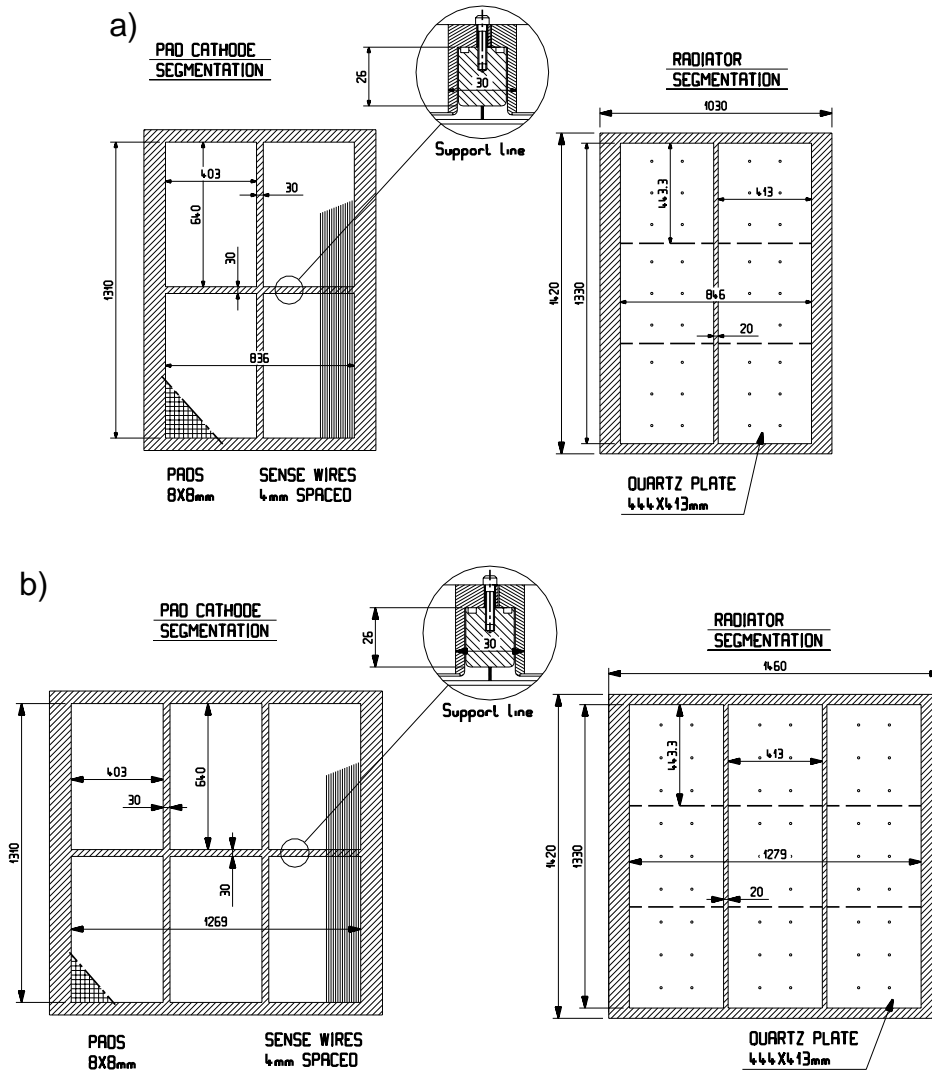


Figure 2.26: Schematic layout of proto-2 (a) showing the CsI pad panel and radiator trays segmentations. Proto-2 corresponds to 2/3 of a full size HMPID module which is shown in (b). The dead zones represented by the crossing rods correspond to 5% of the total area.

A third constraint is that the pad panel has to be easily detachable from the detector in order to perform the processing of the CsI film followed by several mounting and dismounting operations. Therefore, one has to make it as an independent element with flatness and stiffness such that the chamber gap is not affected by these operations.

The choice of a 2 mm anode-to-cathode gap satisfies the previous requirement. In fact, a $\pm 40 \mu\text{m}$ tolerance, i.e. $\pm 2\%$ of the gap, in the machining of the frame and the flatness of the panel is sufficient to

guarantee a uniform behaviour of the chamber. Such mechanical specifications are still practicable with simple and affordable technologies. Also, the diameter of anode wires can be kept at $20\ \mu\text{m}$ to simplify the weaving and ensure the stability of the anode plane. The dead zones hence created to hold the CsI pad panels ease in turn the segmentation of the radiator array, made out of three independent trays overlapping the sensitive pad areas.

During the development phase (RD-26), three early small prototypes were built in order to define the wire chamber geometry and the associated FE electronics [54–56]. They were used to evaluate our first CsI photocathodes of $26 \times 10\ \text{cm}^2$ area [57]. Subsequently, two large prototypes were assembled, referred to as proto-1 and proto-2 (see Fig. 2.27).

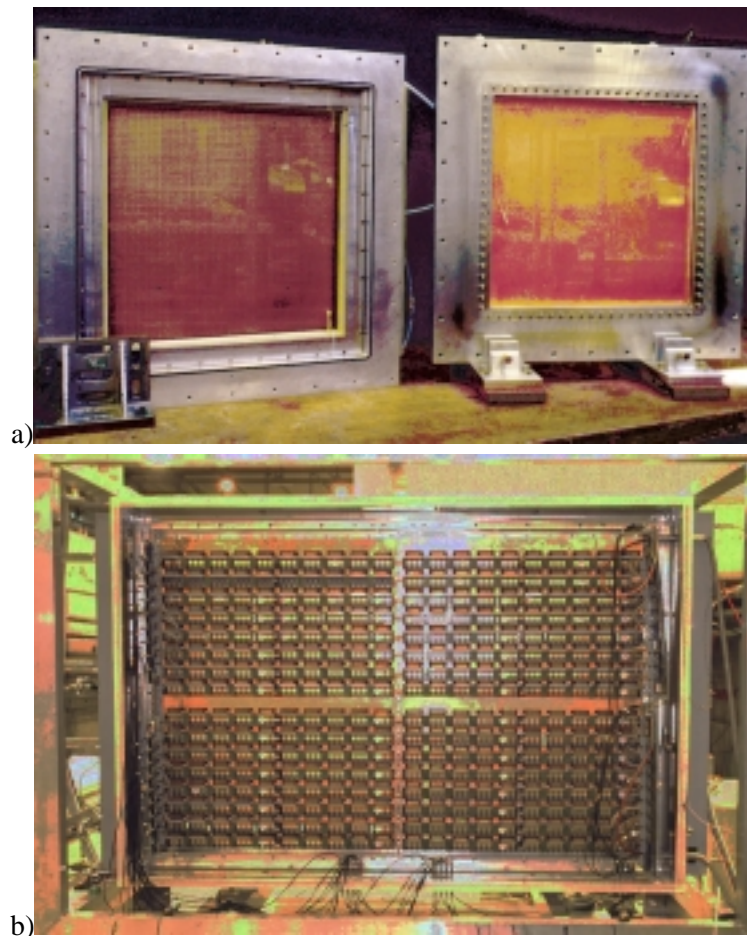


Figure 2.27: a) View of proto-1. On the left side, one sees the photodetector with a pad panel of 56×60 pads and on the right side the radiator vessel enclosed by a quartz plate of $440 \times 460\ \text{mm}^2$. b) Proto-2 viewed from the pad panel side. The four independent pad panels instrumented with GASSIPLEX chips can be distinguished.

With proto-1, pad CsI-photocathodes of size up to $50 \times 50\ \text{cm}^2$ were studied at the test beam using small C_6F_{14} or NaF radiators convenient for single-particle tests. Proto-2 is already a part of a final HMPID module, (two-thirds of the full size). All the essential elements, the anode length, pad CsI-photocathodes ($64 \times 38.4\ \text{cm}^2$), FE electronics and radiator trays ($133 \times 41.3\ \text{cm}^2$) are implemented in their final version. Proto-2 was tested under single and multiparticle irradiation. All the papers published in the HMPID group during the R&D phase, related to beam-test results or system descriptions, are found under references [58–64]. The detailed description of proto-2 and its equipment is found in Section 3.1 since there were no major conceptual differences between proto-1 and proto-2 except the area.

Table 2.1 summarizes the main geometrical parameters and equipment of the different prototypes tested during our R&D period. For all of them, the pad size was of $8 \times 8 \text{ mm}^2$ and the anode pitch of 4 mm.

Table 2.1: Main geometrical parameters of the CsI RICH prototypes

Proto	gap (mm)	CsI PC size (pad)	No. FEE channels	CsI PC size (cm^2)	Radiator medium	Radiator area (cm^2)
Small-1	var.	24×12	288	19.2×9.6	NaF	20
Small-2	2	32×12	384	25.6×9.6	NaF, C_6F_{14}	20
Proto-1	2	40×36	1 440	32.0×28.8	NaF, C_6F_{14}	20
		60×56	3 360	48.0×44.8		
Proto-2	2	80×48	15 360	64.0×38.4	C_6F_{14}	6×20
		(4 times)		(4 times)		5500
						2×5500

2.3 CsI RICH performance

2.3.1 Test beam facilities and test layouts

All our CsI RICH tests were carried out at two test beam facilities: T11 at the East Hall and H4 at the SPS, North Area.

2.3.1.1 T11 test set-up: proto-1, partial proto-2

At T11, the slow PS-extraction on a target provides a secondary beam composed of mixtures of protons/pions using positive magnet polarities or pions/electrons with the other polarity. The available momentum ranges from 1.0 to 3.5 GeV/c with a $\Delta p/p$ of 1%, the duration of the burst is 300 ms.

Figure 2.28 shows our set-up. Two crossed plastic scintillator doublets (PM1,2–PM3,4), 2 m apart define our trigger geometry covering an area of 1 cm^2 of the detector with a beam divergence $\leq 1 \text{ mrad}$. The beam rate was set to 10 kHz/cm^2 . A Time-of-Flight (ToF) array composed of two scintillators, 10 m apart, was used to identify pions from protons present in the beam (Fig. 2.29).

The six-fold coincidence of these scintillators defines the physics trigger signal and the ToF identification used at the software level. The CsI RICH is placed on a table allowing for X/Y translation and vertical rotation. The anode wires are horizontal in the set-up.

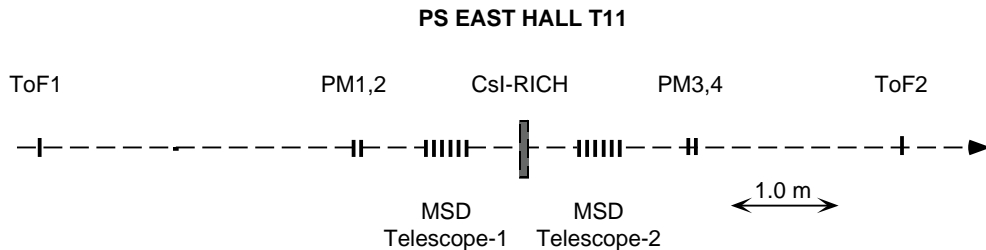


Figure 2.28: Experimental layout used at the PS/T11 test beam.

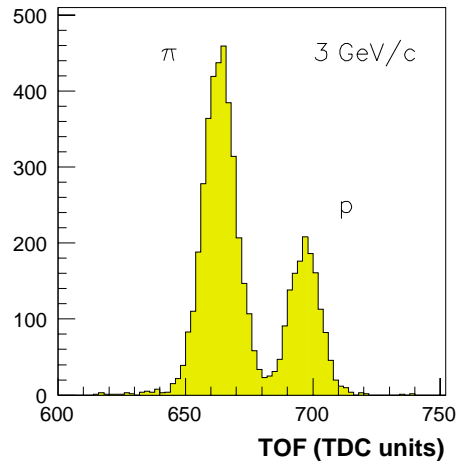


Figure 2.29: Time-of-flight spectrum obtained at the PS/T11 test beam (pi /proton).

In order to study the pad response, the detector was interleaved between two telescopes composed of six planes of microstrip silicon detectors of $50\ \mu\text{m}$ pitch providing an accurate localization, $15\ \mu\text{m}$ r.m.s., of the particle impacts in the pad plane.

The gas mixtures were supplied from primary sources of purity better than 99.98%. Copper tubes were used and the mixture was circulated through Oxysorb and Hydrosorb cartridges. The flow was usually 30–40 l/h. The contaminations were continuously controlled by a Hermann–Moritz oxymeter and a Shaw hygrometer to the ppm level at the output of the detector. While not in operation, the detector was kept under constant argon purge.

The radiator array is fixed to the plate closing the detector. Its position can be adjusted relative to the CsI photocathode plane, allowing for varying in situ the Cherenkov radius. Two kinds of radiating media could be installed. One was a circular plate of NaF, 50 mm diameter, 10 mm thick. The second one was a vessel circulated with C_6F_{14} . The output window was made of a quartz Suprasil plate of 3 mm thickness, 50 mm diameter. The effective thickness of C_6F_{14} could also be adjusted continuously from 0 to 15 mm by moving an opaque foil inside the liquid screening the Cherenkov photons emitted before it. The total volume of liquid was 1 litre. The tightness was achieved with Viton O-rings.

The C_6F_{14} was supplied by 3 M company (DELPHI RICH supplier). It was circulated by using a magnetic circulator at a flow of 0.5 l/h through fully metallic tubings. Several filters were necessary to achieve the best UV transparency: we used a molecular sieve and activated copper. The best results, corresponding to Fig. 2.24(a) were achieved with the molecular sieve alone. A test cell equipped with two CaF_2 windows was inserted in the C_6F_{14} circuit in order to measure the UV transparency.

The first small RICHs and proto-1 were tested at T11 to study CsI photocathodes of size $30 \times 30\ \text{cm}^2$. In 1997, the four final large photocathodes were successively evaluated using proto-2 with small radiators.

The elements of the electronics system in use are described in Section 3.1.4. The pad panel of proto-1 was equipped with 6 boards of 15 GASSIPLEX, corresponding to 240 channels per board. A scheme of the DAQ system is shown in Fig. 2.30.

2.3.1.2 H4 test set-up: proto-2

Since 1997 ALICE groups have been carrying out tests in the SPS H4 beam line. It can receive standard hadron SPS beams up to $450\ \text{GeV}/c$ and runs dedicated extracted lead beams at $158\ \text{GeV}/c$ per nucleon. The zone is shared with the NA57 experiment. It was foreseen to perform here the final test of the large proto-2 under multiparticle events of high density obtained by interaction on target.

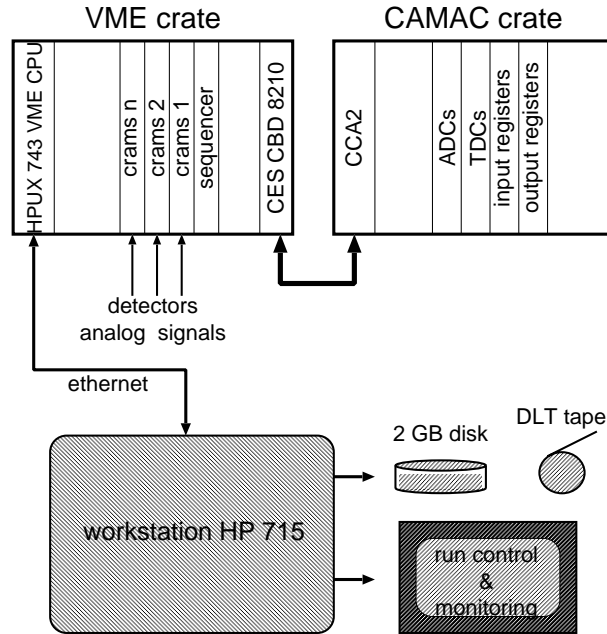


Figure 2.30: Schematic of the DAQ system used at the PS/T11 test beam line. The VME modules used to perform digitization and zero suppression are CAEN-CRAMS V550 and a Sequencer Unit V551.

The layout of the experimental set-up is shown in Fig. 2.31. Starting from upstream, it is composed of the following elements:

- A first scintillator doublet providing beam coincidence in a sensitive area of $5 \times 5 \text{ mm}^2$.
- A veto array for upstream interactions made of four scintillators $20 \times 20 \text{ cm}^2$ providing two- or four-fold coincidences as veto signals. The array has a hole in its middle to let the beam pass through.
- A target holder, remotely controlled with several targets Be, Pb and MT.
- An interaction array, identical to the veto array, providing various interaction trigger signals (two- and four-fold coincidences).
- A telescope of four pad chambers used to reconstruct the trajectories of the secondaries emitted by the target. Its final configuration is seen in Fig. 2.31 and the chamber acceptances listed in Table 2.2: The projected acceptance of that telescope covers only half of the proto-2 area. Results are shown and analysed in Section 2.3.2.6.
- The large proto-2, located on a movable stage with remote control in horizontal and vertical motions. The anode wires are horizontal.
- A second scintillator doublet providing beam coincidence with a sensitive area of $5 \times 5 \text{ mm}^2$.

For these tests, proto-2 was equipped with four large CsI photocathodes, with one and subsequently two full-size C_6F_{14} radiator trays.

Gas mixtures were supplied to proto-2 by a system identical to the one described at the T11 test set-up. In addition to the contaminant control, a system to detect traces of electronegative gas was implemented, with the aim to monitor possible leaks of the C_6F_{14} from the radiator trays surrounded by the chamber gas. The prototype of the ALICE C_6F_{14} circulation system, described in Section 3.1.3 was put in operation feeding one or two radiator trays.

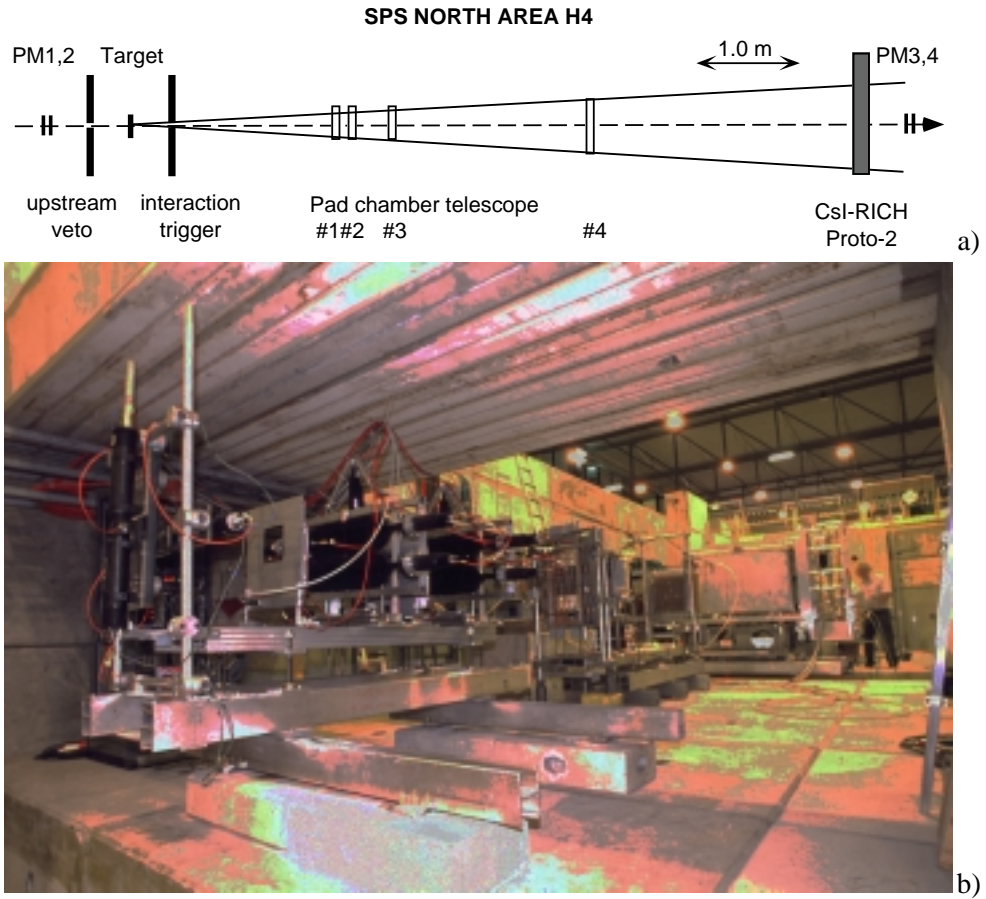


Figure 2.31: a) Experimental layout used at the SPS/H4 test beam. b) General view of the test set-up at the SPS H4 beam line. Following the trigger array and the pad chamber telescope, proto-2 is installed on a translation stage.

Table 2.2: Geometrical parameters of the telescope pad chambers

MWPC	Anode wire	Coord. centroid	Pad size (mm ²)	Pad cathode size (pads)	
				X	Y
1	vertical	Y	8 × 8	30	× 32
2	horiz.	X	8 × 8	32	× 30
3	horiz.	X	8 × 8	40	× 36
4	horiz.	X	8 × 8	56	× 60

The elements of the electronics system in use are described in Section 3.1.4. Each pad panel was equipped with 8 rows of 2 GASSIPLEX-1.5 15-chip boards plugged in a horizontal position such that the readout is propagated in a direction parallel to the anode wires. The readout was organized by horizontally daisy-chaining boards belonging to 2 adjacent pad panels, forming a super-row of 60 chips, i.e. 960 channels. This way, a total of 16 super-rows were read out by 8 CAEN V550 modules, i.e. 15 360 channels. The behaviour of this system is reported in Section 3.1.4.

The pad telescope chambers were also read out by the same electronics, adding eight V550 modules. The DAQ system is the same as the one of the T11 test set-up. The low voltage and current supplying the GASSIPLEX and the HV current of the chamber were constantly monitored.

2.3.2 Results from the PS and SPS beam tests

2.3.2.1 Introduction

The goal of these tests is to understand and optimize the detector in order to achieve the best angular Cherenkov resolution and:

- a) to guarantee a stable and sustainable operation of the detector under the expected ALICE conditions of irradiation;
- b) to demonstrate that the pattern recognition of very dense events (50 particles per square metre) is achievable.

We have concentrated the analysis, modeling and simulation studies after the experimental results (see Section 2.4). The reader may wish to start reading that section first.

The performance of a RICH detector is characterized by the well-known equation [52]:

$$N_{\text{phel}} = L \cdot N_0 \cdot \sin^2 \theta_c , \quad (2.13)$$

where

$$\cos \theta_c = \frac{1}{n\beta} , \quad (2.14)$$

$$N_0 = 370 \cdot \epsilon_{\text{det}} \cdot \int QE(E) \prod_i T_i(E) dE . \quad (2.15)$$

Here N_{phel} is the number of Cherenkov photoelectrons, L is the radiator thickness, θ_c is the mean Cherenkov angle over the detected photon energy spectrum (established by the traversed media transmissions T_i), ϵ_{det} is the single electron detection efficiency and N_0 is the detector factor of merit.

That number has to be as large as possible since the Cherenkov ring angular resolution is expressed as $\sigma_{\text{ring}} = \sigma_{\text{phel}} / \sqrt{N_{\text{phel}}}$, where σ_{phel} is the angular resolution per Cherenkov photoelectron. In turn, σ_{phel} is determined by variables intrinsic to the detector layout that are in our case the radiator chromaticity, the radiator thickness (since we have no focusing geometry), and the localization accuracy of the photoelectrons.

As shown in a ring pattern in Fig. 2.32, every single electron is identified as a pad cluster providing submillimetric localization along the wire direction if its size is ≥ 2 pads. Given our large pad size, a compromise is to be found between high localization accuracy, requiring large cluster area, and accurate photon counting, requiring small clusters well separated to avoid overlap. Of course, the larger the Cherenkov radius, the less the statistical geometrical overlap with limitations imposed by the pattern recognition as seen in Fig. 2.33.

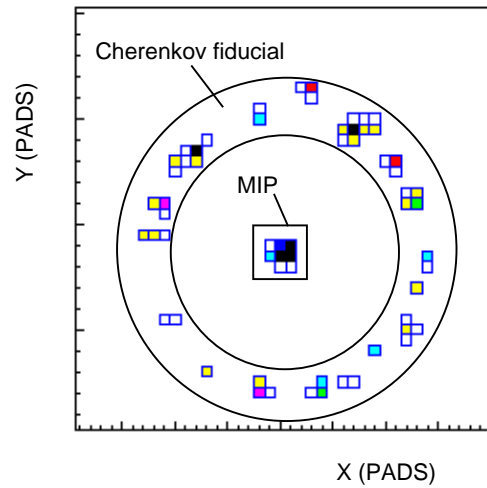


Figure 2.32: Single Cherenkov ring event with the three zones used for cluster finding.

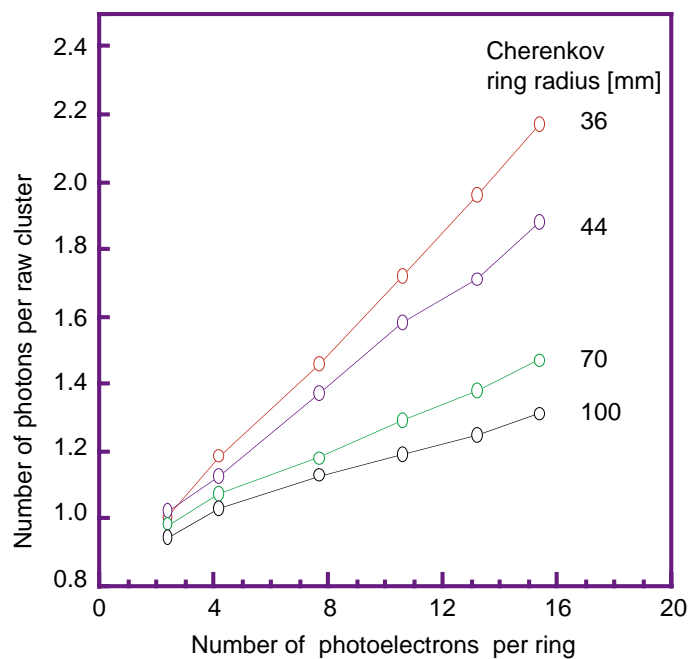


Figure 2.33: Simulated probability for geometrical overlap of Cherenkov clusters as function of the number of clusters per ring for different ring radii. (No photon feedback contribution.)

In addition, specific to the use of CsI photocathode, one expects a number of photoelectrons produced by photon feedback to contaminate the Cherenkov pattern by cluster overlap.

These remarks determine the variables to be extracted from the experimental data and used in the data analysis codes. Let us first introduce these variables to present typical experimental data while the data analysis code detailing their definitions is found in Section 2.4.

As seen in Fig. 2.32, the pad array is divided into three zones: a zone surrounding the particle impact, a Cherenkov fiducial ring zone, and the rest of the pattern corresponding to background hits. They are referred to as MIP, fiducial, and background zones, respectively. The variables listed below can be independently analysed for the three zones of the pad array:

- a) N_{pad} : is the total number of hit pads (threshold dependent) per ring.
- b) N_{raw} : the number of raw clusters per ring: a raw cluster is defined as a pad pattern having all pads adjacent by at least one edge. Above a certain size, it might be formed of several overlapping single patterns.
- c) N_{res} : the number of resolved clusters per ring: a resolved cluster is assumed to correspond to a single Cherenkov photoelectron according to deconvolution algorithms.
- d) N_{tot} : total number of single electrons (Cherenkov and photon feedback) inside a fiducial Cherenkov area.

Since the mean single electron PH, A_0 , is obtained from resolved clusters, the ratio of the total pad PH measured inside the ring fiducial zone over A_0 provides N_{tot} whatever the cluster overlaps are.

2.3.2.2 Main results

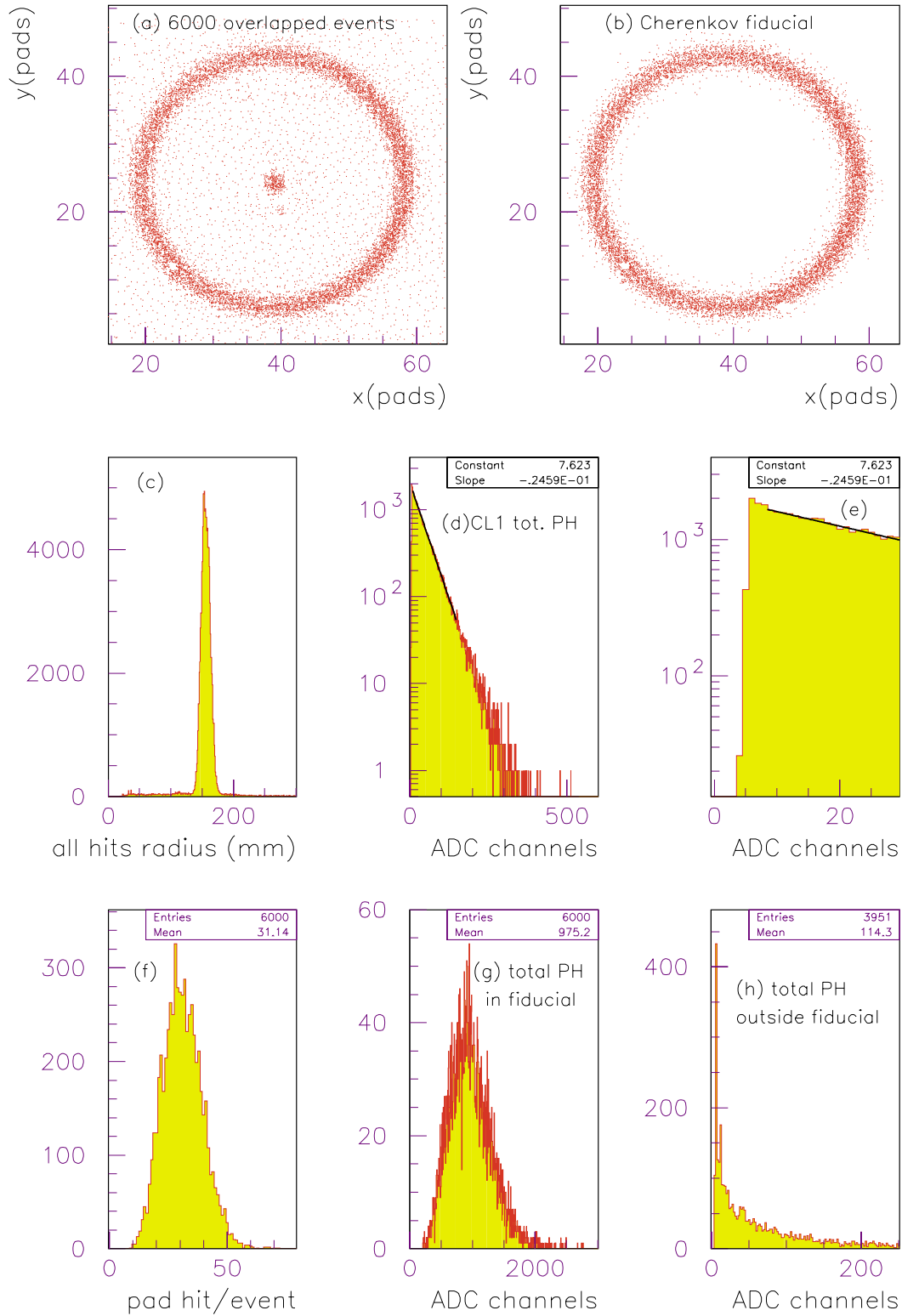
Experimental distributions

For evaluating CsI-photocathodes, the standard test procedure was to take the following sequence of measurements using single particle events:

- a) pedestal measurement at every run;
- b) at a given radiator thickness, make an HV scan;
- c) at a given HV, make a radiator thickness scan (when the convenient radiator set-up is installed).

Different impact position, incident angles, ring radius, gas mixtures, beam rates were taken as primary conditions for the scans. Empty radiator runs were also useful for studying the detector response to MIPs in the absence of Cherenkov events. In order to control the stability of the PCs, such measurements were repeated periodically over a long period of time (four years maximum).

At first, we show in Fig. 2.34 the basic distributions characterizing a run. In particular, in the plot (e) that is a zoom-in at low PH values of the SE-PHD shown in (d), the steep edge of the distribution represents the mean threshold value achieved by the FE electronics. As discussed in Section 3.1.4, this value is of 3–5 ADC channels, corresponding to 4–5 times the sigma of the noise distribution. Then according to Eq. 2.7, applicable in case of single-electron PH spectrum, the single-electron detection efficiency is represented in Fig. 2.35 as a function of the single-electron mean PH.



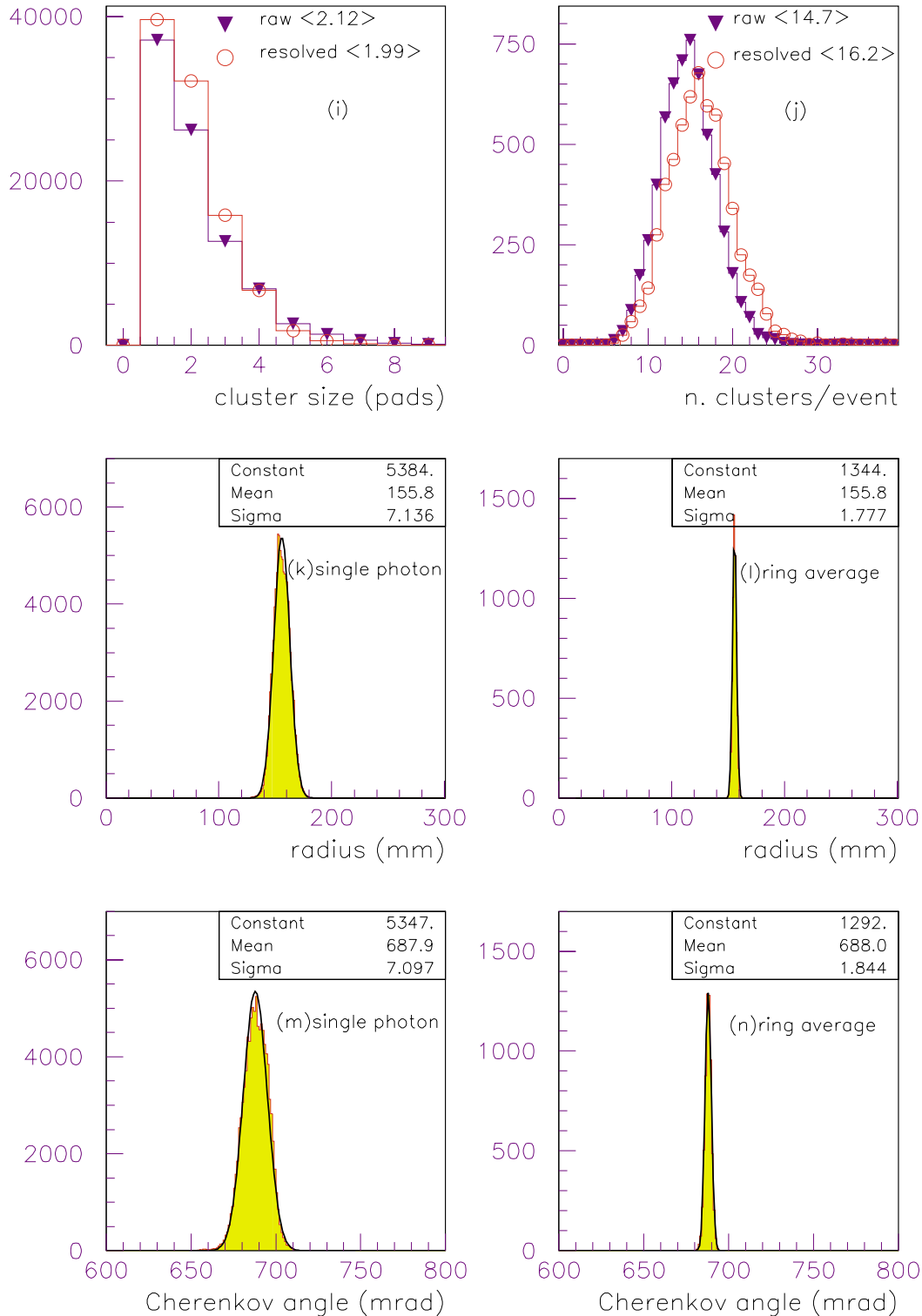


Figure 2.34: RUN2075, SPS beam test, 350 GeV/c π , PC32, 2100 V, 6000 events: two-dimensional display of (a) fully overlapped events and of (b) Cherenkov fiducial zone; (c) hits distance from MIP impact, showing the low background level; (d) single-electron PH spectrum and (e) the lower part of the same spectrum with the PH threshold in evidence; (f) number of hit pads and (g) total PH in fiducial per event; (h) total PH outside the Cherenkov fiducial; (i) size and (j) frequency of raw and resolved clusters in fiducial; (k) single-photon and (l) ring average radius distributions; (m) single-photon and (n) ring average reconstructed Cherenkov angle distributions. One ADC channel corresponds to 0.17 fC.

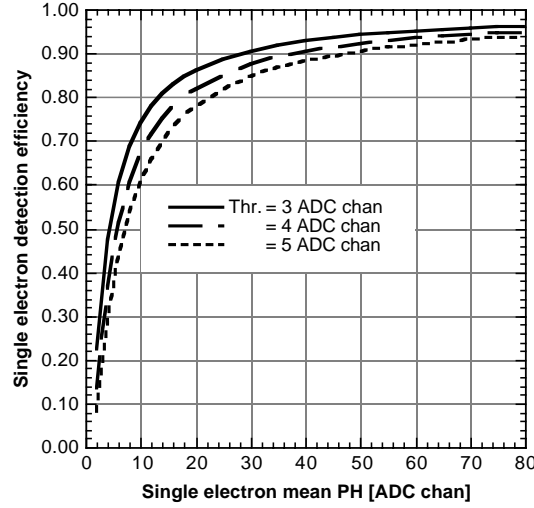


Figure 2.35: Single-electron detection efficiency as a function of the single-electron mean PH calculated at different experimental FEE thresholds.

HV scan

Figure 2.36 shows the characteristic plots derived from the previous distributions in case of an HV scan. All values are plotted versus the single-electron mean PH, A_0 , in order to normalize all results to the chamber gain whatever the experimental conditions are, such as different gas pressure, gas mixtures, gap, etc.

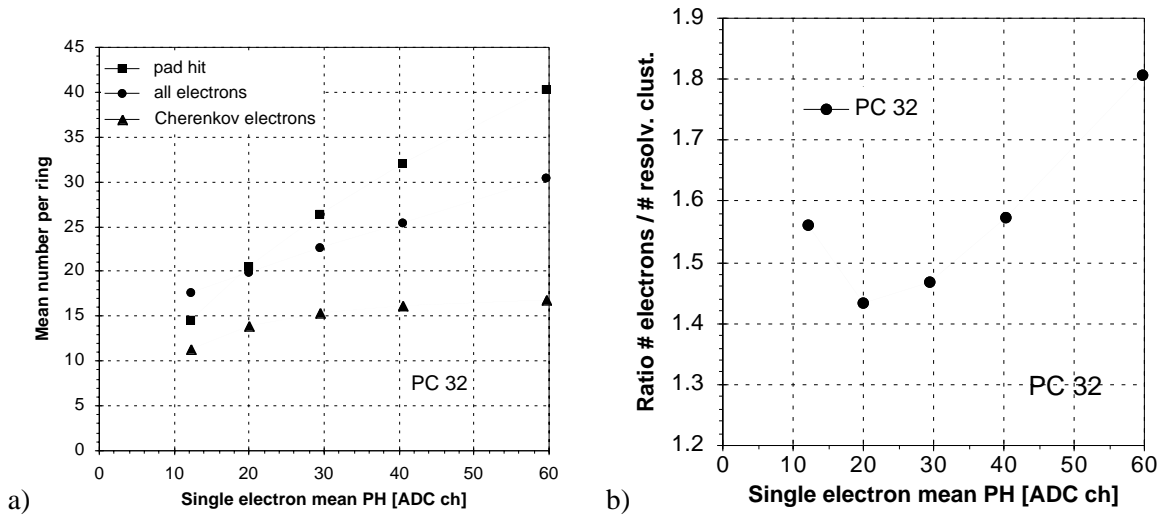


Figure 2.36: Experimental conditions: proto-2, PC32, 10 mm C_6F_{14} radiator, CH_4 , pions 350 GeV/c. a) Plots of the mean number per ring of pad hits (N_{pad}), electrons (N_{tot}) and Cherenkov electrons (N_{res}) as a function of the single-electron mean PH. b) Ratio $N_{\text{tot}}/N_{\text{res}}$, number of electrons per cluster. One ADC channel corresponds to 0.17 fC.

One can notice in Fig. 2.36a that N_{res} tends to reach a plateau of 15–16 Cherenkov photoelectrons per ring, while the total number of electrons N_{tot} increases almost linearly with the chamber gain. Such a linear dependence is expected since the feedback photons add a contribution to the total pad PH that increases linearly with the chamber gain (Eq. 2.1). The reason why N_{res} is flat (as expected at the full detection efficiency plateau, Fig. 2.35) can be given by the feedback photons emission from the primary avalanches. Since the distance of the anode to the pads is small (2 mm) compared to the pad size ($8 \times$

8 mm²), the feedback photons are emitted in a solid angle such that there is a high probability that the feedback photon is converted at the same pad as the primary one, hence overlapping the same cluster. In addition, the wider the emission angle of the feedback photon, the more probable it will be lost by reflection on the dielectric surface of the CsI photocathode (Fig. 2.3).

Such a feature has, a beneficial effect on the detection efficiency since a fraction of events is composed of two photoelectrons, but, the feedback photons contribute also to increase the pad pattern occupancy by enlarging the size of the clusters and their number. That is illustrated in Fig. 2.36a on the graph showing N_{pad} , the number of pad hits per ring, monotonically raising with the chamber gain. Finally, Fig. 2.36b shows the ratio of the total number of electrons to the number of Cherenkov resolved clusters, providing the number of photo electrons per cluster. This number is a close evaluation of the fraction of feedback photons however convoluted with a small contribution of primary Cherenkov clusters geometrically overlapped (Fig. 2.33 and Section 2.4.1). The rise of $N_{\text{tot}}/N_{\text{res}}$ observed in Fig. 2.36b at low amplification reflects that the selection by thresholding of large-sized avalanches enriches relatively the feedback photon contribution. In the next paragraph, we shall investigate the possibility of reducing $N_{\text{tot}}/N_{\text{res}}$ value, i.e. pad occupancy, by using different gas mixtures.

The influence of gas mixtures on photoelectron yield and photon feedback

It has been seen in Section 2.1.1.2 that the operation of a CsI photocathode in a gas medium at atmospheric pressure results in the loss of photoelectrons depending on the gas species and the reduced field E/p value at the surface. Therefore, we shall make a distinction between the CsI QE measured in vacuum and the photoelectron yield of a photocathode evaluated in a MWPC.

Pure CH₄ was used as basic chamber gas since it was known that noble-gas-based mixtures were decreasing the photoelectron yield. In addition, its excellent UV transparency was quite attractive. However, this good transparency makes its contribution to photon feedback non-negligible due to the three emission lines at 156, 166, 193 nm. Later results from GALICE simulation showed how important the conversion of slow neutrons in a hydrogenated gas could be. These very heavily ionizing events (MeV local deposition) might be responsible for damaging the chamber. We present a study of the influence of the gas mixtures on the photoelectron yield and associated photon feedback ratio to investigate a possible optimization.

The measurements were obtained with proto-1 equipped with PC-24 and the small C₆F₁₄ radiator adjusted at 10 mm liquid thickness. The detector was installed at H4 (pion 350 GeV/c). The C₆F₁₄ transparency was carefully monitored and found stable all along the runs.

In Fig. 2.37, N_{res} and the ratio $N_{\text{tot}}/N_{\text{res}}$ are plotted as a function of A_0 , respectively for the different gas mixtures, CH₄, CH₄-iC₄H₁₀, Ar-CH₄, Ar-iC₄H₁₀, Ar-CH₄-iC₄H₁₀. iC₄H₁₀ is known for its efficient quenching property.

Figure 2.37a shows that the photoelectron yield is maximum using pure CH₄, and decreases when increasing the iC₄H₁₀ fraction in the mixture. Compared to pure CH₄, the photoelectron yield loss is 13% by adding 10% iC₄H₁₀ and 75% in Ar-iC₄H₁₀/52-48%. A part of that loss can be attributed to worse iC₄H₁₀ UV transparency since the iC₄H₁₀ in use (98.7% purity) in our test was not purified by Oxysorb cartridges. The ‘noble-gas backscattering effect’ (see Section 2.1.1.2) can be evaluated by comparing mixtures having about the same iC₄H₁₀ fraction, that is CH₄-iC₄H₁₀/94-6 and Ar-CH₄-iC₄H₁₀/73-20-7 where the loss is 20%. Ar-CH₄ mixtures seem able to achieve the same plateau as CH₄ but it will be seen that, owing to the poor quenching of CH₄, the feedback yield is so high that the cluster resolution is degraded. In addition, microdischarges were observed at such a rate that the use of these mixtures is out of the question for stable operation.

Figure 2.37b shows the variation of the ratios $N_{\text{tot}}/N_{\text{res}}$ as a function of A_0 . As said above, $N_{\text{tot}}/N_{\text{res}}$ quantifies the fraction of photon feedback per ring in the Cherenkov fiducial zone. First, a rapid increase of the photon feedback yield is observed in Ar-CH₄ mixtures already at low gain making these mixtures useless even with 50% CH₄. For the other mixtures, the $N_{\text{tot}}/N_{\text{res}}$ curves show a minimum in the 20 to 30 ADC channel A_0 range. In fact the falling part on the left of the plots comes from the lack of effi-

ciency at low A_0 as seen in Fig. 2.37a. The lowest minimum value, 38%, is obtained with $\text{CH}_4/\text{iC}_4\text{H}_{10}$ mixtures for A_0 up to 40 ADC channels providing full single-electron detection efficiency. Although a comparable minimum is achieved in pure CH_4 , it is obtained at lower A_0 to reach 60% at A_0 equals 40 for full efficiency. Finally, the ternary and the Ar- iC_4H_{10} mixtures show a ratio remaining constant while increasing A_0 to higher values but, as seen in Fig. 2.37a, the photoelectron yield might be too low.

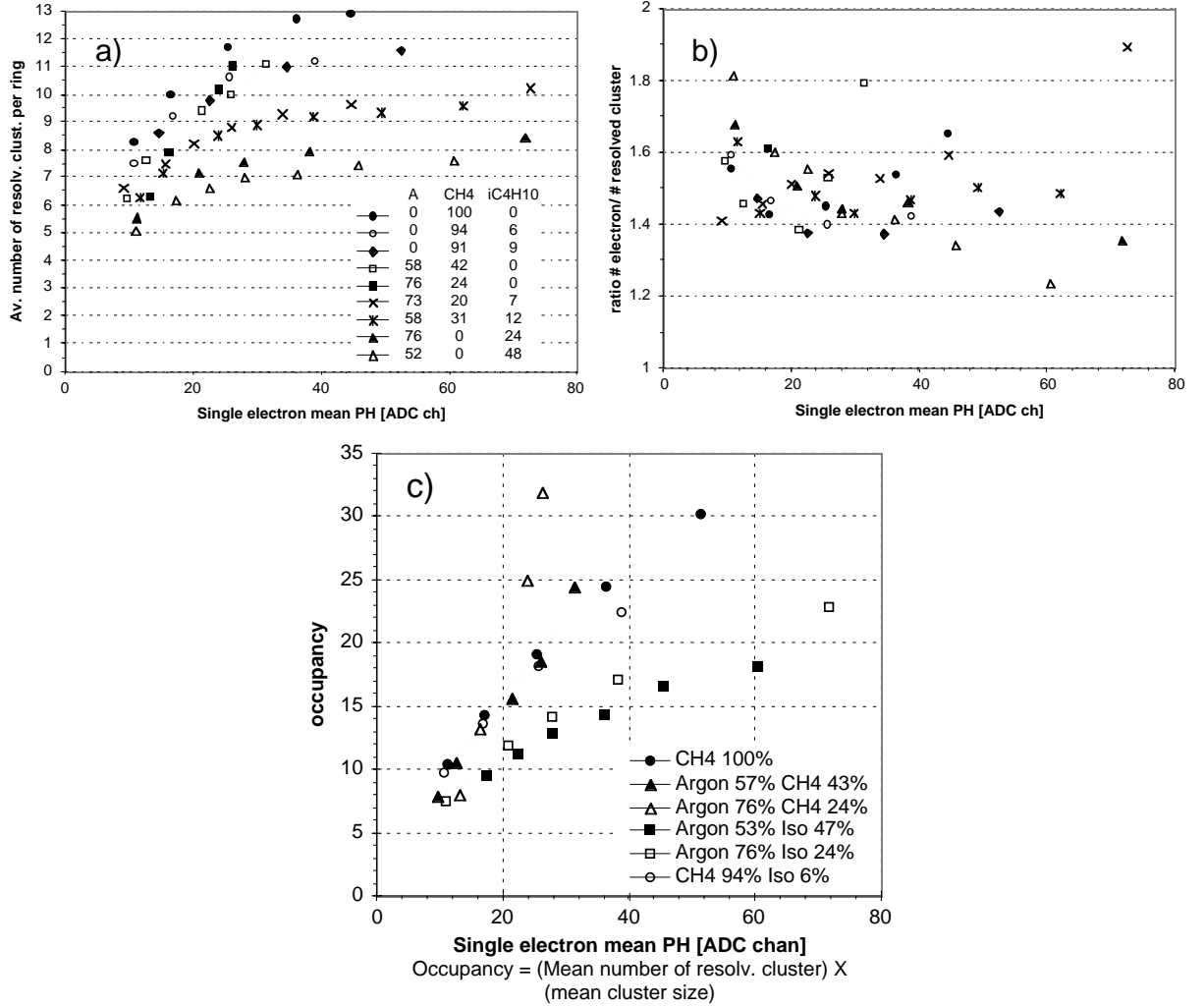


Figure 2.37: Experimental conditions: proto-1, PC24, 10 mm C_6F_{14} radiator, CH_4 , pions 350 GeV/c. Gas mixtures study. a) Plots of the mean number per ring of pad hits (N_{pad}), electrons (N_{tot}), and Cherenkov electrons (N_{res}) as a function of the single-electron mean PH. b) Ratio $N_{\text{tot}}/N_{\text{res}}$, number of electron per cluster. c) Occupancy plot for different gas mixtures. One ADC channel corresponds to 0.17 fC.

As seen in Fig. 2.37c, the different gas mixtures can also be compared by plotting an occupancy factor defined as the product N_{res} times the corresponding mean cluster size. Argon-isobutane mixtures achieve the smaller occupancy to the cost of a reduced N_{res} value.

In conclusion, the best mixture from the point of view of detector performance seems to be $\text{CH}_4\text{-iC}_4\text{H}_{10}$, although the large hydrogen content increases the neutron conversion. These questions will necessitate further investigations with alpha sources. Another candidate, half-hydrogenated, could be Ar- $\text{CH}_4\text{-iC}_4\text{H}_{10}/58\text{-}31\text{-}12$ the properties of which are compared in Table 2.3.

Table 2.3: Effect of the gas composition on the photoelectron and photon feedback yields

Gas mixture	N_{res}	$N_{\text{tot}}/N_{\text{res}}$ (%)
CH ₄	12.8	60
CH ₄ -iC ₄ H ₁₀ /91-9	11.2	45
A-CH ₄ -iC ₄ H ₁₀ /58-31-12	9.2	40

MIP detection and associated background

The background generated at the passage of the MIPs through the detector essentially originates from the feedback photons emitted by the primary avalanche and converted at the CsI PC. Other contributions are the delta electrons or interactions occurring in the MWPC gap and secondary photonic effects occurring in the proximity gap, not influenced by the field in collection gap E_{coll} (colour Fig. 1.iii), such as Cherenkov light emitted by delta electrons created in the C₆F₁₄ and the quartz window. None of the elements in use are scintillating in the operating wave length range.

In order to study the pad patterns specific to the MIPs alone in absence of Cherenkov events, the measurements presented now were taken after emptying the radiator in proto-2. The beam spot size at the chamber was of a few tens of mm² (pion, 350 GeV/c).

Figure 2.38a,b show primary cluster size and Landau PH distributions, (c) the mean primary particle cluster size as a function of the chamber voltage, relevant to further pad occupancy discussion and (d) the variation of the Landau peak versus HV, indicating a proportional regime.

The 2-D plots of colour Fig. 2.i show a substantial amount of hits outside the region where the beam particles cross the chamber. The upper curve in Fig. 2.39a shows the total number of separated clusters per event that can be split into two contributions. A small contribution comes from secondary interactions that are identified by the external pad chamber telescope. It accounts for 0.2/primary, independent of the chamber HV. Their occurrence, already low at the SPS beam energy, will be negligible at the much lower momentum range in ALICE. The larger fraction is identified as the feedback photon contribution as their PH distribution is found exponential and comparable to the one obtained at the same gain for the Cherenkov single photoelectrons, as shown in Fig. 2.40a,b. Let us remark that the small number of photoelectrons per particle, shown in Fig. 2.39b accounts only for separated clusters, remembering that the majority of them overlap the large primary cluster as discussed above.

The distances from the MIP impact to these separated clusters found outside of a zone corresponding to the MIP primary cluster size is plotted in Fig. 2.41. That distribution extends up to large values not compatible with a model where the emitting source is located at the anode wire only. One has to assume emitting sources more distant from the pad plane like parasitic Cherenkov light or reflections at the quartz surfaces. The influence on the centroid localization of the particle by the feedback clusters overlapping the primary one has been evaluated by simulation, Fig. 2.42. After correction of the intrinsic centroid error, a r.m.s. error for the coordinate along the wire is of 250 μm while the r.m.s. error in the orthogonal direction is dictated by the 4 mm wire pitch [65].

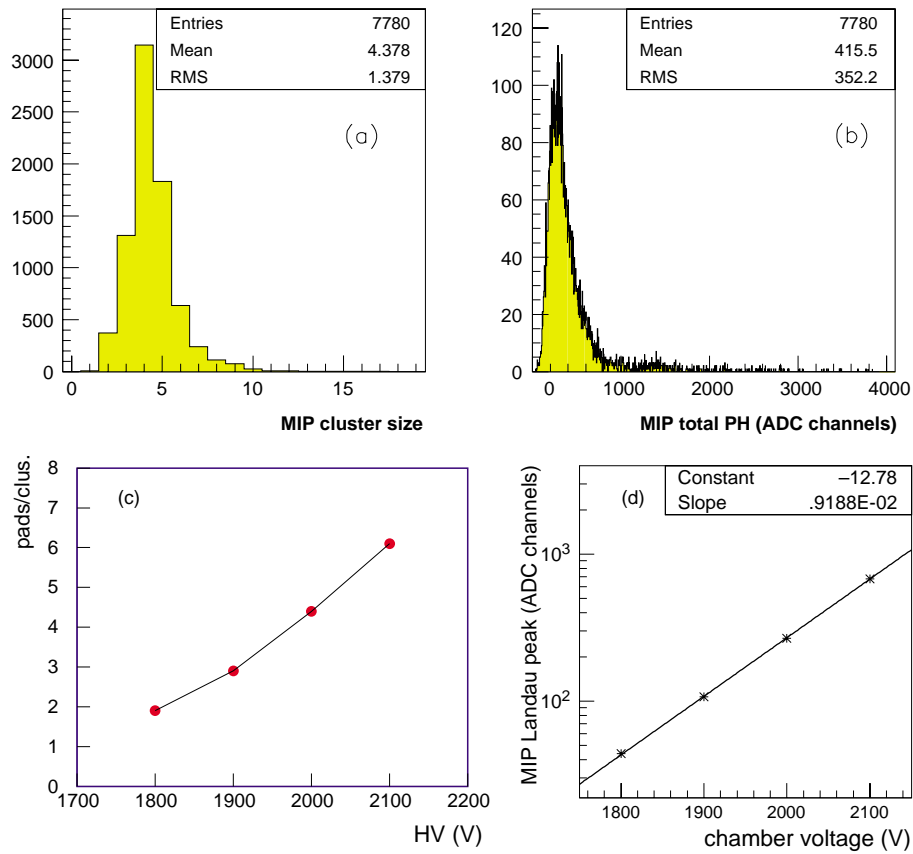


Figure 2.38: MIP studies with proto-2, PC31, CH₄, empty radiator, 350 GeV/*c* pion. a) Cluster size distribution. b) Landau PH distribution at 2000 V. c) Primary cluster size as a function of HV. d) MIP Landau peak as a function of HV.

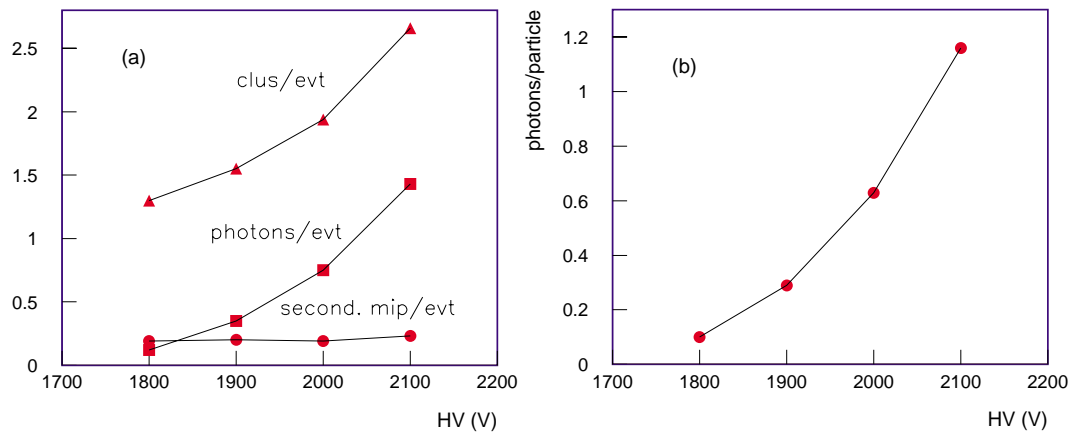


Figure 2.39: MIP studies with proto-2, PC31, CH₄, empty radiator, 350 GeV/*c* pion. Background associated to MIP primary clusters. a) number of clusters per event vs. HV. b) number of feedback electrons per particle vs. HV.

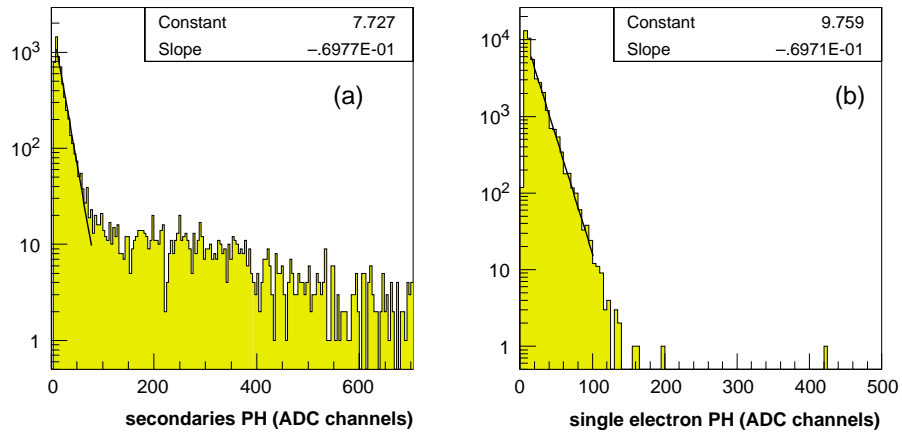


Figure 2.40: MIP studies with proto-2, PC31, 2000 V, CH₄, empty radiator, 350 GeV/c pion. a) PH spectrum of secondary clusters associated to a MIP cluster. b) For comparison, PH spectrum of single Cherenkov photoelectrons at the same voltage. One ADC channel corresponds to 0.17 fC.

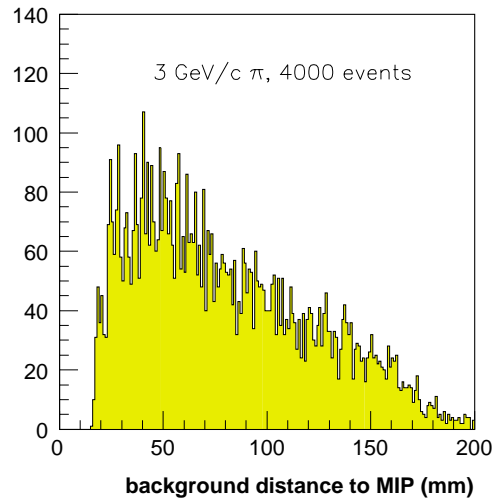


Figure 2.41: MIP studies with proto-1, PC24, 2050 V, CH₄, empty radiator, 3 GeV/c pion. Distribution of the distances of secondary clusters to the impact of their primary MIP.

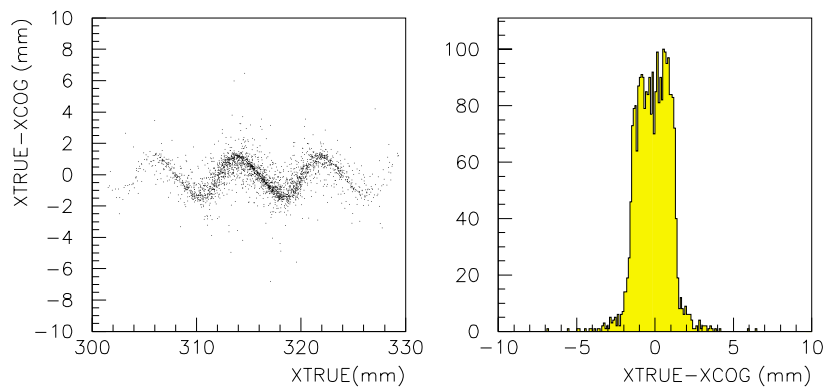


Figure 2.42: Smearing due to feedback photoelectrons of the residual distribution (compare to Fig. 2.19b).

Influence of magnetic field on the photoelectron yield

In the event of operating the CsI RICH in a magnetic field parallel to the plane of the photocathode, photoelectrons emitted nearly at rest from the CsI photocathode are submitted to the resulting force of crossed electrical and magnetic fields. Depending on the energy and emission angle of the photoelectron, the curling of the electron trajectory during the first mean free path in the gas could be such that it could be sent back to the photocathode and re-trapped. Since, to our knowledge, the distributions of the energy and emission angle of the photoelectron are not available, a direct test was set installing proto-1 inside the GOLIATH magnet at NA57 providing a field adjustable from 0 to 1.5 T parallel to the photocathode. The particles used were pions of 350 GeV/c at the H4 beam line. Proto-1 was equipped with PC-24 and a small C₆F₁₄ radiator adjusted at 10 mm liquid thickness. The chamber was flushed with CH₄. Figure 2.43 shows the variations of N_{pad} , N_{res} and N_{tot} as a function of the magnetic field measurements taken at the same gas gain: a slight decrease is observed reaching 8% at 0.9 T. Figure 2.44 shows the variations of N_{res} versus A_0 , that is decreasing the electrical field at the photocathode surface. It can be seen that the curves remain parallel at different magnetic fields down to the minimum electrical field. The E/p range under test ranges from 3.8 to 4.2 V/cm Torr⁻¹. In conclusion, the operating magnetic field at ALICE, that is 0.2 T, is not expected to affect the performance of the CsI-RICH.

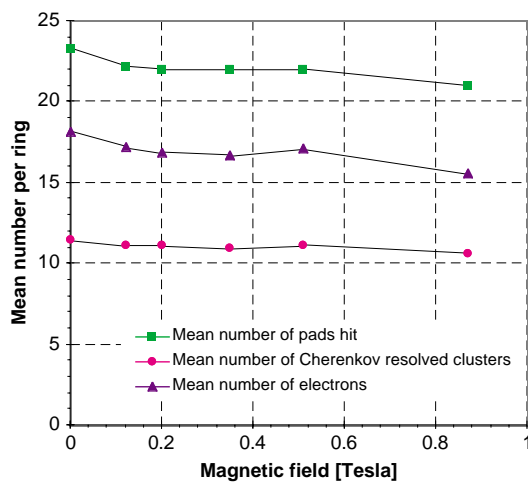


Figure 2.43: Measurements of the performance of a CsI photocathode placed parallel to a uniform magnetic field. Experimental conditions: proto-1, PC24, $HV = 2200$ V, CH₄, 10 mm C₆F₁₄ radiator, pion 350 GeV/c.

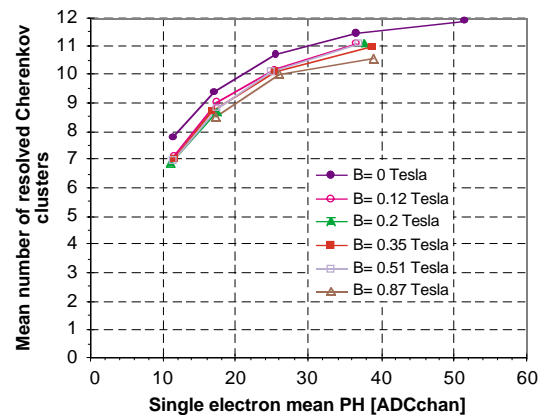


Figure 2.44: Measurement of the photoelectron yield ($N_{\text{res}}/\text{ring}$) of a CsI photocathode varying the chamber gain at different intensities of the magnetic field. Part of the drop respective to the no-field value originates from an increase of the common noise induced by the magnet operation. Experimental conditions: proto-1, PC24, CH₄, 10 mm C₆F₁₄ radiator, pion 350 GeV/c. One ADC channel corresponds to 0.17 fC.

CsI QE evaluation using Cherenkov measurements

The knowledge of the spectrum of the Cherenkov radiation, which constitutes a well-calibrated UV source, can be exploited to evaluate the CsI differential QE with two different approaches. The first one is based on the simulation of Cherenkov events aiming at the ‘tuning’ of the quantum response through the reproduction of experimental test-beam measurements; it will be described in Section 2.4. The other method allows a direct measurement of the CsI QE curve making use of the large dispersion of the refractive index of a NaF radiator (Fig. 2.45) [66].

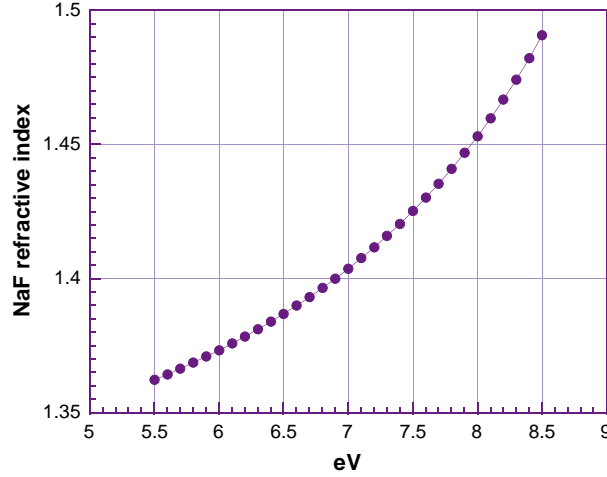


Figure 2.45: The NaF refractive index [66].

The number of photons having an energy within E , $E + dE$, incident on the photocathode, can be calculated as:

$$N_{\text{phot}}(E) = 370 L \int_E^{E+dE} \sin^2 \theta_c(E) \prod_i T_i(E) dE \quad (2.16)$$

where L is the radiator thickness, θ_c is the Cherenkov angle and T_i is the transmission of the i -th traversed medium (Fig. 2.46).

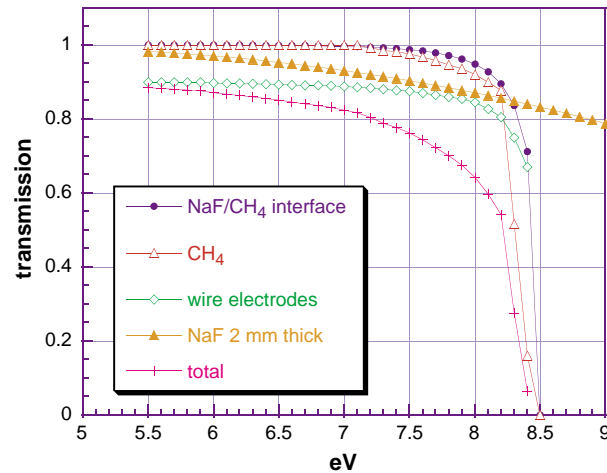


Figure 2.46: Transmission of media in the NaF RICH detector for 2 GeV/ c protons, 2 mm radiator thickness and 28 mm proximity gap.

In the case of 2 GeV/ c protons the spectral acceptance extends up to 8.5 eV, limit set by the CH₄ UV cut-off, while with 3 GeV/ c protons it is limited to 7.9 eV by total internal reflection at the NaF/CH₄ interface, according to the relation $n_{\text{max}} = \sqrt{1 + \beta^{-2}}$. In both cases the lower limit is set by the CsI photoelectric threshold.

Given the radiator thickness and the proximity gap, it is possible to determine in the detection plane circular fiducial areas such that when a photon is counted in the n -th zone its energy falls in a bin of width ΔE centred at E_n . Figure 2.47 shows the relation between the radial distance of photon impact to the centre of the ring calculated for 2 GeV/ c protons, proximity gap of 28 mm, and emission point in the middle of a 2 mm NaF radiator.

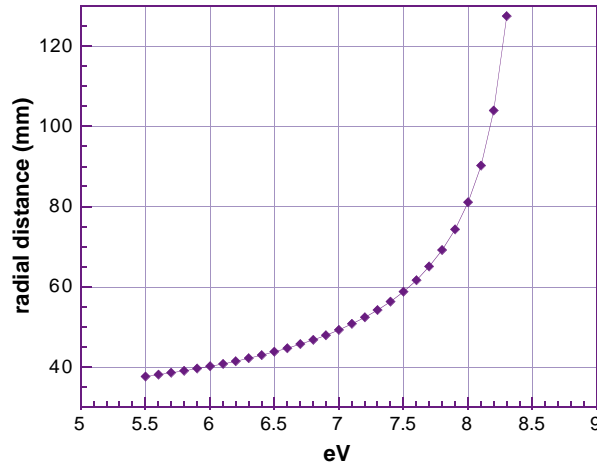


Figure 2.47: Cherenkov photons' distance from the ring centre as a function of photon energy.

Assuming that all the quantities depending on energy are constant in each energy interval of width $\Delta E = 0.1$ eV, the QE can be calculated with the approximated relation:

$$QE(E_i) = \frac{N_{\text{phel}}(E_i)}{370 L \sin^2 \theta_c(E_i) \prod_j T_j(E_i) \Delta E \epsilon_{\text{det}}}, \quad (2.17)$$

where $N_{\text{phel}}(E_i)$ is the number of photoelectrons counted in the i -th interval and ϵ_{det} is the single-electron detection efficiency. The accuracy of this method is limited by the spread of the photon emission along the particle path in the radiator. It results in a fraction of overlap between photons belonging to adjacent energy bins. To minimize this effect a radiator as thin as possible has to be used allowing narrower energy bins to be used. We present the results obtained using proto-1 equipped with PC24 and a NaF radiator 2 mm thick. Several runs have been taken in different combinations of proton beam momenta (2 and 3 GeV/ c) and proximity gaps (24.5, 28, 33, 43 and 48 mm) to investigate various spectral ranges and photocathode regions. In Fig. 2.48 are reported the average QE curve and, for comparison, the CsI QE measured at the Weizmann Institute.

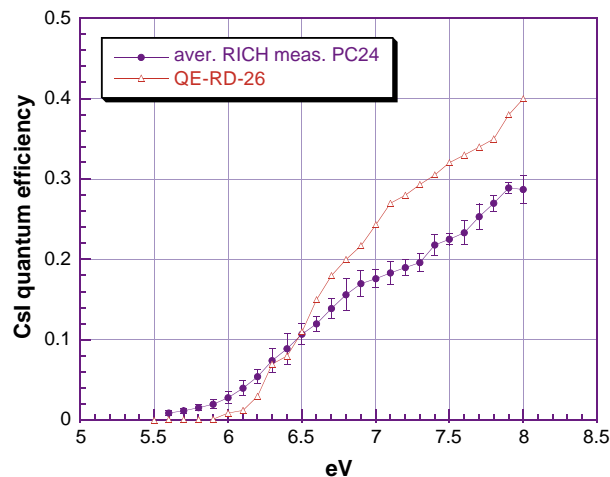


Figure 2.48: PC24 measured differential QE and the RD-26 QE obtained at the W.I.S. from photocurrent measurements on a small sample under vacuum (QE about 10% higher than the one measured in CH_4 ; Section 2.1.1.2.).

The measured differential QE is overestimated, owing to the feedback contribution to the total photon counting in each energy interval. This contribution is particularly evident in annular regions corresponding to Cherenkov photon energies below or close to the CsI photoelectric threshold (6 eV): photon counts larger than expected can only be associated with feedback photons, the energy of which is larger than that correlated to the hit fiducial zone.

After a suitable correction of the measured QE, we were able to reproduce, by means of the simulation described in Section 2.4, various sets of experimental data relative to the proto-1/PC24 equipped not only with NaF but also with C_6F_{14} radiator. This is a good cross-check of the validity of the measured QE, since the different set-up produces also a different photon spectrum.

2.3.2.3 Overall performance of the prototypes

Operation of the detector, chamber current

Despite the presence of a semi-insulating CsI layer, the commissioning of a new photocathode has never required any conditioning time: the working voltage is reached in less than one hour with a very low dark current (less than 10 nA) and very rare ‘microdischarge’ events when CH_4 or CH_4 - iC_4H_{10} mixtures are used. The noble-gas-based mixtures are more unstable under local beam irradiation at $10^4 cm^{-2}s^{-1}$ rate where voltage trips are observed.

When a breakdown occurs, it is essentially caused by an anode wire coming loose due to a weak soldering. Letting such a wire at a floating potential by removing its connection to the HV supply was found sufficient to restore the normal operation of the whole chamber.

The dark current delivered by the $1 m^2$ area of proto-2 is 1–2 nA and stable during beam operation. Local beam irradiation up to $2 \times 10^4 cm^{-2}s^{-1}$ can be sustained. Such a rate is several orders of magnitude larger than the local rate expected at ALICE (10 – 50 particles $cm^{-2}s^{-1}$). Figure 2.49 shows a sequence of the chamber current recorded by the HV slow-control system between and during the bursts.

Figure 2.50 shows the gap configuration that is traversed by the relativistic charged particles (MIP). In order that the only part of the primary ionization deposited at the passage of the MIPs be the one restricted to the 4 mm thick MWPC gap, the fraction deposited in the large proximity gap is drifted towards the collection electrode raised at a positive voltage, V_{coll} . Most of the primary ions are collected by the grounded MWPC cathode. However, if E_{mwpc} and E_{coll} are the fields in the MWPC and proximity gap, respectively, some primary electrons lying close to that transparent wired electrode may sneak from the proximity into the MWPC gap depending on the ratio E_{coll}/E_{mwpc} . That contribution has to be kept small since it unnecessarily increases the MIP avalanche size. The effect of E_{coll} was evaluated by measuring the current in the chamber irradiated by particles at a rate of 9×10^3 per burst. As shown in Fig. 2.51, the chamber current decreases and stabilizes at a constant value when V_{coll} is larger than 150 V.

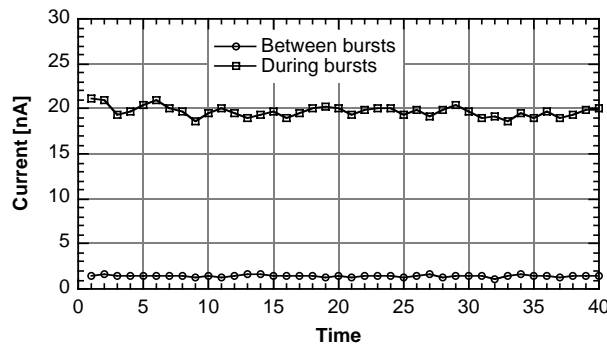


Figure 2.49: Sequence of chamber current values recorded between and during bursts of 10 000 particles. Each point is the mean of 40 bursts. $HV = 2050$ V, 10 000 particles/burst.

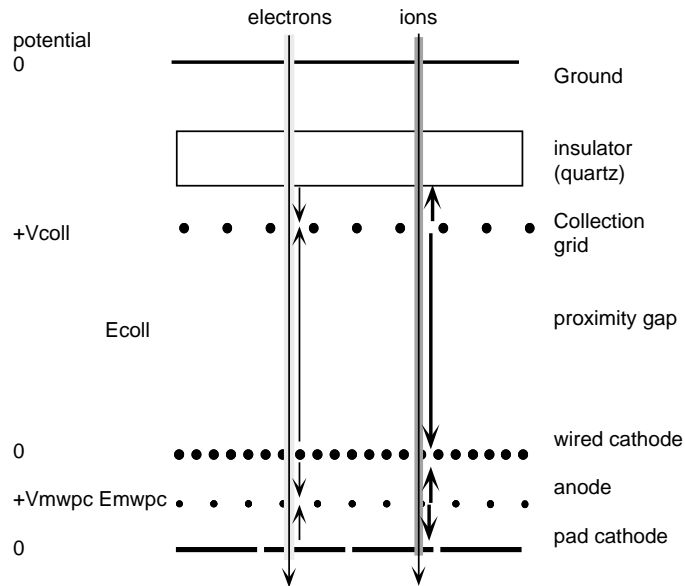


Figure 2.50: Electrical field configuration in proto-2 and primary deposition.

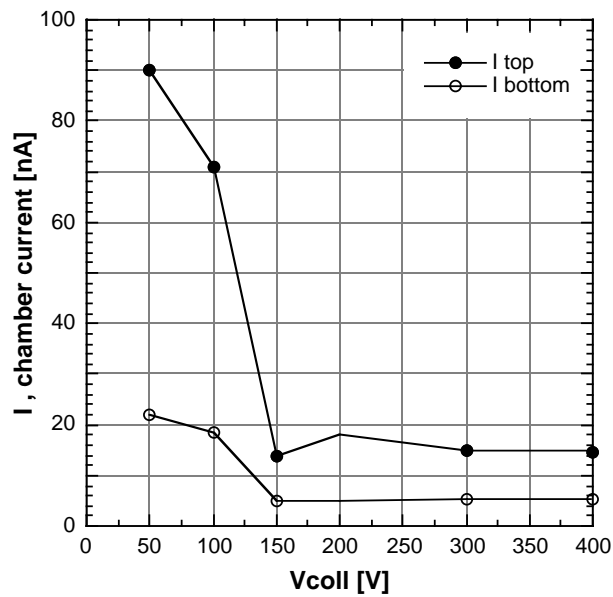


Figure 2.51: Influence of V_{coll} on the chamber current. PC32. $HV = 2050$ V, 10 000 particles/burst. I_{top} is measured in the half of the chamber crossed by the direct beam. I_{bottom} is the other half.

In Fig. 2.52, we show the variation of the single-electron mean PH, A_0 , as a function of the chamber voltage for the different gas mixtures that were tested. The working voltage ranges start at an A_0 value of 10–15 ADC channels. Remembering that the FE electronics threshold, A_{th} , is of 2 ADC channels, single-electron detection efficiencies are obtained as $\exp(-A_{\text{th}}/A_0)$.

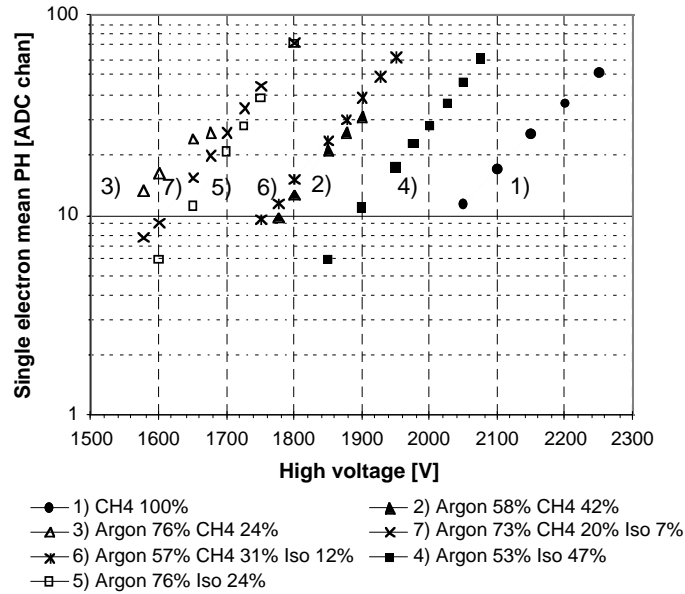


Figure 2.52: Variation of the mean single-electron PH A_0 as a function of the chamber voltage for different gas mixtures. Measurements were obtained from proto-1 using PC24, 10 mm C_6F_{14} radiator at H4/SPS, pion 350 GeV/c. One ADC channel corresponds to 0.17 fC.

Gain and photon yield uniformity

The detector is usually circulated at a flow rate of 40 l/h, that is a change of one chamber volume every 3 hours for proto-2. Given the impedance of the gas outlet pipes, the chamber is typically overpressured by 5–8 mbar. The sagittas of the pad planes induced by that overpressure were measured as a function of gas flow to be 200 μm at the centre of a pad panel at 40 l/h. To evaluate the effect of chamber gap deformation, the gain uniformity is obtained by plotting single-electron PH distributions for selected areas of the pad panel, e.g. corresponding to each quarter of a Cherenkov ring. As seen in Fig. 2.53, a coarse scan can be achieved by taking runs at different positions of the ring centre.

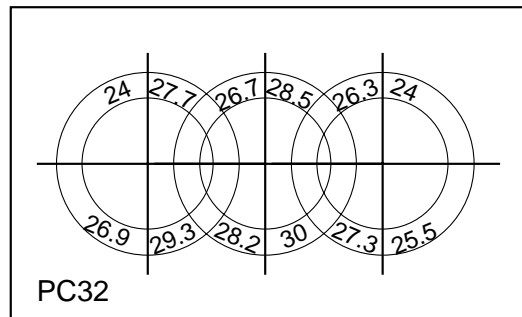


Figure 2.53: Evaluation of the uniformity of the chamber gain across PC32 in proto-2. The numbers correspond to the mean PH spectrum measured in 90° sectors of the Cherenkov fiducial zones. $HV = 2050$ V.

In order to evaluate the uniformity of the photoelectron yield of a CsI photocathode, pad patterns of rings are overlapped to create a 2-dimensional hit density plot that allows in turn to plot the hit density per unit angle versus azimuthal angle of the ring. Such a plot is shown in Fig. 2.54, indicating a uniform response all around the ring. Since the ring radius is large, repeating the operation at different locations over the pad panel allows almost the whole photocathode area to be scanned. The variation of the azimuthal density was never found to be larger than 10%, demonstrating a satisfactory uniformity of the response of the PC over its whole area.

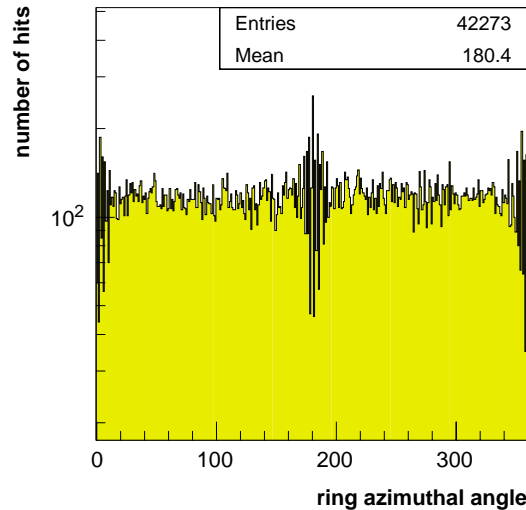


Figure 2.54: Azimuthal distribution of number of hits by 1° bin along the Cherenkov fiducial zone. (3000 events, PC32, 2050 V).

Optimization, yield and stability of PCs

In this section, an outline of the RD phase is given to review the steps achieved in the optimization of the detector towards the assembly of a final prototype of a HMPID module.

During the period 1993 to 1997, 32 CsI photocathodes were produced and evaluated using test beams. They are referred to as PC1 to PC32 in Fig. 2.55. The choice of a parameter convenient to compare their performance is not straightforward since a variable like the photoelectron yield depends on specific experimental conditions like transparencies, efficiencies, etc that might change from run to run. For that purpose, we have taken the QE value at 170 nm, referred as QE(170).

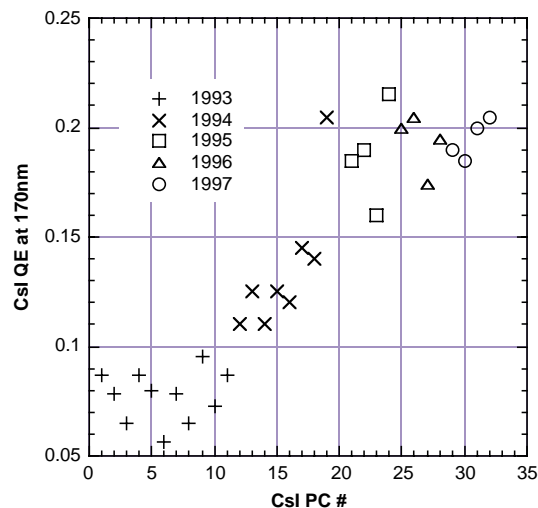


Figure 2.55: CsI QE history. Overview of the QE measured at 170 nm of all the CsI photocathodes produced during the R&D phase.

The following actions, described in chronological sequence, were taken and resulted in an improvement of either the photoelectron yield or the QE(170) performance.

a) At the beginning of our R&D work, CsI layers were deposited on G10/Cu/Au substrates at room temperature (PC1 to PC10), showing low QE and bad quality coatings (Section 2.1.1.5). An improvement was observed (PC12 to PC18) when the post treatment was applied (Section 2.1.1.3).

b) During 1994, PC19 was the first photocathode where the pad PCBs with a Ni/Au layer and polishing were implemented, with the post-treatment applied after CsI evaporation. As seen in Fig. 2.55, a clear improvement of QE(170) was achieved in comparison to the previous PCs made with standard PCBs.

c) Also, during the periods when the PCs were not mounted on the detector for test, they were protected by a tight lid and stored in a setup providing a continuous argon circulation of 15 l/h. Progressively, the mounting on detector was done more carefully in a Jacobex glove box under argon.

d) In 1995, the optical transparency of the second MWPC cathode was improved by replacing a stainless steel mesh (500 $\mu\text{m}/\text{square}$) providing a good field hermeticity in the gap by a cathode made of 100 μm diameter wires spaced by 2mm. A gain of 20% in the transparency, hence in the photon yield, was achieved. This gain is obtained because of the large angles, $\sim 60^\circ$, under which the photons cross the wire cathode. The gain uniformity and the protection against charges deposited in the proximity gap were still found satisfactory by using the wired cathode as seen in Fig. 2.51.

e) After PC19, a series of photocathodes were produced to investigate whether the adopted PCB technology and CsI processing were convenient to achieve reproducible results.

f) As seen in Fig. 2.55, the mean performance was kept at a satisfactory mean level over the next 10 PCs with the exception of PC23. Also, the check of PC22 after a 4 months storage period showed a significantly degraded performance. An examination of the PC surface indicated the presence of whitish spots possibly attributed to an exposure to moisture. Both, the transfer procedure from the evaporation vessel to the detector and the tightness of the PCB (through holes) were put under question.

g) An improved technology was tested to guarantee the tightness of the pad PCBs (discussed in Section 3.1.1.1) that was applied to the four large PCs installed on proto-2 (PC29 to PC32). Also, given the size of proto-2, a removable glove box was built to be adapted directly to the back of the detector, allowing for the transfer of each PC from its protective box to the detector without any contact with air. During these manipulation the fractions of oxygen and moisture were kept below 400 ppm.

This first step allowed to demonstrate that the handling, mounting of PCs on a HMPID module of final sizes were achievable under safe conditions and with a simple tooling. The contamination levels could and should still be decreased.

h) Since PC22 was damaged, that was the opportunity to check whether a second evaporation on the same substrate was feasible after removing the bad CsI film. The removal was done by using pure ethanol and a very soft tissue. The panel was outgassed for a week at 60° under argon before the second evaporation. The resulting new QE(170), indicated as PC27 in Fig. 2.55, was found comparable to the first one. That unique test has to be reproduced since, in case of confirmation, the renewing of aged PCs could be done by a second CsI evaporation, avoiding the non negligible expense of the construction of new pad panels. The new equipment described in Section 3.1.5.2 will be used to pursue this study more conveniently than producing and testing expensive pad panels at the beam.

Stability of the CsI photocathode

Following a first performance evaluation just after production, several photocathodes were periodically re-evaluated at the test beam in order to control their stability versus chemical contaminations as moisture, oxygen. Figure 2.56a shows the evolution of PC19 and PC24, two of our oldest PCs. Even though these PCs were removed and remounted about 10 times from proto-1, under non optimal conditions, long plateaus are observed corresponding to less than 5% QE drop over three years. As discussed in the previous paragraph, the production and the handling of the last PCs, 29 to 32, equipping proto-2 were performed with more care and controls. They show, in Fig. 2.56b, an excellent stability over their first year of operation. These checks will be pursued as well as dedicated tests aiming to quantify the QE loss as a function of the contamination rates using the ASSET system (see Section 2.1.1.6).

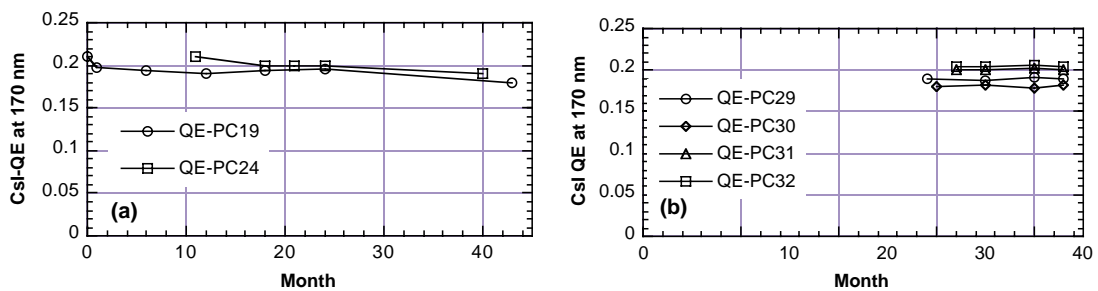


Figure 2.56: QE stability plots. Evolution with time of the QE of several photocathodes.

2.3.2.4 Proto-2: results obtained with single-particle events

Proto-2 was assembled in 1996 and the first large photocathode, PC26, tested at T11 in December 1996. The four final PCs (PC29 to PC32) were processed and tested with small radiators at T11 from June to October 1997. A first test of the detector fully equipped with four PCs and one full-size-radiator tray was performed at the SPS in November 1997. Finally, two SPS test periods were scheduled in April and July 1998, the second one with the complete radiator composed of two trays. Measurements relative to PCs evaluation are reported here while those taken with beam interacting on target are found in Section 2.3.2.6. Figure 2.57 indicates the position of the four photocathodes and of the radiator tray for the test period when only one tray was mounted.

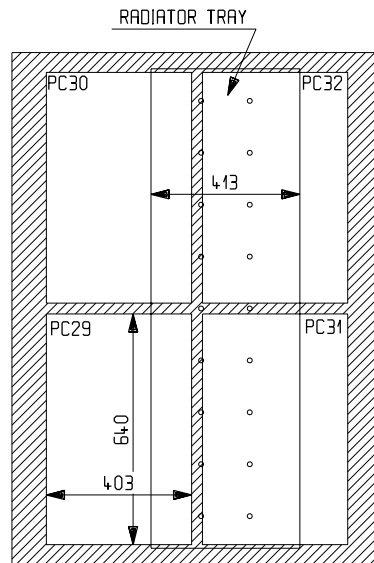


Figure 2.57: Schematic layout of proto-2 showing the position of the radiator tray relative to the four CsI pad panels (PC29 to PC32) when using a single tray at the SPS test runs in November 1997 and April 1998. For the July 1998 runs, the layout with two radiator trays is seen in Fig. 2.26.

Single-particle runs were taken to scan at three beam positions the four PCs at different particle incident angles: $0, \pm 2.5, \pm 5, \pm 7.5^\circ$. In addition to the evaluation of the detector, these runs are used as databases to generate by software multiparticle patterns of known density by randomly overlapping single events that are fully characterized. Their analysis is found in Chapter 4.

- a) The total time of exposure to the beam was about 30 days. The irradiation rate was typically 5 kHz on a beam spot of 1 cm² corresponding to a maximum current of 30 nA/cm² at maximum gain. During monitoring, neither microdischarges nor HV trips were observed, indicating a quite stable operation. Such a current density is much higher than the one expected at ALICE. CH₄ was mainly used as amplification gas at a flow of 30 l/h. The contamination level was kept at less than 10 ppm for oxygen and moisture. The performance of the C₆F₁₄ radiator system is reported in Section 3.1.3.
- b) In Fig. 2.58, the measurements of N_{res} and N_{pad} obtained with PC32 over four test periods from its production in August 1997 until July 1998 overlap, demonstrating an excellent stability of the performance for about one year. Three photocathode removal operations were done during this period using the large glove box set-up described in Section 3.2.3.3.

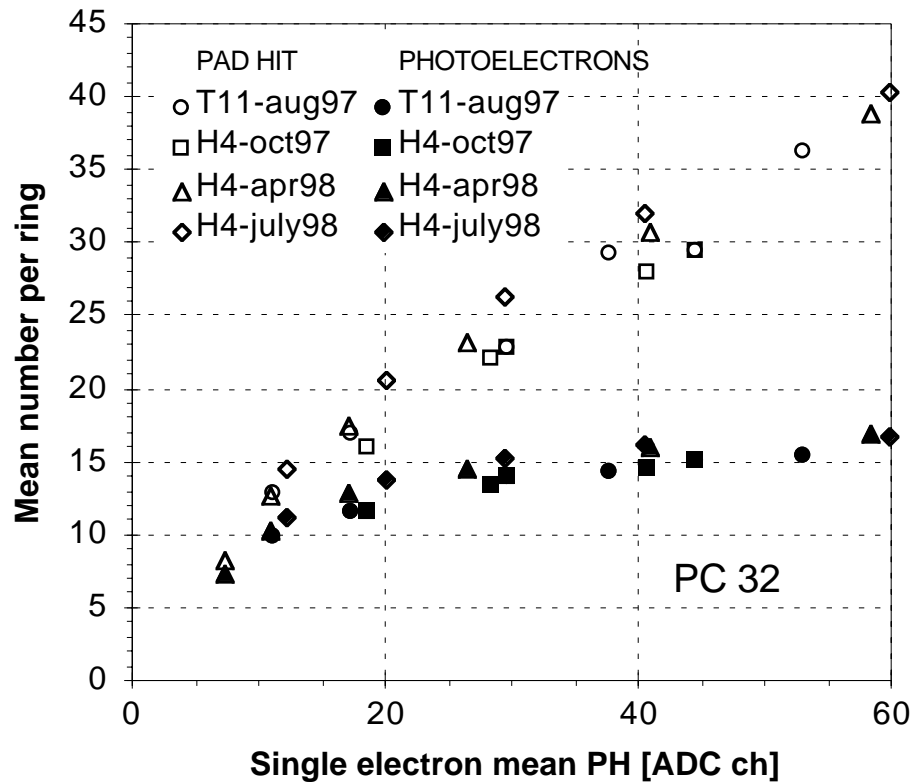


Figure 2.58: Stability of the performance of PC32. Four measurements, obtained over one year's duration, are superimposed. Operating conditions: CH₄, 10 mm C₆F₁₄, pion 350 GeV/c. One ADC channel corresponds to 0.17 fC. Mean N_{res} and N_{pad} per ring as a function of the single-electron mean PH.

- c) In Fig. 2.59a, the gain variation A_0 is represented versus the chamber voltage obtained with the beam centred at the middle of each photocathode. While the same gain curves are measured in the quadrants of the chamber corresponding to PC30 and PC32, the curves are shifted by +30 V for PC31 and -30 V for PC29, respectively to PC30, PC32. At an operational voltage of 2050 V, that shift corresponds to a 20% variation of the chamber gain A_0 . Given the relative situations of PC29 and PC31 on the detector (Fig. 2.57), the gap variation cannot be attributed to an overall deformation of the main frame due to the overpressure but to gap differences of each pad panel resulting in the adjustment procedure (frame machining) described in Section 3.1.1.2. Such a gain difference corresponds to a variation of 120 μm of the nominal 2 mm gap value. The incidence on the clustering is shown below.

- d) In Fig. 2.59b, the photoelectron yields, N_{res} , and the number of pads hit per ring of the four photocathodes are compared. A mean value of $N_{\text{res}} = 14.9 \pm 1.5$ is obtained at $A_0 = 40$ ADC channels. This spread is not correlated to the different gains reported in Fig. 2.59a: PC31 and PC32, achieving the best yields, are located in gaps of low gain. This reflects, in fact, a spread in the QE value, as seen in the plots (c) and (d) of the cluster size and ratio $N_{\text{tot}}/N_{\text{res}}$ correlating PCs of low QE to PCs of low photon feedback. This spread is actually found acceptable in the context of our pattern recognition efficiency. Finally, proto-2 was operated in July 1998 with CH_4 - $i\text{C}_4\text{H}_{10}$ mixtures. When adding isobutane, the photoelectron yields drops down by 10–20% but associated to a significant decrease of the feedback photon yield at high gain, as shown in Fig. 2.60.

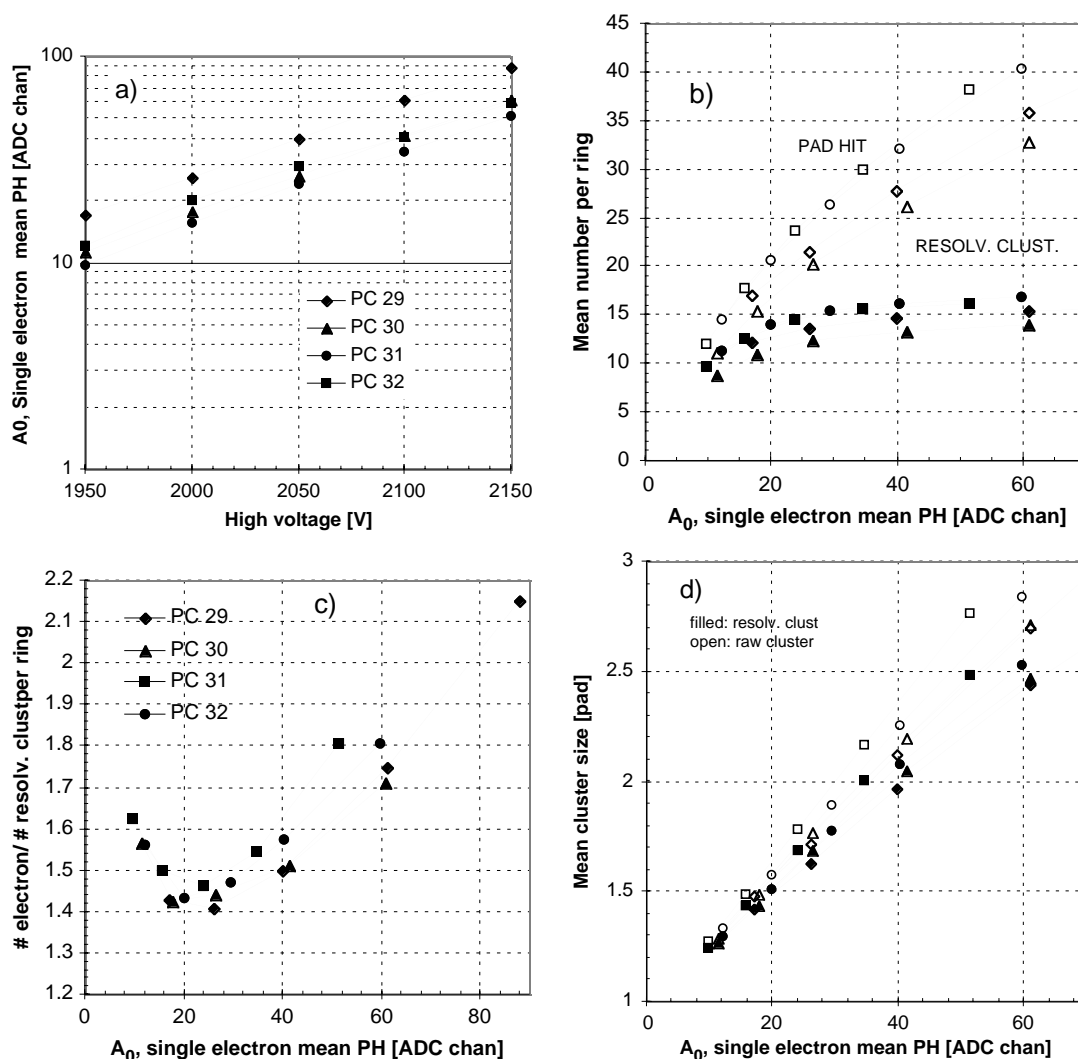


Figure 2.59: Compared performance of the four photocathodes mounted on proto-2. Operating conditions: CH_4 , 10 mm C_6F_{14} , pion 350 GeV/c. One ADC channel corresponds to 0.17 fC. a) Mean single-electron PH (or chamber gain) as a function of high voltage measured at the centre of each of the four PCs. As a function of the single-electron mean PH: b) Mean N_{res} and N_{pad} per ring. c) Ratio $N_{\text{tot}}/N_{\text{res}}$ (feedback photon fraction). d) Mean resolved cluster size.

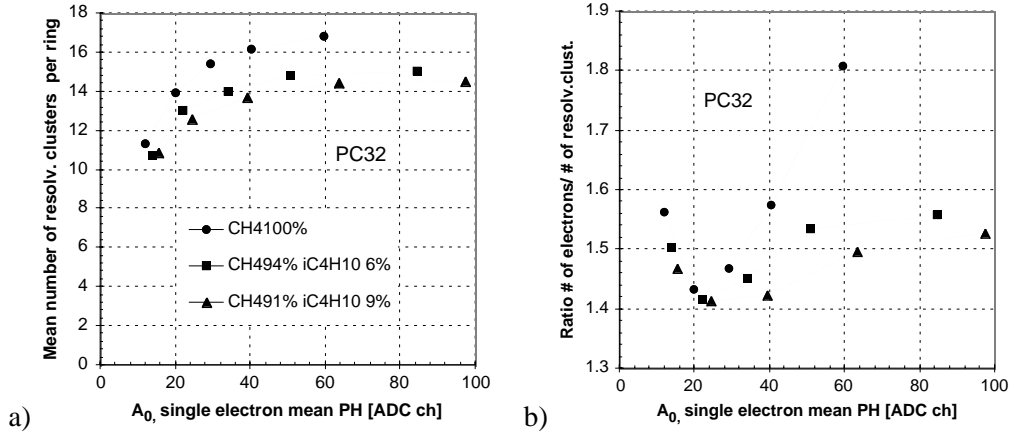


Figure 2.60: Performance comparison using different gas mixtures in proto-2. Operating conditions: PC32, 10 mm C₆F₁₄, pion 350 GeV/c. One ADC channel corresponds to 0.17 fC. As a function of the single-electron mean PH: a) Mean N_{res} per ring. b) Ratio $N_{\text{tot}}/N_{\text{res}}$ (feedback photon fraction).

2.3.2.5 Study of the angular resolution with single-particle events

The angular resolution is maybe the most important feature of a RICH detector since it is strongly correlated to the particle identification capabilities. We have carried out an investigation of all the aspects influencing the spread of the reconstructed angle distribution, based on a combined analysis of beam test and Monte Carlo events with the support of an analytical estimation of each contribution.

The Cherenkov angle is affected by the following errors:

- (1) The *chromatic error*, related to variation of the radiator refractive index n with the photon energy E . It is determined by the dispersion dn/dE of the radiator medium index and by the spread of the overall detector response over the effective photon energy range, between the CsI photoelectric threshold and the C₆F₁₄ cut-off (Fig. 2.24d).
- (2) The *geometric error*, related to the spread of the emission point along the particle path in the Cherenkov radiator. It depends on the ratio RW/GAP between the radiator thickness, RW , and the proximity gap width, GAP ; it can be minimized by increasing GAP and reducing RW , provided the number of photoelectrons per ring is sufficient for pattern recognition (Chapter 4).
- (3) The *localization error*, related to the precision with which the photon and particle impact coordinates can be measured. It is determined by the detector characteristics (pad size, sense wire pitch) and by the photon feedback.
- (4) The track *incidence angle error*, related to the particle angle θ_p and to the precision of the tracking devices. In the following, the θ_p error, assumed to be of the order of 2 mrad at the considered incidence angles, will not be quoted in tables and plots but simply included in the calculation of the total angular resolution.

While the chromatic and geometric error are intrinsic, respectively, to the radiator properties and to the proximity focusing technique, the last two are of experimental nature.

The angle reconstruction procedure defines, between the Cherenkov angle θ_c and each of the described variables, a relation $\theta_c = \theta_c(E, RW, R, \theta_p)$ from which the angular resolution, particular to the adopted algorithm, can be analytically estimated as:

$$\sigma_{\theta_c} = \left[\sum_{i=1}^4 \left(\frac{\partial \theta_c}{\partial v_i} \sigma_{v_i} \right)^2 \right]^{1/2}, \quad (2.18)$$

where the variables v_i are: E, RW, R, θ_p and σ_{v_i} are the respective r.m.s. errors.

Angle reconstruction and analytical treatment

Three methods have been used for the Cherenkov angle reconstruction, in real and simulated events. The first one, called β -method, provides the intrinsic angular resolution, being based on the knowledge of the particle β which eliminates the analytical dependence on n . The second one, the $loop$ -method, is based on the search of the best angle through an iteration routine [67]. Figure 2.34c shows the single-photon experimental distributions of ring radius; the corresponding reconstructed Cherenkov angle distributions, either single-photon or ring averaged (with $\sigma_{\theta_c}^{\text{ring}} = \sigma_{\theta_c}^{\text{single}} / \sqrt{N_{\text{res.cluster}}}$), obtained by means of those two procedures, are shown in Fig. 2.61. Both will be described briefly here and the relative numerical results from the analytical calculation of single contributions to angular resolution will be presented. An extensive discussion about the analytical treatment can be found in Ref. [68].

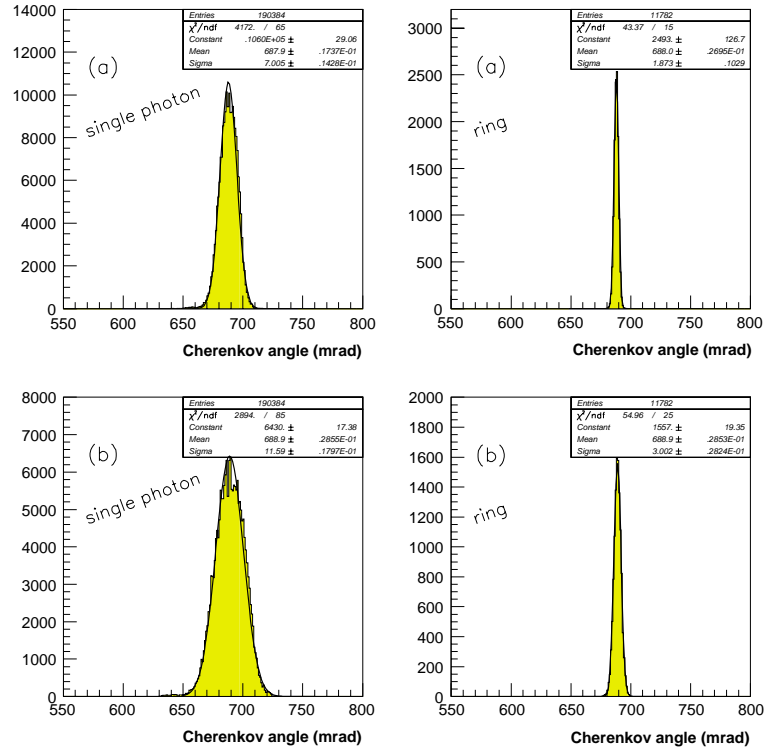


Figure 2.61: Single-photon and ring-averaged, Cherenkov angle distributions, from a) the β and b) the $loop$ -methods; SPS beam test (350 GeV/c π), PC32, chamber gain $A_0 \sim 40$ ADC channels.

The third reconstruction algorithm, which produces the same results as the $loop$ -method, is based on a photon geometrical backtracing; it will be presented in Chapter 4 with an application to multi-particles events.

Since the photon *emission point* in the radiator, X_{ep} and the photon energy are unknown, in all methods, the angle reconstruction is achieved by fixing them at the most probable values. In particular, X_{ep} is about 5.2 mm for perpendicular tracks in a 10 mm radiator (photons generated in the first radiator half have larger probability of being absorbed due to the longer path in the C_6F_{14}), while the average energy E_{av} is 6.85 eV over the detector response (Fig. 2.24d).

i) The β -method. Figure 2.62 illustrates the geometry for the angle reconstruction with perpendicular incidence particles; in the case of oblique tracks an image correction through a detector rotation is needed. The measured ring radius R can be expressed as:

$$R = \Delta R_{\text{rad}} + \Delta R_{\text{qz}} + R_0, \quad (2.19)$$

where $\Delta R_{\text{rad}} = (RW - X_{ep}) \cdot \tan \theta_c(E_{av})$ and $\Delta R_{\text{qz}} = QW \tan \theta_{qz}(E_{av})$ are constant terms and $R_0 = GAP \cdot \tan \theta_0$. θ_0 can be simply expressed as a function of θ_c by means of Snell's law; then, using

the Cherenkov relation $\cos \theta_c = (n\beta)^{-1}$, with simple calculations, one can reconstruct the Cherenkov angle as:

$$\theta_c = \arccos\left(\frac{\beta^2}{1 + (GAP/R_0)^2} + 1\right)^{-1/2}, \quad (2.20)$$

where GAP and particle β are known and R_0 is deduced from the measured radius through Eq. 2.19.

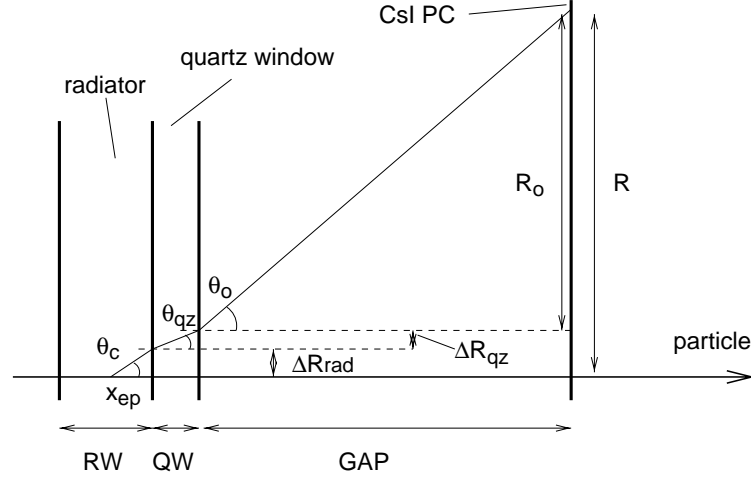


Figure 2.62: Cherenkov photon optical path through the detector and geometry for the β -method angle reconstruction.

ii) The *loop-method*. In the first step, the angle ϕ_c , defined by the plane containing the particle trajectory and the photon impact, is calculated and, assuming $\theta_c = \theta_c(E_{av})$ and $\beta = 1$, photon tracking is executed starting from X_{ep} through the media up to the CsI PC, producing an impact point at a distance Δs from the measured point of coordinates (x_c, y_c) . Then a new tracking is started after having increased θ_c and ϕ_c by $(d\theta_c/ds)\Delta s$ and $(d\phi_c/ds)\Delta s$ respectively, with the derivatives evaluated with a 0.5 mrad variation of each angle. The condition which stops the iteration is $\Delta s \leq 0.1$ mm.

A straightforward vector ray trace with refraction at all surfaces in the detector media gives the following equation for the photon coordinates [69]:

$$x_c = Ra_x, \quad (2.21)$$

$$y_c = Ra_y, \quad (2.22)$$

where

$$R = \frac{L}{a_z} + \frac{QW}{\sqrt{a_z^2 + (n_q/n)^2 - 1}} + \frac{GAP}{\sqrt{a_z^2 + (1/n)^2 - 1}} \quad (2.23)$$

and a_x, a_y, a_z are the photon direction cosines in the detector reference system. In the limit case $RW, QW \rightarrow 0$, an explicit solution giving θ_c as a function of the measured quantities (x_c, y_c, θ_p) is obtained:

$$\cos \theta_c = \cos \phi_p \sin \theta_p a_x + \sin \phi_p \sin \theta_p a_y + \cos \theta_p a_z, \quad (2.24)$$

with ϕ_p particle track azimuthal angle, $a_x = x_c/nr$, $a_y = y_c/nr$, $a_z = \sqrt{1 - (x_c^2 + y_c^2)/(n^2 r^2)}$ and $r^2 = x_c^2 + y_c^2 + GAP^2$.

Evaluation of the r.m.s. errors

After having obtained the partial derivatives $(\partial\theta_c/\partial v_i)$ from the relations Eq. 2.20 and Eq. 2.24, the final step of the analytical treatment is the evaluation of the r.m.s. errors σ_{v_i} which are strictly related to the detector response.

The estimation of the chromatic r.m.s. error, $\sigma_E = (dn/dE)\sigma_E^{\text{det}}$, is important in reproducing, with either Monte Carlo simulation or analytical treatment, the measured angular resolution. As explained in Section 2.1.3.1, the assumed value for dn/dE is 0.0172 eV^{-1} . σ_E^{det} represents the standard deviation of the detected Cherenkov photon spectrum, resulting from the convolution of all media UV-transmission with the CsI QE (Fig. 2.24d). The shape of such a distribution suggests a triangular response of the detector to UV photons and, therefore, σ_E^{det} can be approximated by $\Delta E/\sqrt{24} = 1.8/\sqrt{24} \text{ eV}$. With such values we obtain: $\sigma_E = 6.33 \times 10^{-4}$.

For the geometric r.m.s. error σ_L the calculation is straightforward:

$$\sigma_L = RW/(\sqrt{12} \cos \theta_p) = 2.89 \text{ mm}/\cos \theta_p.$$

The total localization r.m.s. error σ_R includes the indeterminacy of both particle and photon x, y coordinates. The values used to calculate σ_R are: $\sigma_x = 2 \text{ mm}$ and $\sigma_y = 2.5 \text{ mm}$, both for photons and particles. It is evident that both σ_x and $\sigma_y \rightarrow (x \text{ or } y \text{ pad-size})/\sqrt{12}$ (with $8 \times 8 \text{ mm}$ pad size). Besides the error introduced by the finite sampling of the charge related to the detector pad segmentation (Figs. 2.19b, Fig. 2.42) further contributions come, for photons, from the large fraction of single pad clusters for which no centroid evaluation is possible, while, for particles, they come from the photon feedback associated to the larger total charge released.

In Table 2.4 are reported the results of analytical estimations of each contribution in the two methods; for comparison, the same errors have been evaluated with the simulation program, described in Section 2.4.1, disabling suitable switches in the code in order to get only the contribution from a particular quantity. The presented values refer to $\beta = 1$ and proto-2 geometry, namely $RW = 10 \text{ mm}$, $QW = 5 \text{ mm}$, $GAP = 103 \text{ mm}$.

Table 2.4: Single-photon Cherenkov angle errors from analytical treatment and simulation

Error	Calculation		Simulation	
	β -method (mrad)	loop-method (mrad)	β -method (mrad)	loop-method (mrad)
chromatic	5.7	9.4	5.9	9.7
geometric	2.5	4.1	2.6	4.2
localization	3.1	4.8	3.1	5

Optimization of the angular resolution in beam tests

The analytical treatment and the simulation have been developed aiming at a better understanding of experimental data and, hence, at the optimization of the detector response in terms of angular resolution. Several studies have been carried out in beam tests, to analyse the angular resolution dependence on:

- the Cherenkov ring radius (proximity gap dependent);
- the chamber gain (high voltage and gas mixture dependent);
- the radiator thickness;
- the particle incidence angle θ_p .

In Table 2.5 are reported the single errors $((\partial\theta_c/\partial v_i)\sigma_{v_i})$ and the angular resolution (σ_{θ_c}) , from analytical calculation and simulation, for the β -method, at several ring radii. In Table 2.6 the same quantities, evaluated with the *loop method*, are shown. It should be borne in mind that the simulation σ_{θ_c} values come

from the reproduction of test-beam runs, thus including effects related to the detector operating conditions peculiar to each run, while the calculated values refer to a constant configuration.

In the following all the presented results are relative to the β -method since the β value is experimentally known with accuracy.

Figure 2.63 shows the single-photon and ring angular resolution, from measurements and simulation, as a function of the ring radius, confirming the good agreement among measurements, simulation, and analytical treatment. Besides, the results quoted in Table 2.5 and Table 2.6 point out the dominance of the chromatic error over the other contributions, at ring radii < 120 mm; therefore a reduction of the localization error, which could be obtained with a finer detector segmentation, would produce a very small improvement of the angular resolution, not compensating the cost for the increased number of electronic channels.

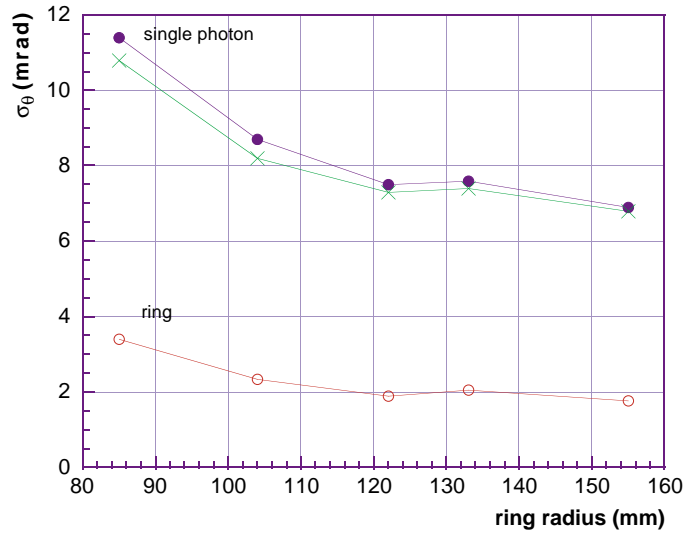


Figure 2.63: Angular resolution as a function of ring radius at $A_0 \sim 40$ ADC channels; circles: measurements; crosses: simulation. Ring radius 85 and 104 mm: data from PS beam-test (3 GeV/c p and π , $GAP = 70$ mm), PC24; ring radius 133 mm: data from PS beam-test (3 GeV/c π , $GAP = 90$ mm), PC32; ring radius 122 and 155 mm: data from SPS beam-test (350 GeV/c π , $GAP = 80$ and 103 mm), PC32.

Table 2.5: Single-photon extracted Cherenkov angle errors from analytical treatment and simulation, in the β -method, at several ring radii

ring radius (mm)	Calculation				Simulation
	chromatic (mrad)	geometric (mrad)	localization (mrad)	σ_{θ_c} (mrad)	σ_{θ_c} (mrad)
85	5.76	4.83	5.95	9.7	10.8
104	5.73	3.78	4.66	8.4	8.2
122	5.71	3.26	4.01	7.8	7.3
133	5.7	2.9	3.6	7.43	7.4
155	5.69	2.53	3.12	7.1	6.8

Table 2.6: Single-photon extracted Cherenkov angle errors from analytical treatment and simulation, in the *loop method*, at several ring radii

ring (mm)	Calculation				Simulation
	chromatic (mrad)	geometric (mrad)	localization (mrad)	σ_{θ_c} (mrad)	σ_{θ_c} (mrad)
85	9.4	7.9	9.1	15.9	15.6
104	9.4	6.2	7.1	13.8	13.3
122	9.4	5.4	6.1	12.8	12.2
133	9.4	4.8	5.4	12.2	12
155	9.4	4.2	4.8	11.6	11.1

In Fig. 2.64 are reported the single-photon and ring angular resolution, from measurements and simulation, as a function of the chamber gain represented by the single-electron average pulse height A_0 , in two gas mixtures. The stability of σ_{θ_c} with the increase of A_0 , at the considered ring radius, could be the result of two opposite effects: the larger feedback contribution, deteriorating the resolution, and the smaller fraction of single pad clusters, improving the resolution. In the mixture with iC_4H_{10} the single-photon resolution is slightly better than in pure CH_4 probably due to the lower UV-transmission of iC_4H_{10} reducing the chromatic error and the feedback contribution; however, the ring-averaged resolution is similar to that in pure CH_4 because of the smaller number of Cherenkov photons (Section 2.3.2.2, Fig. 2.37).

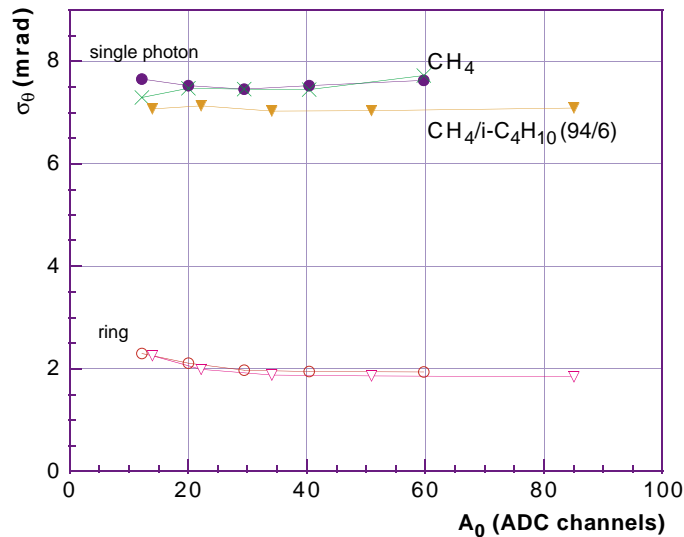


Figure 2.64: Angular resolution as a function of A_0 at $R = 122$ mm, in two gas mixtures; circles and triangles: measurements; crosses: simulation; SPS beam-test (350 GeV/ c π), PC32.

In Fig. 2.65 are reported the single-photon and ring angular resolution, from measurements and simulation, as a function of the particle incidence angle θ_p . No significant deterioration of the resolution is observed in the range of θ_p where most of the HMPID expected tracks will fall.

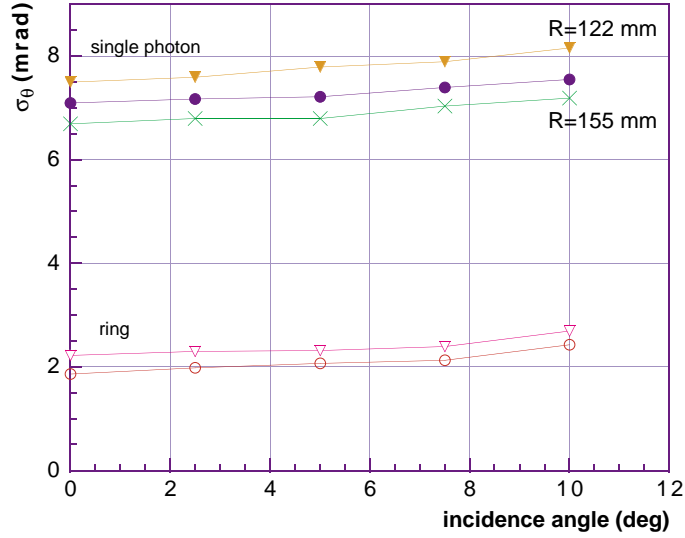


Figure 2.65: Angular resolution as a function of particle inclination at $A_0 \sim 40$ ADC channels; circles ($R = 155$ mm) and triangles ($R = 122$ mm): measurements; crosses: ($R = 155$ mm) simulation; SPS beam-test ($350 \text{ GeV}/c \pi$), $R = 122$ mm: PC30 and $GAP = 80$ mm, $R = 155$ mm: PC32 and $GAP = 103$ mm.

Finally, Fig. 2.66 shows the single-photon and ring angular resolution, from measurements and simulation, as a function of the radiator thickness RW . The small variations of the single-photon σ_{θ_c} are related to the changes of ring radius and radiator transmission with RW , while the ring σ_{θ_c} increases, as expected, at smaller RW as a consequence of the reduction of emitted Cherenkov photons. In general all the observed discrepancies between simulation and measurements could be explained by the difficulty in evaluating correctly the detector rotations used for the angle reconstruction.

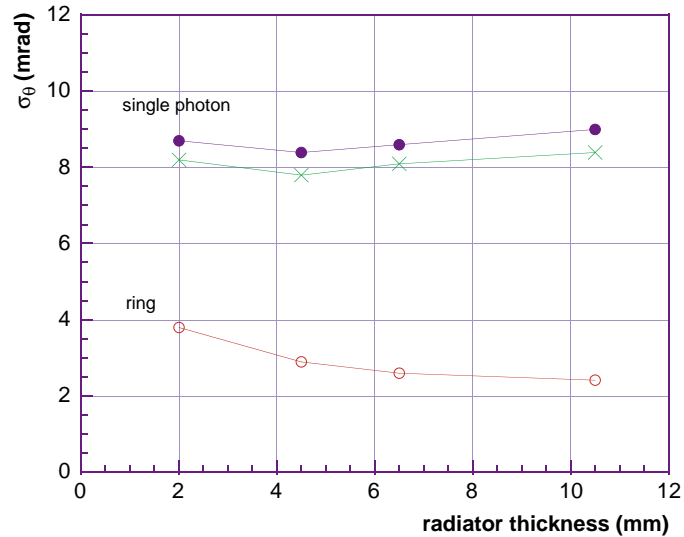


Figure 2.66: Angular resolution as a function of radiator thickness at $R = 104$ mm; circles: measurements; crosses: simulation; PS beam-test ($3 \text{ GeV}/c \pi$), PC24.

2.3.2.6 Proto-2: results obtained with multi-particle events

We present the results obtained by exposing proto-2 to multiparticle events at H4 using a telescope composed of four pad chambers described in Section 2.3.1.2. Two test periods were devoted to this data taking, the first one in April 1998 using a single radiator and the second one in July 1998 with the full radiator

(see Fig. 2.57 showing photocathode and radiation implementation). For both periods, PC29 to PC32 were mounted on proto-2.

Track multiplicity and occupancy

The track multiplicity distribution obtained by analysing real events from pion–beryllium interactions is shown in Fig. 2.67.

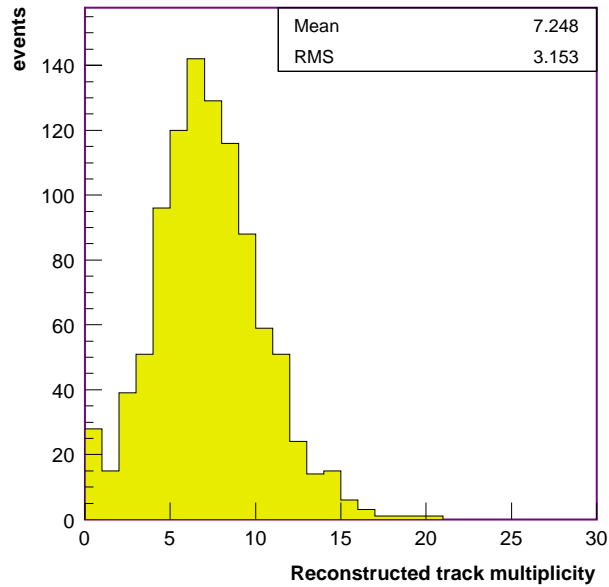


Figure 2.67: Track multiplicity in the HMPID evaluated in π^- -Be events.

The acceptance of the proto-2 is larger than the telescope acceptance, therefore only a fraction of the particles produced are tracked in the telescope. On average, seven secondary particles reach the RICH plane but there are also events with more than 20 tracks. Since no sweeping magnet has been employed in the test, particles hit the proto-2 in a very narrow region around the beam as we can recognize by plotting the distribution of the distance between the impact point of each track on the RICH plane and the beam line (Fig. 2.68).

Consequently, the cathode plane is exposed to a very large track density, as shown in Fig. 2.69. The track density on the HMPID detector has been evaluated by counting the number of tracks contained in annulus regions, 2 cm wide, at a distance d , moving from the beam line to the outer region and dividing it by the chosen fiducial area.

The colour Fig. 2.ii shows a superposition of raw data from 1000 real interaction events. The relative occupancy is shown in Table 2.7.

Table 2.7: HMPID occupancy at different distances from the beam line for two different sets of anode–cathode voltages.

Distance (cm)	2000 V	2100 V
10	10%	15%
30	6%	9%
40	5%	8%

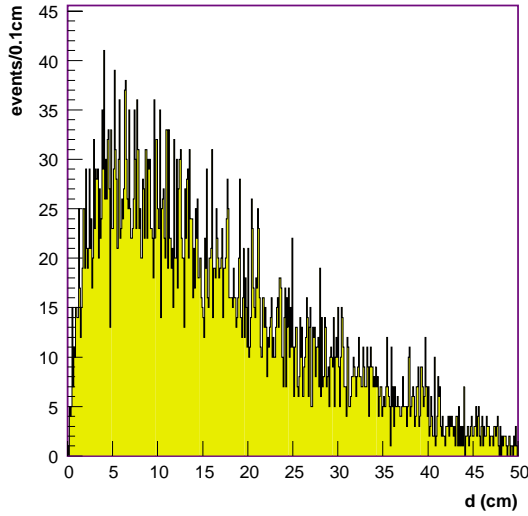


Figure 2.68: The distribution of distances d of track impact points measured on the HMPID cathode plane from the beam line.

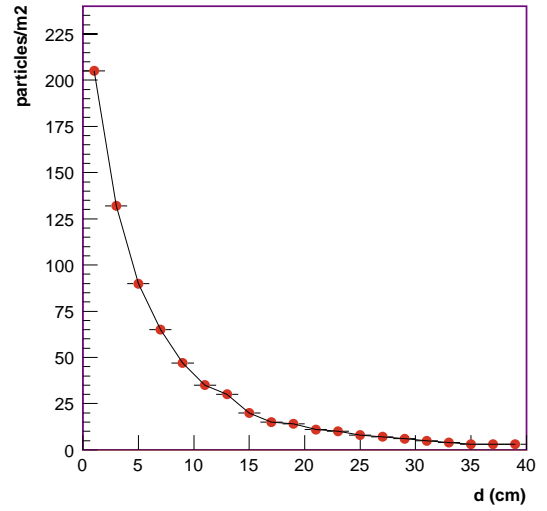


Figure 2.69: Track density on the HMPID cathode plane in real π^- -Be events (see text).

SPS data pattern recognition

The SPS ALICE facility represented a formidable ‘test bench’ for the HMPID prototype in terms of particle density and background as already shown previously. Moreover, SPS data will allow the pattern recognition algorithms to be tested in environmental condition that might also be more severe than those anticipated in the ALICE heavy-ion runs. In order to accomplish this last point, an accurate GEANT simulation of the telescope that takes into account secondary interactions and multiple scattering effects was used to evaluate the tracking capability of the telescope. Tracking errors were accounted for with regard to the spatial resolution of the proportional chambers, and their efficiency according to the specification given in Section 2.3.1.2. Since three pad chambers out of four have a good spatial resolution in the horizontal projection, whilst only one gives a good accuracy in the vertical projection (see Table 2.2 on page 42), tracks are reconstructed by applying the method ‘by view’. In this method, the first step is to reconstruct track projections onto the xz plane and later in the yz plane, z being the beam axis. Track projections are then associated only to those candidate tracks that point back to the target region defined by a box of 15 mm side. Since the pad chamber efficiency is larger than 95%, the reconstruction method requires that every track projection must have a hit in each pad chamber. In Fig. 2.70, the tracking efficiency is shown as a function of the number of tracks generated.

The telescope allows the correct reconstruction, and therefore the association of the respective impact point on the proto-2 plane in almost 85% of the particle trajectories, also in events with 16 tracks pointing to the proto-2. The average momentum of those particles that, being produced in the interaction of a pion beam of 350 GeV/ c on a Be target, impinge the HMPID, is about 40 GeV/ c . Therefore the multiple scattering weakly contributes to the accuracy in reconstructing the particle trajectories. The measured angle resolution $\sigma_{\theta_p} = 1$ mrad is mainly due to the geometry of the pad chambers and their specific spatial resolution. The analysis of the real data based on the Hough transform method, so far developed as discussed in Section 4.3, is in progress. The method seems robust enough also when applied to recognize Cherenkov patterns belonging to tracks that cross the proto-2 plane in a very small region.

A fully reconstructed SPS event is shown in colour Figs. 2.iii and 2.iv.

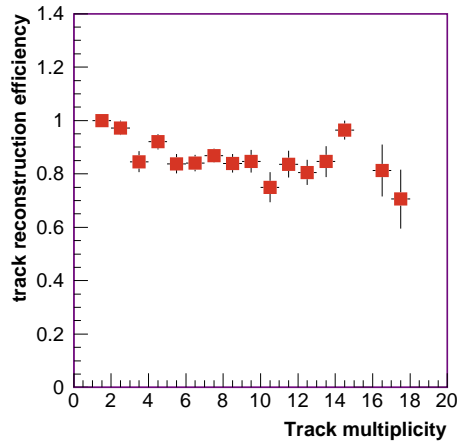


Figure 2.70: Track reconstruction efficiency versus the number of simulated tracks per event.

2.3.2.7 Ageing and ‘heavily-ionizing’ events

Besides the degradation provoked by contaminants, it has been shown in Section 2.1.1.4 that a CsI photocathode operated in a MWPC may be damaged by the impact of the ion clouds of each avalanche. The ion impact rate expected at the ALICE operating conditions has been evaluated from the GALICE event simulation program, discussed in Chapter 4, which provides the charged primary and secondary track densities and associated photoelectron yields. The ion charge per photoelectron and MIP are taken as 8×10^{-14} and 1.2×10^{-12} C, respectively, at a maximum gain of 5×10^5 . According to the densities and rate given for minimum bias collisions in Table 2.8, the total ion charge rate amounts to 5×10^{-11} C/cm² s⁻¹ at ALICE operating with lead beams.

Table 2.8: Track densities and rates in Pb–Pb collisions

Collisions	track/m ²	photoelect/m ²	rate (kHz)
Central	100	1000	0.1
Minimum Bias	25	250	10

In comparison, the beam rates routinely used at the test beams were equivalent to 3×10^{-8} C/cm² s⁻¹. The charge density integrated over a 1 year (10^6 seconds) lead run at ALICE amounts to 0.05 mC/cm², was largely overcome during the test exposure without showing any degradation on the photocathodes, agreeing with the laboratory results shown in Section 2.1.1.4.

Integrating over 10 years of operation at ALICE (proton, calcium, lead modes [9], Section 12.5.3) results in a charge density of 1.2 mC/cm². For comparison, the irradiation test performed with a laboratory set-up shows a stable QE up to 2.5 mC/cm². More ageing tests will be pursued in 1999.

In addition to the class of relativistic tracks, the rate of heavily ionizing events was also evaluated using FLUKA simulation (see Chapter 4). They originate from nuclear reactions and fast neutron interactions occurring in the MWPC gap or its vicinity. As seen in Fig. 2.71, such spectacular reactions were indeed observed in proto-2 during the SPS tests and simulated in GALICE. Neutron interactions correspond to such a local release of energy (MeV range) that they are visible as current pulses, usually self-limited by space charge saturation. However, they represent a potential risk of discharges.

In 1995–96, a relevant information was obtained from the exposure during two periods of four weeks of a CsI-based imaging detector built in our group for the NA44 experiment, using lead beam on target. The CsI photodetectors, part of the Threshold Imaging Cherenkov detector (TIC [11]) were located close to the lead beam dump and were delivering high burst current (100–400 nA). However, the magnetic spec-

trometer in use at NA44 was designed such that very few charged particles were traversing the gaseous radiator of the TIC without even crossing the photodetectors. Hence, it is expected that a large part of the current was produced by neutrons. During these periods, the performance has been found stable and the detector operation satisfactory.

In conclusion, although the ageing of CsI photocathodes is at the present time neither well quantified nor fully understood, our detector has been found stable under ion rates exposures much larger than the one expected during the ALICE operation.

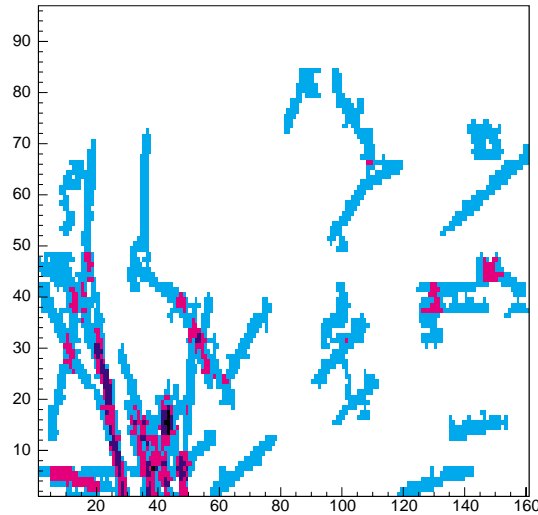


Figure 2.71: Integrated map showing 39 patterns with a cluster size larger than 60 pads. They have been found when analysing 5000 pion–Be events. As seen in Fig. 4.2 on page 155, they correspond to hadronic interactions with the CsI pad plane.

2.4 Event analysis and Monte Carlo simulation

Although the data acquisition is accomplished with a threshold corresponding to a 2–3 sigma of the pedestal variation, mainly for data volume compression, the analysis of each event is preceded by a further cleaning from electronic noise by a 4–6 sigma thresholding. Owing to the good linearity of the FE electronics over the full dynamical range (Section 3.1.4) no corrections of the PH spectrum are required. A typical event is shown in Fig. 2.32 on page 44: it is characterized by clusters of pads relative either to the ionization released by the MIP particle (in the middle) or to the detected Cherenkov and feedback photons (along the ring). As also seen in Fig. 2.32, three different regions can be singled out in such a picture:

- 1) a MIP region, where the particle is expected to cross the detector;
- 2) a fiducial area where all Cherenkov photons are detected, determined by particle momentum, detector geometry, UV transmission of traversed media and CsI quantum response;
- 3) the remaining part of the detector active area, populated mainly by background (electronic noise, feedback photons, cosmic ray ionization, etc.).

Figure 2.34a shows 6000 overlapped events, illustrating the topography of the different fiducial zones. The impact position of particles and photons, for clusters of more than one pad, is evaluated with the centroid finding method, while for single-pad clusters it is assumed to be in the pad centre. Once the MIP centroid has been found, the Cherenkov fiducial zone can be located in the pad plane and the main quantities characterizing the event, inside and outside that region, are estimated. The knowledge of the pad PH, besides a better localization through the centroid method, allows the evaluation of the chamber gain and the single-electron detection efficiency from the cluster PH distribution. Indeed, according to the

rather good symmetry of the signal induced on the pads (Section 2.1.2.3), the clusters can be classified into three categories depending on their size and shape (Fig. 2.72):

- class 1: clusters of one, two or three pads (row or L-shaped) when the PH maximum is in the central pad, assumed to correspond to single photoelectrons;
- class 2: clusters of three pads when the PH maximum is not in the central pad, assumed to correspond to two photoelectrons;
- class 3: clusters of more than three pads, assumed to correspond to two or more photoelectrons.

Clusters are first counted as *raw* clusters and after image processing as *resolved* clusters. Figure 2.72 presents the cluster PH distribution for each class, from beam-test events with proto-2 operated with CH₄ at 2100 V. In those conditions the class 1 PH distribution is generally exponential and the single-electron average PH (A_0), namely the chamber gain, can be deduced from the slope of the fit (also reported in the figure). However, it has been deduced from the simulation that a fraction of such clusters is generated by more than one electron, owing to the overlap of a second Cherenkov photon or feedback photon.

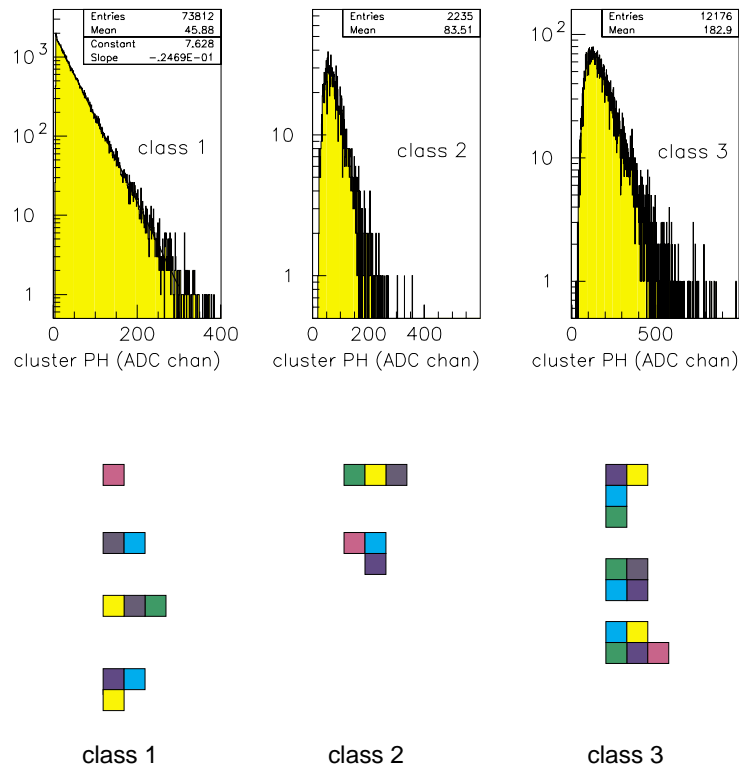


Figure 2.72: (top) The total pulse-height distributions of the three classes of *raw* clusters and (bottom) the geometrical features for each class (the darker the grey tone, the larger the pad pulse height).

The average and the shape of the PH distributions relative to class 2 and 3 clusters, compared to that of class 1, indicate clearly the contribution of two or more photoelectrons. In the majority of the cases those large clusters can be *resolved* into smaller sized clusters: when n local PH maxima are found in the original raw cluster, n resolved clusters are created. The pads in the original raw cluster are associated to a given resolved cluster according to the closeness to the local maxima. When a pad is at the same distance from two maxima, it is associated to both corresponding clusters, with a PH contribution weighted by the PH of the two maxima. Such a procedure improves the localization accuracy of Cherenkov photons: because of the small anode–cathode gap (2 mm) and the larger pad size (8 mm) most of the feedback photons are converted on the same pad hit by the primary photon and the probability that such local maxima are related to Cherenkov photons is quite large.

The main goals of the event analysis are the CsI photocathode response and the Cherenkov angle resolution. The last topic has already been discussed in a previous section. The quantities related to the detection performance are: total number of pads/event, total PH/event, number of raw-resolved clusters/event, raw-resolved cluster size, radius and reconstructed Cherenkov angles (single-photon and ring average). Figure 2.34 shows the respective distributions obtained in the SPS beam test of proto-2 at a chamber voltage of 2100 V. The tool which allows the interpretation of the experimental average values of such distributions is an originally developed Monte Carlo program generating RICH events which can be analysed using the same software adopted for the real beam-test events.

2.4.1 Monte Carlo simulation

The Monte Carlo simulation program *richsim* has been used to obtain very useful information mainly about the CsI photocathode quantum efficiency and to evaluate the many factors affecting the Cherenkov angular resolution. All physical processes, from the Cherenkov emission to the signal induction on the photocathode pad plane, are taken into account. The input parameters are: type of Cherenkov radiator (NaF or C₆F₁₄), its thickness RW and UV-transmission in the 160 to 220 nm range, proximity gap width, O₂ and H₂O contamination (in ppm), CsI QE curve, detector rotation angles, mean pedestal and sigma for electronic noise, chamber gain, photon feedback rate.

Cherenkov photon generation and propagation

The number of photons generated along the particle trajectory in the radiator is drawn from a Poisson distribution with mean N_{av} given by the integral of the Frank–Tamm relation over the energy range established by the CsI photoelectric threshold and the transmission of media traversed by the photons (Fig. 2.24d):

$$N_{av} = RW \int \left(\frac{\alpha}{\hbar c} \right) Z^2 \sin^2 \theta_c(E) dE ; \quad (2.25)$$

α is the fine structure constant, Z is the charge of the particle and θ_c is the Cherenkov angle. The emission point in the radiator is uniformly distributed while the Cherenkov photon energy is sampled from a density function

$$f(E) = 1 - \frac{1}{n^2(E)\beta^2} . \quad (2.26)$$

Each Cherenkov photon is propagated through the detector, undergoing absorption and interactions at the media boundaries. The transmission T_{we} of the collection and cathode wire electrodes is evaluated on a statistical basis according to the relation:

$$T_{we} = 1 - \frac{2r}{s \cos (1 + \tan^2 \theta_0 \sin^2 \phi_c)^{-1/2}} , \quad (2.27)$$

where r is the wire radius, s the wire pitch, θ_0 the Cherenkov photon angle in the proximity gap and ϕ_c the Cherenkov photon azimuthal angle.

Photoconversion at the CsI photocathode

The quantum efficiency curve used to reproduce the PC32 beam-test data is shown in Fig. 2.24d. The QE is, by definition, the probability of photoconversion of an incident photon at a given energy; therefore any QE curve includes the reflection losses which, in turn, depend on the photon incidence angle on the photocathode surface. That has to be taken into account when comparing QE measured in the laboratory with perpendicular UV beam and the quantum response of the same photocathode to Cherenkov photons having oblique incidence. Indeed, in the simulation, a suitable correction for that effect is included: the

PC32 QE curve is such that it can be compared to laboratory measurements and the photoconversion probability is calculated as $QE \cdot (1 - R_\theta)/(1 - R_\perp)$. R_θ , R_\perp are the Fresnel reflection probability calculated using a CsI complex refractive index and including a correction for surface roughness.

Table 2.9 reports the photon losses in the proto-2 configuration. Out of 324 Cherenkov photon/MIP produced in the radiator (in the range 5.7–7.8 eV) 21 are converted into photoelectrons.

Table 2.9: Photon losses out of 324 produced per MIP in the radiator (in 5.7–7.8 eV)

Loss mechanism	Number of lost photons
Absorption in C_6F_{14}	48
Absorption in quartz	52
Absorption in CH_4	6
Absorption in wire electrodes	22
CsI inefficiency	175

Generation of signal on pads and photon feedback

Each photoelectron initiates an avalanche on the anode wire which is closest to the photon impact-point inducing a signal on the neighbouring pads. In addition, the signal corresponding to the ionization released by the MIP in the 4 mm sensitive gap is generated as the convolution of the signal relative to each ion pair. The total charge of any single-electron avalanche is sampled from an exponential distribution having a mean deduced from beam-test data. Then a further contribution coming from feedback is added, with the number of generated feedback photons N_{pf} proportional to the total avalanche charge: $N_{pf} = K_{pf}Q$. A feedback rate, $\overline{K_{pf}}$, of 0.05 (for charge measured in ADC channels) reproduces best the experimental data. This value includes corrections not only for the so-called *visible gain* (Section 2.1.2.5) but also for a reflection at the anode wires which enhances the number of the feedback photons directed towards the photocathode. The photons are generated taking as a source the avalanche at the sense wire, with an isotropic angular distribution and sampling the wavelength spectrum described in Section 2.1.2.4. Such photons, if converted on the photocathode, will generate new avalanches and in turn new feedback. The electrostatic model used for the signal induction is based on the single-parameter Gatti formula described in Section 2.1.2.3.

Electronic noise contribution and PH thresholding

The electronic noise is generated on each pad with a Gaussian distribution having a standard deviation determined experimentally. Finally a PH thresholding with pedestal subtraction produces the event that can be analysed by means of the same test beam data-analysis program.

2.4.2 Analysis results: radiator thickness and HV scan

Figure 2.73 shows the analysis results for the radiator thickness scan with PC24, PS 3 GeV/c beam-test. The agreement between real and simulated data is acceptable, also considering that the QE curve for PC24 used in the Monte Carlo is the one obtained from the NaF-runs analysis which produces an approximate estimation of the differential QE (Section 2.3.2.2). The non-linearity of the plotted quantities with the increasing radiator thickness is due to the saturation induced by the geometrical overlapping of the larger number of Cherenkov photons per ring (Fig. 2.33). In addition, enlarging the radiator thickness makes more effective the photon absorption in the higher energy range, close to the C_6F_{14} cut-off. As a result the emitted photon spectrum shifts towards lower energies corresponding to a reduced quantum response of the photocathode.

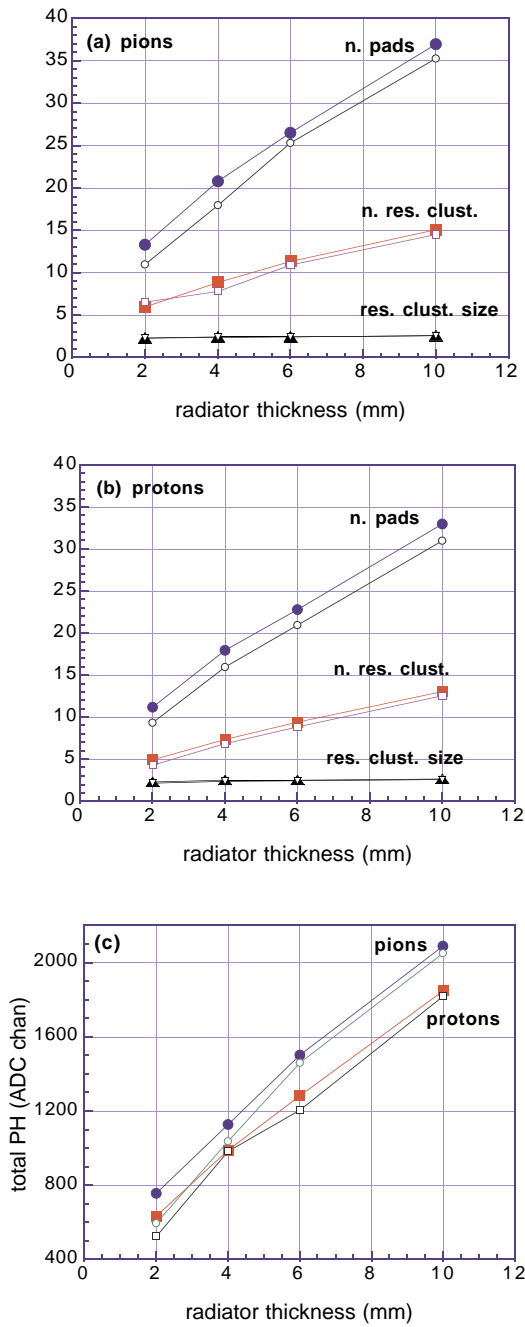


Figure 2.73: Radiator thickness scan in proto-1, PC24, 3 GeV/c PS beam test, chamber voltage 2250 V; full symbols: measurements; empty symbols: simulation. Number of pads, number of resolved clusters and resolved cluster size for pions (a) and protons (b) and total PH per event (c) as a function of the C_6F_{14} thickness.

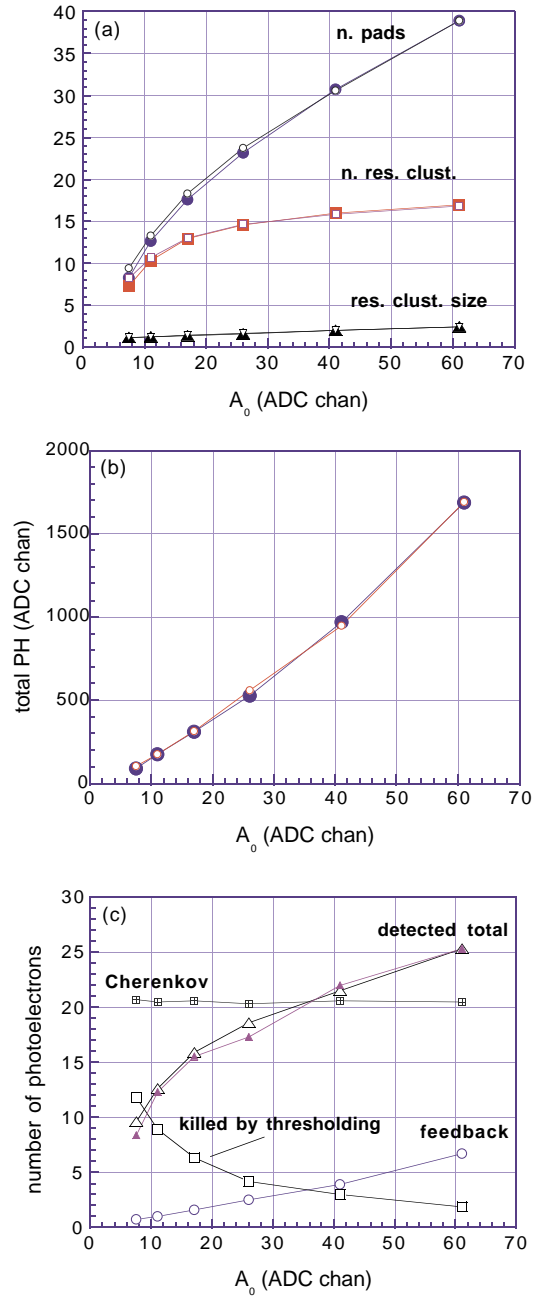


Figure 2.74: Chamber gain scan in proto-2, PC32, 350 GeV/c π SPS beam test; full symbols: measurements; empty symbols: simulation. Number of pads, number of resolved clusters and resolved cluster size (a) and (b) and total PH per event; in (c) the measured total number of detected photoelectrons estimated is compared to the same quantity obtained from the simulation, with an evaluation of the single contributions (detected total = Cherenkov+feedback–killed by thresholding).

In Fig. 2.74 are reported the results of the chamber high voltage scan in proto-2. The variation of the main quantities in plots (a) and (b) can be interpreted in the light of plot (c) where all the contributions to the total number of detected photoelectrons are presented: while the saturation in the number of resolved clusters is due to the plateau of the detection efficiency and the geometrical overlapping, the increase in the number of pads is related to the enhancement of the feedback contribution.

As a concluding remark, the simulation allowed to estimate a factor of merit $N_0 = 45 \text{ cm}^{-1}$ with PC32 and a chamber gain $A_0 = 41$ ADC channels (single electron detection efficiency of 90%).

figure 2.i

figure 2.ii

figure 2.iii

figure 2.iv